

ATOMIC SCALE STUDIES OF THE STRESS EFFECTS ON DEFECT KINETICS  
AND DAMAGE EVOLUTION OF IRRADIATED FE

A Dissertation

by

CHANGWOO KANG

Submitted to the Office of Graduate and Professional Studies of  
Texas A&M University  
in partial fulfillment of the requirements for the degree of

DOCTOR OF PHILOSOPHY

Chair of Committee,	Lin Shao
Committee Members,	Pavel V. Tsvetkov
	Ryan McClarren
	Miladin Radovic
Head of Department,	Yassin A. Hassan

May 2018

Major Subject: Nuclear Engineering

Copyright 2018 Changwoo Kang

## ABSTRACT

Irradiation of the materials with neutrons or energetic particles creates a significant number of point defects and nucleates extended defects, such as dislocations and voids. These defects result in the changes of material properties and degradation. The knowledge of the evolution of damages under different irradiation conditions such as high temperature and stress is important to predict lifetime and guarantee the safety of the nuclear materials.

By means of molecular dynamics and statics simulations, the effects of strain on the damage production are examined. Interstitial is more affected by tensile strain along  $[111]$ . Otherwise, the motion of vacancy is more influenced by compressive strains. In displacement cascade of 10 keV primary knock-on atoms, increased defect production is obtained under strains. The increased diffusivity and anisotropic diffusion along specific directions affect recombination rates between interstitials and vacancies. We also investigate kinetic properties, formation and migration energies of defects in alpha Fe and identify their stable configurations under different strains. By applying uniaxial stress along  $[111]$ ,  $\langle 111 \rangle$  oriented single SIA defects become more stable than  $\langle 110 \rangle$  oriented SIA, which is opposite to stress-free condition. Diffusion of SIA defects under  $[111]$  tensile stress is facilitated along  $[111]$  direction and the diffusion becomes one dimensional (1D). The effects of compressive stress and strain on diffusivities of vacancy clusters are also investigated. The mechanisms of collapse of voids are also studied. We find that spherical voids in alpha-Fe under indentation along  $[111]$  direction

can emit and evolve into planar voids, following by super-fast 1D migration along [111] direction. The results are important to show that defect clusters with planar structure can be migrated to one dimensional with high diffusivity. Under a constant compressive strain, diffusivities of planar voids increase with increasing void sizes, except for a stable configuration of  $V_9$  which is able to convert back from a mobile planar void to immobile spherical voids.

The findings of present works are important to understand both mechanical property and defect evolution of irradiated metals, as expected in nuclear reactors. The information is also useful to develop the multiscale modeling of damages under strain environments.

## DEDICATION

To my family

## ACKNOWLEDGEMENTS

I would like to thank my advisor and committee chair, Dr. Shao, without whom this dissertation would not have been completed. His supervision and encouragement helped me grow as a researcher during my time.

I would like to thank my committee members, Dr. Tsvetkov, Dr. Radovic, and Dr. McClarren for their dedication and support throughout the course of this research. I would like to express my gratitude to Dr. McDeavitt and Dr. Qian for their guidance.

I acknowledge all my colleagues, collaborators, and the department faculty and staff for their help throughout the course of my research and for making my time at Texas A&M University a great and memorable experience. I would also like to thank Dr. Wang and Dr. Hoang, who helped me with my project.

Finally, I thank my parent for their encouragement and to my wife, Hyerim Choi, and daughter, Yunha Kang, for their patience and love.

## CONTRIBUTORS AND FUNDING SOURCES

### Contributors

This work was supervised by a dissertation committee consisting of Professors Lin Shao [advisor], Pavel V. Tsvetkov, Ryan McClarren of the Department of Nuclear Engineering and Professor Miladin Radovic of the Department of Material Science & Engineering.

All work for the dissertation was completed by the student, in collaboration with Dr. Tuan Hoang and Dr. Qingyu Wang of the Department of Nuclear Engineering.

### Funding Sources

Graduate study was supported by a fellowship from Republic of Korea Army and the research was supported by US Department of Energy's NEUP program, through grant no. DE-NE0008297.

## NOMENCLATURE

$\text{\AA}$	Angstrom
BCC	Body -Centered Cubic
DPA	Displacement per Atom
DFT	Density Functional Theory
EAM	Embedded Atom Method
$E_{dam}$	Damage Energy
$E_d$	Displacement Energy
$E_f$	Formation Energy
$E_m$	Migration Energy
$E_{pka}$	PKA Energy
Eq.	Equation
eV	Electron Volt
FCC	Face Centered Cubic
Fe	Ferrum
FIB	Focused Ion Beam
FMD	Freely Migrating Defect
I	Interstitial
KeV	Kilo electron Volt
KMC	Kinetic Monte Carlo
LAMMPS	Large-Scale Atomic Molecular Massively Parallel Simulator

MC	Monte Carlo
MD	Molecular Dynamics
NEB	Nudge Elastic Band
nm	Nanometer
NRT	Norgett-Robinson-Torrens formula
OVITO	Open Visualization Tool
PKA	Primary Knock-On Atom
ps	Picosecond
s	Second
SEM	Scanning Electron Microscope
SIA	Self-Interstitial Atom
SIPA	Stress-Induced Preferential Absorption
SIPN	Stress-Induced Preferential Nucleation
TEM	Transmission Electron Microscope
V	Vacancy

## TABLE OF CONTENTS

	Page
ABSTRACT .....	ii
DEDICATION .....	iv
ACKNOWLEDGEMENTS .....	v
CONTRIBUTORS AND FUNDING SOURCES.....	vi
NOMENCLATURE.....	vii
LIST OF FIGURES.....	xi
LIST OF TABLES .....	xiv
CHAPTER I INTRODUCTION: .....	1
1.1 Literature Review .....	1
1.2 Ion Solid Interactions .....	6
1.3 Damage Cascade .....	8
1.4 Molecular Dynamics .....	15
1.4.1 Empirical Potential.....	18
1.4.2 Ensembles.....	19
1.4.3 Periodic Boundary Conditions .....	20
1.4.4 Defect analysis .....	20
1.4.5 Large-scale Atomic / Molecular Massively Parallel Simulator (LAMMPS).....	21
1.4.6 OVITO .....	22
CHAPTER II EFFECTS OF STRAIN ON THE DISPLACEMENT CASCADE IN FE .....	24
2.1 Introduction .....	24
2.2 Methodology .....	26
2.3 Results .....	27
2.3.1 Anisotropy of diffusion .....	27
2.3.2 Displacement cascade.....	33
2.4 Discussion .....	44
2.5 Conclusion.....	47

CHAPTER III KINETICS OF INTERSTITIAL DEFECTS IN FE: THE EFFECT FROM UNIAXIAL STRESS .....	48
3.1 Introduction .....	48
3.2 Methodology .....	49
3.3 Result and discussion .....	52
3.4 Conclusion.....	71
CHAPTER IV INDENTATION INDUCED FAST ONE DIMENSIONAL MIGRATION OF VACANCY CLUSTERS IN ALPHA IRON .....	72
4.1 Introduction .....	72
4.2 Methodology .....	73
4.3 Result and discussion .....	76
4.4 Conclusion.....	87
CHAPTER V CONCLUSION AND FUTURE WORK.....	90
REFERENCES .....	94

## LIST OF FIGURES

		Page
Figure 1.1	Dimensional changes after irradiation and detailed microstructure of stainless steel after neutron irradiation: (a) Dimensional changes of cold worked 316 stainless steel before and after $1.5 \times 10^{23} m^{-2}$ neutron irradiation. (b) Microstructure of stainless steel irradiated at 510 °C to a neutron dose of $4.7 \times 10^{22} cm^{-2}$ .....	2
Figure 1.2	Operating conditions of traditional and next generation reactors .....	3
Figure 1.3	Mechanisms of radiation damage buildup and effects .....	4
Figure 1.4	The loss of energy of an incident ion: electronic collisions and nuclear collisions.....	6
Figure 1.5	Nuclear and electronic energy losses .....	8
Figure 1.6	Original version of the displacement spike as drawn by Brinkman.....	9
Figure 1.7	Different version of Brinkman’s displacement spike.....	10
Figure 1.8	Energy spectrum of fission neutron for $^{235}U$ .....	12
Figure 1.9	A typical flow chart for an MD simulation .....	16
Figure 2.1	Diffusivities of 1-SIA and vacancy under different uniaxial strains along [111]: (a) Tensile strains for 1-SIA, (b) Compressive strains for 1-SIA, (c) Tensile strains for vacancy, (d) Compressive strains for vacancy .....	28
Figure 2.2	Isotropic Diffusivities of 1-SIA and vacancy under 0% strains: (a) Diffusivities under 0% for 1-SIA (b) Diffusivities under 0% strain for vacancy .....	30
Figure 2.3	Anisotropic Diffusivities of 1-SIA under different uniaxial tensile and compressive strains along [111]: (a-1) Tensile strain 1%, (a-2) Tensile strain 2%, (a-3) Tensile strain 3%, (b-1) Compressive strain 1%, (b-2) Compressive strain 2%, (b-3) Compressive strain 3% .....	31

	Page
Figure 2.4	Anisotropic Diffusivities of vacancy under different uniaxial tensile and compressive strains along [111]: (a-1) Tensile strain 1%, (a-2) Tensile strain 2%, (a-3) Tensile strain 3%, (b-1) Compressive strain 1%, (b-2) Compressive strain 2%, (b-3) Compressive strain 3% ..... 32
Figure 2.5	The average number of interstitial defects (above) and vacancy defects (below) under different uniaxial strains along [111] ..... 35
Figure 2.6	Interstitial and vacancy cluster distribution under different strain types and levels ..... 36
Figure 2.7	The ratio of FMD to NRT under different strains ..... 38
Figure 2.8	Peak number of defects formed during displacement cascades under different strains (up) and the fraction of surviving defects and peak numbers normalized by those of 0% strain (down)..... 39
Figure 2.9	Fraction of surviving defects to peak number formed during displacement cascades under different strains..... 41
Figure 2.10	Recombination rates for specific time after creation of peak numbers 42
Figure 2.11	Average peak time under uniaxial strains along [111]..... 43
Figure 3.1	Formation energies of <111> and <110> SIA defect clusters as a function of strain for cluster containing (a) single SIA, (b) 2 SIAs, (c) 3 SIAs, (d) 4 SIAs, and (e) 5 SIAs..... 58
Figure 3.2	Schematics of migration mechanisms for 1-SIA..... 59
Figure 3.3	The energy barriers of 1-SIA for (a) the migration mechanism A and (b) the migration mechanism..... 60
Figure 3.4	1-SIA migration trajectories under different uniaxial tensile strains along [111] direction at 500 K ..... 61
Figure 3.5	Migration trajectories of (a) 2-SIA, (b) 3-SIA, (c) 4-SIA, and (d) 5-SIA under 0% strain at 500 K ..... 63
Figure 3.6	Migration trajectories of (a) 2-SIA, (b) 3-SIA, (c) 4-SIA, and (d) 5-SIA under 3% strain at 500 K ..... 65

	Page	
Figure 3.7	Diffusion coefficients as a function of temperature under different tensile strain along $\langle 111 \rangle$ direction for defect clusters containing (a) 1-SIA, (b) 2- SIAs, (c) 3-SIAs, (d) 4-SIAs, and (e) 5-SIAs.....	68
Figure 4.1	Schematic diagram of the nanoindentation simulation model .....	75
Figure 4.2	The stress-strain curve for different size of voids .....	76
Figure 4.3	The stress( $zz$ ) for the material with a small void (0.8 nm) .....	78
Figure 4.4	The snapshots of different size voids for 0.8 nm (a 1 to 5), for 1.6 nm (b 1 to 5), and for 2.0 nm (c 1 to 5), showing the collapse of a void and migration under increased compressive stress.....	79
Figure 4.5	The square displacement of vacancy clusters size 11 along $[111]$ and the transformation of structure for migration under 3% compressive strain at 750 K .....	83
Figure 4.6	Structures and movements of vacancy cluster with size 14 under 3% compressive strain and 750 K .....	84
Figure 4.7	The displacements of center of mass (COM) of vacancy cluster with size 9, and configurations under 3% strain .....	85
Figure 4.8	Diffusivities of different sizes of vacancy clusters under 3% compressive strain at 750 K .....	86
Figure 5.1	A possible miniature-sized stress test machine for 3-point bending ....	93

## LIST OF TABLES

	Page
Table 2.1 Diffusion parameters of SIA and vacancy under uniaxial strains along [111] .....	29
Table 3.1 Observed configurations of 1-SIA to 5-SIA under strain free and strains along [111] .....	54
Table 3.2 Formation energies in eV for 1-SIA to 5-SIA under 0% strain .....	55
Table 3.3 Migration energies in eV (diffusion prefactors in $10^{-8}$ m <sup>2</sup> /s) for 1-SIA to 5-SIA under 0% strain .....	55
Table 3.4 Migration energies and diffusivity prefactors of SIAs defects .....	69

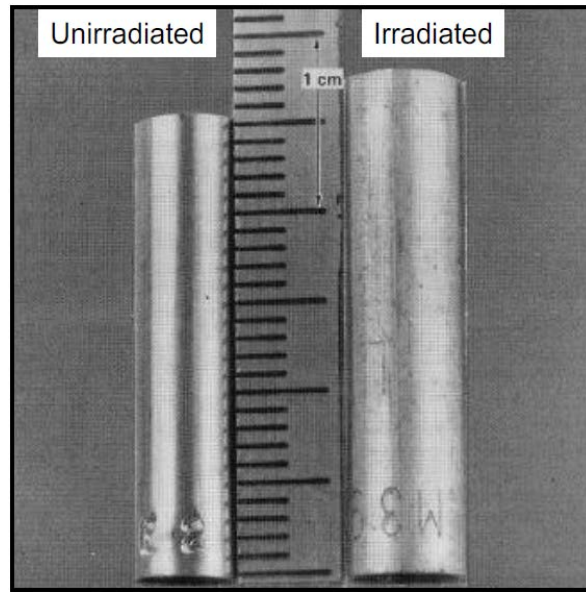
# CHAPTER I

## INTRODUCTION

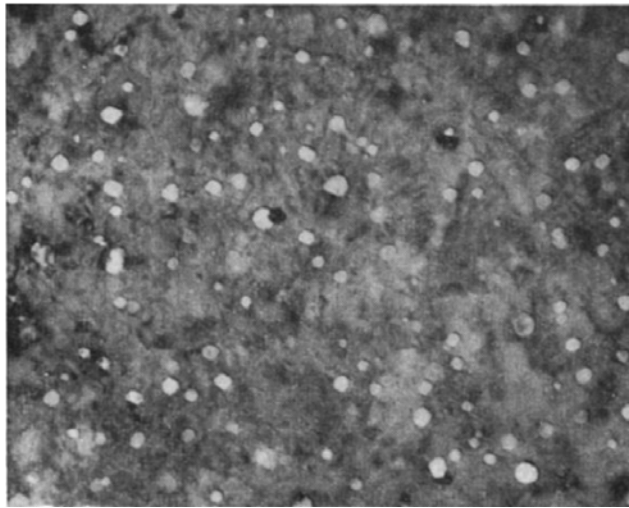
### 1.1 Literature Review

The researches on the radiation damage by ion solid interactions have been widely conducted during the past decades [1]. Especially, stainless steels are one of interested materials, which are main components in structures of nuclear reactors. The materials suffer from harsh conditions such as high pressure, temperature, corrosion, and irradiation. Radiation damages are built up to 100s of DPA (displacement per atom) in core structural components during operation of reactor [1]. The radiation damages create voids, dislocations, and stacking fault defects and lead to irradiation creep, embrittlement, and swelling. Thus, the irradiation under extreme conditions of reactors can generate negative impact on the material's safety and reliability during a lifetime of reactor [2].

Due to the extreme environments and build-up of radiation damages, the materials also experience stresses, strains and dimensional changes. Figure 1.1 shows dimensional changes before and after irradiation and detailed microstructure of stainless steel after neutron irradiation. Those significant dimensional changes and creation of damages inside the materials also would alter the material properties during reactor operation.



(a)



(b)

Fig. 1.1 Dimensional changes after irradiation and detailed microstructure of stainless steel after neutron irradiation: (a) Dimensional changes of cold worked 316 stainless steel before and after  $1.5 \times 10^{23} m^{-2}$  neutron irradiation. Reprinted from [3]. (b) Microstructure of stainless steel irradiated at 510 °C to a neutron dose of  $4.7 \times 10^{22} cm^{-2}$ . Reprinted from [4].

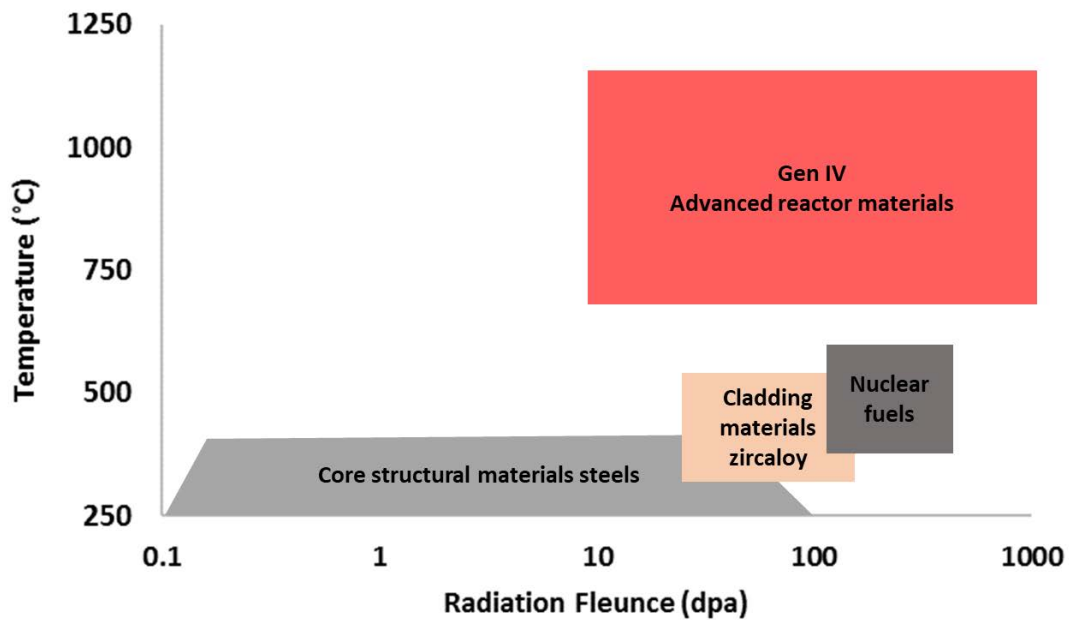


Fig. 1.2 Operating conditions of traditional and next generation reactors.

The future generation's advanced reactors are required to guarantee the safety of materials under even more extreme conditions in comparison with present working nuclear reactors as shown in figure 1.2. Thus, it is necessary to investigate radiation damages on materials under such high temperatures, pressures, and huge irradiation conditions. Figure 1.3 shows how radiation damages are created and evolved. Reactions of nuclear fuels and materials generate lots of radiations such as neutron, electron, gamma ray, and fission products.

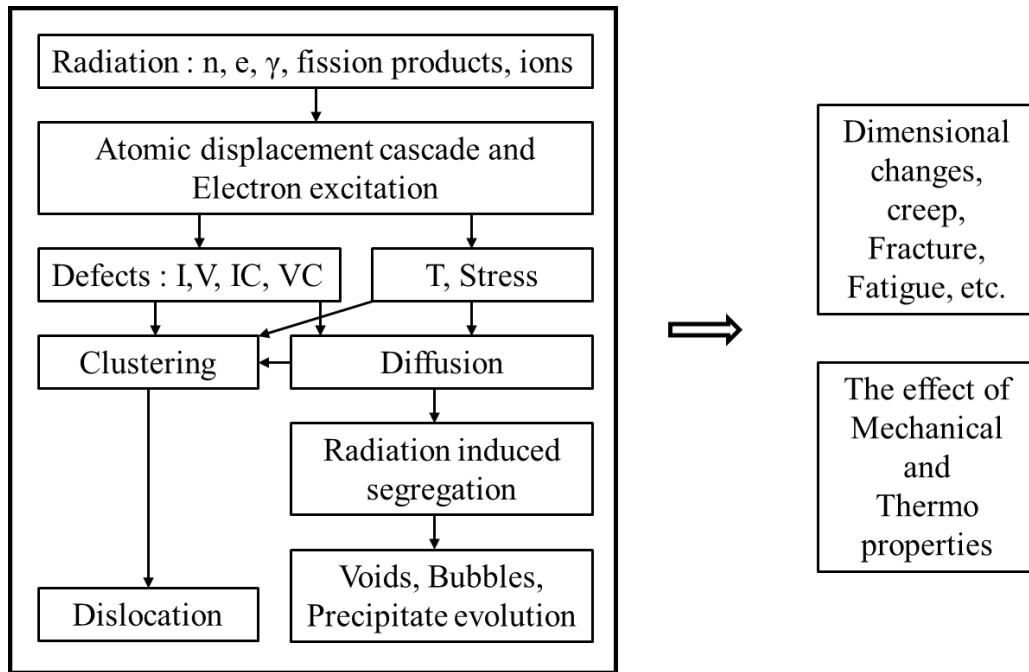


Fig. 1.3 Mechanisms of radiation damage buildup and effects.

The radiations collide with materials and create atomic displacement cascades and electron excitations. Produced interstitials and vacancies diffuse, recombine or agglomerate to form clusters. Interstitial clusters lead to dislocation loops and the vacancies and vacancy clusters could form voids or bubbles. Finally, the conditions and properties of materials before and after irradiation are totally different. The defects affect mechanical and thermal properties of materials. During lifetime of reactors, the radiation damages are even built up and stacked under such changed conditions and the materials are further damaged. For example, the components of reactor suffer from thermal stress, local stress, creep, and external mechanical loads [5-7]. The stress and strains would also affect defect properties such as the displacement threshold, formation, migration energies and their configurations [6-11]. Consequently, the defects are reacted under

such different material conditions and show totally different kinetics. The change of both mobility and migration path under different conditions such as stresses and strains would affect the damage accumulation significantly and cause even more serious consequences for safety operation. However, the detailed mechanisms of defect kinetics under such different stress and strain conditions are still unclear.

For the initial damage creation and their kinetics, computational works based on Density Functional Theory (DFT) and Molecular Dynamics (MD) have been widely used due to the limitations of experiments and resolution of traditional analysis tools. However, only a few limited computational studies have been considered stress and strain effects on the radiation damages. The investigation of stress and strain effects is main purpose on present work. Radiation damage production and their kinetics under different strain environments will be examined and discussed. In addition, we also investigate fast one dimensional migration of defects and clusters, which is one of important factors affecting damage evolution in short and long term scale.

## 1.2 Ion Solid Interactions

Particles coming from fission and fusion reactions collide with lattice atoms and electrons. The particles transfer energy to the lattice atoms, produce primary knock-on atoms (PKAs), and undergo a series of collisions continuously. The ion range is calculated by the energy loss rate along the ion path as shown in equation (1-1).

$$R = \int_{E_0}^0 \frac{1}{\frac{dE}{dx}} dE \quad (1-1)$$

where  $E_0$  is the ion's incident energy and  $\frac{dE}{dx}$  is the energy loss per increment of ion path [12]. Atomic number of ions, ion energy, and a target material are main factors to determine the energy loss rate and the penetration depth. The depths of penetration for individual ions are not equal and follow random process, which are represented as straggling [12]. The net penetration depth/projected range  $R_p$ , which is total path length of projectile, is measured along the direction of incidence [12].

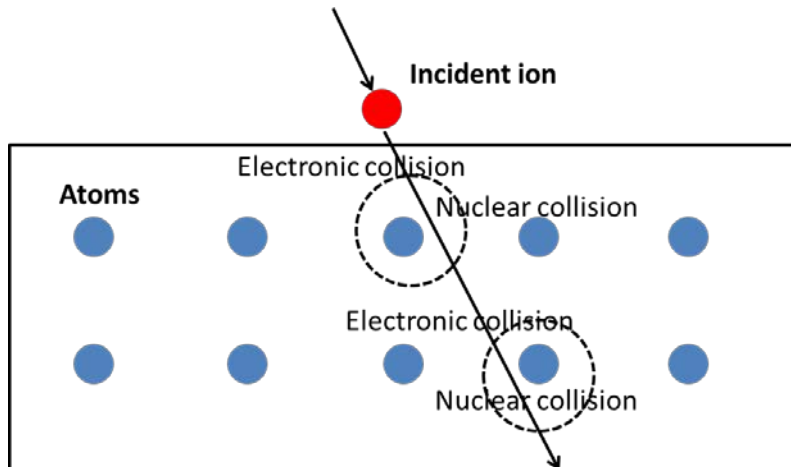


Fig. 1.4 The loss of energy of an incident ion: electronic collisions and nuclear collisions.

Figure 1.4 shows energy loss mechanisms of an ion in a target material. Electronic and nuclear collisions are two mechanisms for energy loss rate of Coulomb interactions of ions with target atoms and electrons. It can be expressed as:

$$\frac{dE}{dx} = \left. \frac{dE}{dx} \right|_n + \left. \frac{dE}{dx} \right|_e \quad (1-2)$$

where  $n$  and  $e$  indicate nuclear and electronic collisions, respectively [12]. The energy loss of nuclear collision is measured by transferred energy per unit length through elastic interactions, which is defined as the nuclear stopping power [12]. The nuclear energy loss is important in a low energy region. The particle loses significant discrete energy and has angular deflections, which can lead to the displaced atoms from their original positions. Otherwise, electronic collision represents that impinging particle excites or removes electrons from an orbital. As ion's energies are high and it has low atomic numbers, the electronic collisions are dominated [12].

Figure 1.5 shows nuclear and electronic energy losses. As velocities of ions  $v$  are lower than that of atomic electrons  $v_0$ , the ions can be neutralized by capturing electrons. Nuclear energy loss decreases as  $1/E_0$  with increasing velocity of ions, and electronic energy loss begins to predominate [12]. In the range from  $0.1 \times v_0$  to  $Z_1^{2/3} v_0$ , electronic energy loss is proportional to  $E^{1/2}$ . As the ion's velocity increases, the charge state of ion also increases from neutral to positive values. It can be considered as a positive point charge at above  $Z_1^{2/3} v_0$  [12].

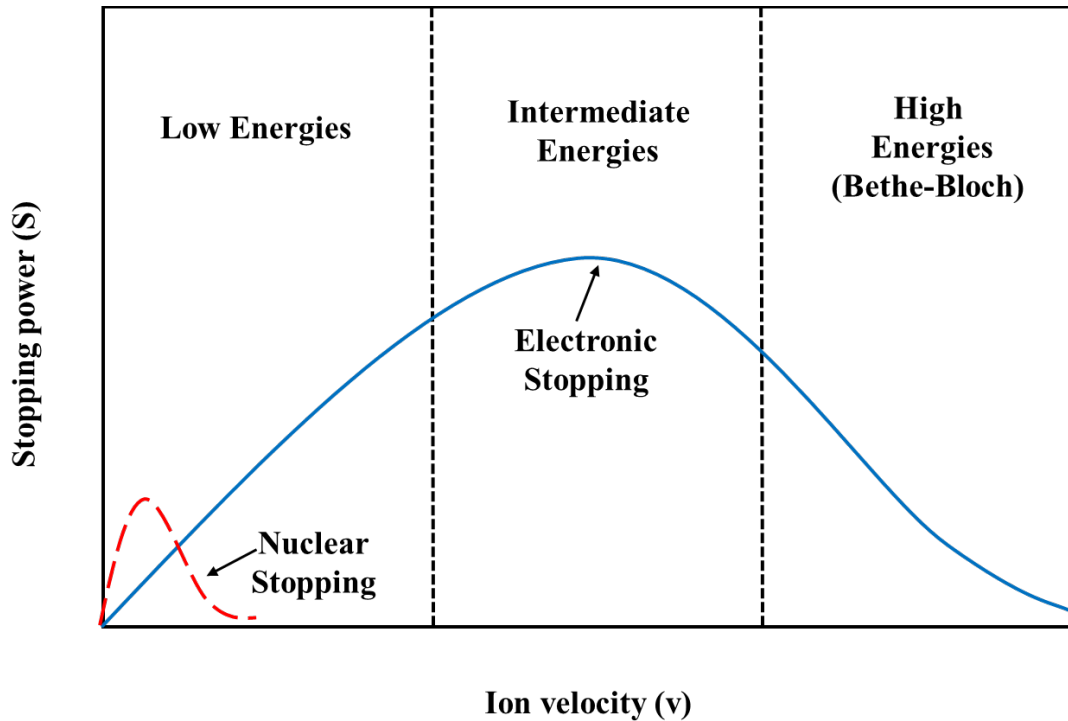


Fig. 1.5 Nuclear and electronic energy losses.

### 1.3 Damage Cascade

As we discussed in previous section, the incident particle collides with atoms in a material and transfers energies to atoms. The atoms are displaced from original positions and become primary knock-on atoms (PKA) create other collisions in the material. A series of those processes are called by displacement cascade. The radiation damages are the results of the displacement cascade. Interstitials, vacancies and clusters are created around the ion track as shown in figure 1.6 and 1.7. A minimum energy is required to displace atom from its lattice site, which is called as a displacement threshold energy,  $E_d$ . If the incident energy ( $T$ ) is less than the displacement threshold energy, the atom remains at its original position, but has large vibration. If the  $T$  is larger than the

displacement threshold energy, the displaced atom and vacancy are produced. The detail damage cascade in molecular dynamics (MD) will be explained and discussed more in later chapter.

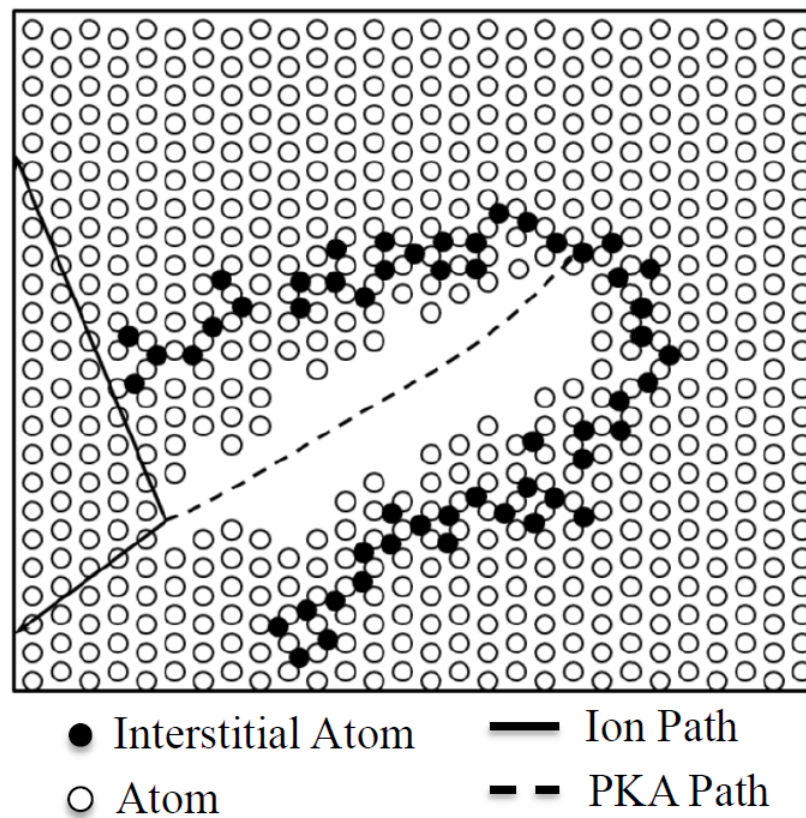


Fig. 1.6 Original version of the displacement spike as drawn by Brinkman. Reprinted from [13].

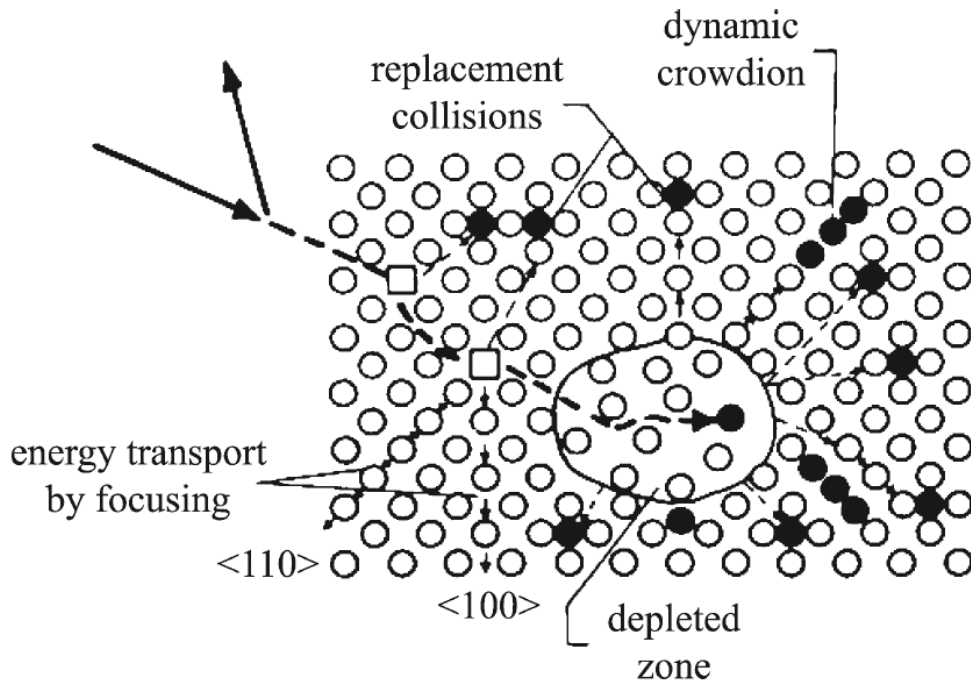


Fig. 1.7 Different version of Brinkman's displacement spike. Reprinted from [14].

There are four stages for the evolution of displacement cascade. First stage is a collision stage in which lattice atoms are knocked and recoiled. It occurs at a time of  $10^{-18}$  s. Second stage is a thermal spike. In this stage, the atoms have huge kinetic energies and convert its kinetic energies to potential energies [15]. It has a high temperature region and period. It also occurs around  $10^{-13}$  s. Next is a quenching stage in which the defects recombine or agglomerate to form clusters, and the system begins to dissipate energies and cool down. Finally, the material is relaxed in the annealing stage. In this stage, defects migrate to form permanent extended defects. In the displacement cascade, it also generates production of crowdion, which is the aligned interstitials along closed packed directions. After the cascade process, a high density of vacancies places in the damaged center region [15].

In nuclear reactors, the generated neutrons from fission or fusion reactions transfer their energies to lattice atoms of structure materials. The transferred energies can be calculated by analysis of using classical dynamics as shown in equation (1-3) [1, 16].

$$E_{recoil,max} = \frac{4mM}{(m+M)^2} E_{initial} \quad (1-3)$$

here,  $E_{recoil,max}$  is the maximum recoil energy, which is represented by PKA energy in the cascade work. The  $E_{initial}$  is an initial neutron energy, M is the sample atomic mass, and m is the mass of neutron. Thus,  $E_{recoil,max}$  becomes  $\sim \frac{4}{M} E_{initial}$  with neutron and relatively heavy particle such as iron, which is a main component of reactor. By considering the neutron energy spectrum caused by fission and fusion reactions and knowing neutron cross section with the target material, the PKA energies can be evaluated. Figure 1.8 shows neutron's energy spectrum for  $^{235}\text{U}$ . The neutrons have energies up to ~14 MeV through fission and ~20 MeV through fusion.

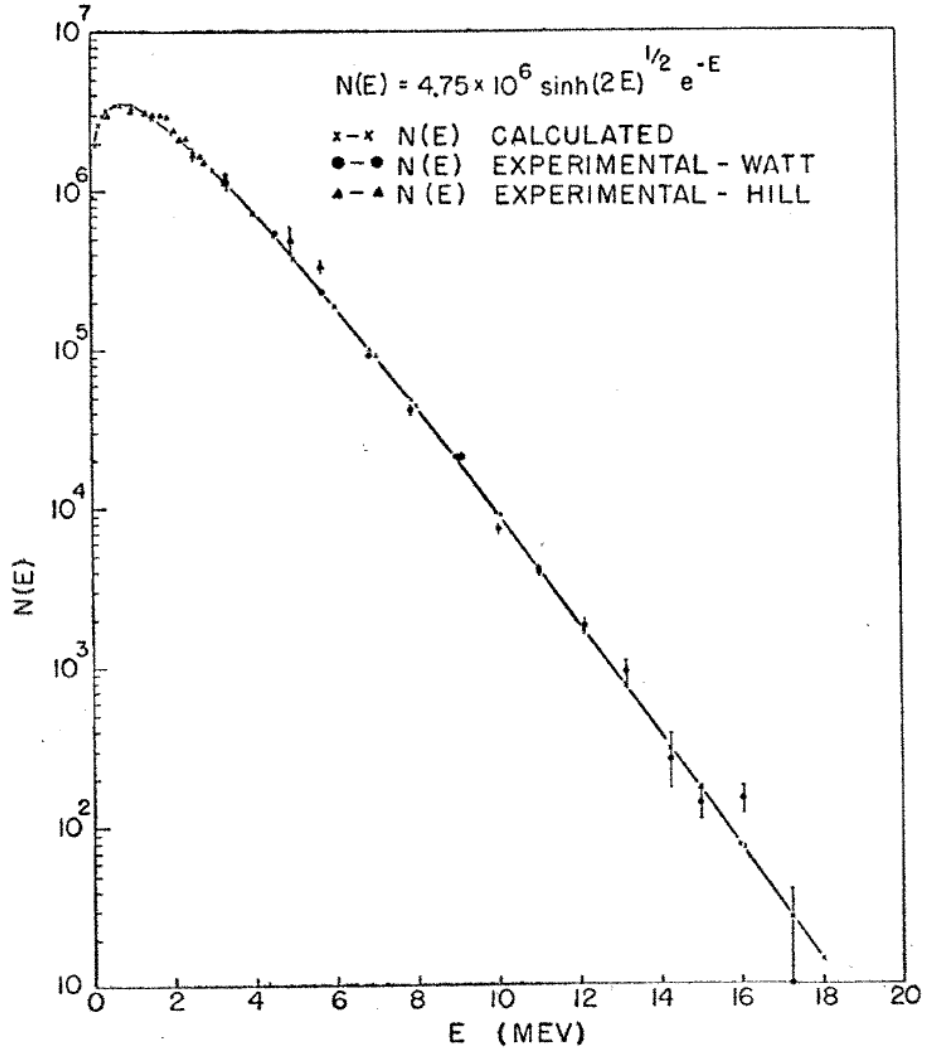


Fig. 1.8 Energy spectrum of fission neutron for  $^{235}\text{U}$ . Reprinted from [17].

One of fundamental model to calculate the number of displaced atoms by PKA is Kinchin-Pease model [18]. Here, we summarize the Kinchin-Pease model and the other models briefly. There are several assumptions to simplify the calculation in the model:

- 1) Elastic collision between atoms,
- 2) If  $T > E_d$ , then the probability of displacement is one,
- 3) randomly located atoms, and
- 4) Electronic stopping is ignored at energies below

the cut-off energy  $E_c$  [12]. Kinchin-Pease model is shown in the equation (1-4). It is assumed that there is a linear relationship between the number of Frenkel pair and the PKA energy under region of between a threshold energy and cut-off energy [18].

$$N_{dis} = \begin{cases} 0 & \text{for } T < E_d \\ 1 & \text{for } E_d < T < 2E_d \\ \frac{T}{E_d} & \text{for } 2E_d < T < E_c \\ \frac{E_c}{2E_d} & \text{for } T \geq E_c \end{cases} \quad (1-4)$$

Norgett, Robinson, and Torrens (NRT) also developed displacement model, which is used as a standard in the nuclear industry [19]. The NRT formula can be expressed by equation (1-5).

$$N_{dis} = \frac{\kappa E_{pka}}{2E_d} \quad (1-5)$$

The displacement efficiency  $\kappa$  accounts for the effects of realistic atomic scattering, which is approximately 0.8 obtained from an extensive works using the binary collision approximation (BCA) [20]. Based on previous MD works, the NRT formula overestimates the total number of Frenkel pair due to the limitation of the formula, which does not consider spontaneous recombination reactions of interstitials, vacancies and clusters [15]. However, the NRT model is still valuable to use the atomic displacements per atom (dpa) as an exposure parameter [15]. Thus, it can be used as a comparison of radiation exposure for different bombarding particles and target materials. The dpa quantity is calculated by the number of displaced atoms divided by the number of atoms in the volume.

Next, we briefly introduce the damage on material during reactor operation. After displacement cascades, the remaining defects such as vacancies, interstitials, and clusters diffuse, agglomerate, and recombine among them. The point defects can generate different types and structures of vacancy loops, voids, interstitial loops and dislocations. Those extended defects can be observed from experiment analysis tools such as TEM after neutron or heavy ion bombardments. The irradiated materials can suffer irradiation growth and irradiation creep. The irradiation growth means the dimensional change with conserved volume under irradiation. Anisotropic diffusion of defects is one of factors for the irradiation growth, which can be explained by Diffusion Anisotropy Different (DAD) model [21]. The creep is the time-dependent deformation of a metal under constant load and at high temperature [1]. Thermal and irradiation creep are main types of creep. Irradiation creep rates are sufficiently larger than thermal creep rates at the same temperature [1]. Irradiation increases the number of interstitials and vacancies, so enhances defect production. As loops and voids form and grow, the creep and stress increase even further. Stress-Induced Preferential Nucleation of Loops (SIPN) and Stress-Induced Preferential Absorption (SIPA) can explain for the transient portion of the creep behavior [1]. When materials suffer from stresses, interstitial loops are more likely to nucleate on planes with a preferred orientation, which is a perpendicular to the applied tensile stress. Otherwise, vacancy loops are more likely to be formed on planes parallel to the tensile stress. On the other hand, SIPA means that applied stresses cause preferential absorption of interstitials and clusters in dislocations that are aligned with the stress [1].

## 1.4 Molecular Dynamics

Molecular dynamics (MD) is an atomistic simulation and modeling method based on classical mechanics. It simulates kinetic and thermodynamic properties of the materials. With improvement of computer technology and its ability, MD simulation has been widely used in various areas. It can be characterized as a way of particle tracking. It solves many body interactions among atoms based on classical Newton's equations. By using numerical integration of equation of motions, it can provide atomistic details of microstructural evolutions in nuclear materials. In order to analyze radiation damage for wide range of length and time scales, it should be integrated with other computational methods such as Density Functional Theory (DFT), Rate Theory (RT), and Kinetic Monte Carlo (KMC).

Figure 1.9 shows a flow chart of MD simulation. The forces are calculated from interatomic potential, and it should explain proper physical description. However, the force calculation of the flow chart is most time consuming work among the steps. Thus, it should also consider the computational efficiency. First, the position of atoms should be set in the system. Then, the velocities of atoms are allocated. Then, MD calculates the

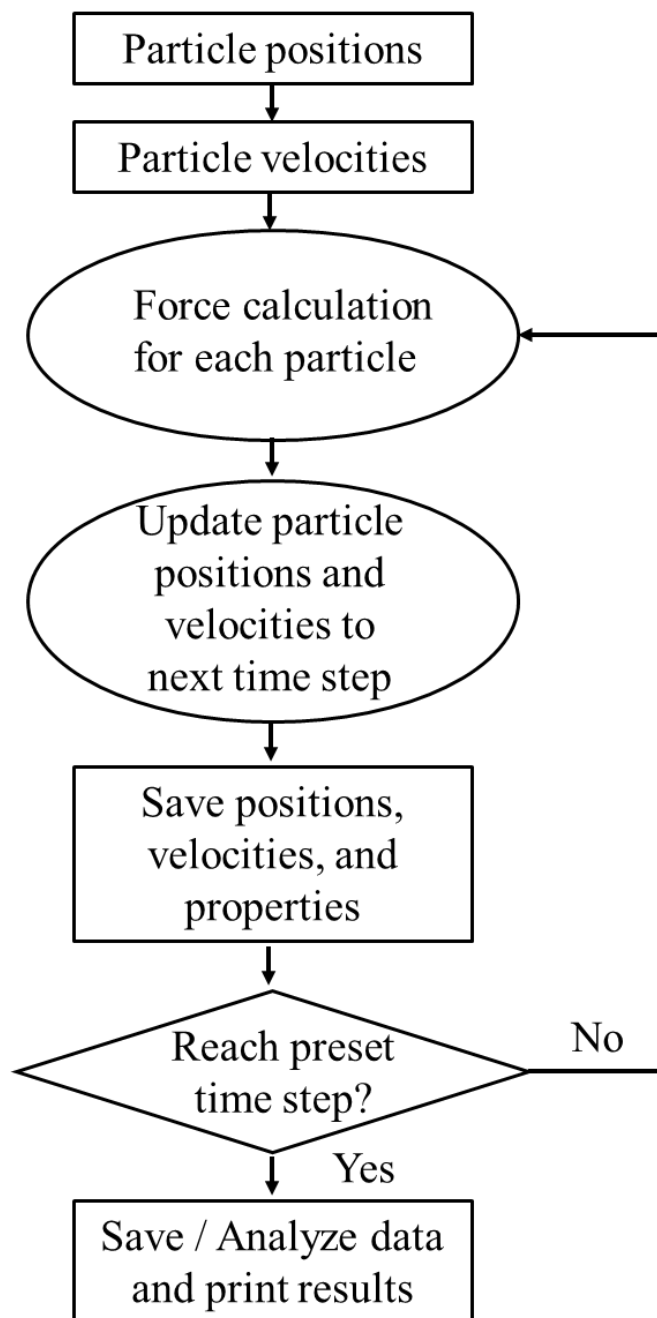


Fig. 1.9 A typical flow chart for an MD simulation.

force of each atom by using the interatomic potential with a time step by using Newton's equation. With the force calculation, atom's new position and velocity are updated and saved in the time step. MD also provides other kinetic properties, which are assigned by user. The force calculation is repeated and if the preset time step is achieved, then user can analyze the data with dump results.

Here, the basic algorithm of MD simulations, which is based on classical mechanics, will be discussed more. The Newton's equation is as following:

$$f_i = m\ddot{r}_i \quad (1-6)$$

where,  $r_i$  is the atom position, which can be calculated by integration of the above equation.  $f_i$  is the force on atom, which can be calculated from atomic potential  $U$ .

$$f_i = -\frac{\partial U}{\partial r_i} \quad (1-7)$$

The atomic potential is most important to estimate atomic position, velocity and force in MD simulation. The numerical integration of force and the force calculation from atomic potential are required to assume that the position and the velocity of each atom can be derived from Taylor Expansion. One of most popular algorithms for numerical methods is Verlet algorithm. Here, we introduce the Verlet algorithm briefly. First, the Verlet algorithm is derived as:

$$\begin{aligned} v\left(t + \frac{1}{2}\delta t\right) &= v(t) + \frac{1}{2}a(t)\delta t \\ r(t + \delta t) &= r(t) + v\left(t + \frac{1}{2}\delta t\right)\delta t \\ v(t + \delta t) &= v\left(t + \frac{1}{2}\delta t\right) + \frac{1}{2}a(t + \delta t)\delta t \end{aligned} \quad (1-8)$$

The Verlet algorithm calculates the positions of atoms after one time step based on current position and velocity of atoms. After half time step,  $\frac{1}{2}\delta t$ , it calculates a velocity to get the new position. After then, it again calculates the position and velocity with the estimated velocity. In the above equation, the acceleration is derived from potential energy. The Verlet algorithm is straightforward and has modest storage requirements.

#### 1.4.1 Empirical Potential

Interatomic potential is most crucial part in MD simulations. It should be chosen proper potential for each purpose and system. Different potentials respond different characteristics of system or materials. For example, Lennard-Jones potential is good for a system with week bond interactions. This potential is can be expressed as follows:

$$U(r) = 4\epsilon \left[ \left(\frac{\sigma}{r}\right)^{12} - \left(\frac{\sigma}{r}\right)^6 \right] \quad (1-9)$$

For the empirical many-body potentials, it is proper to use in a system for metallic bonds. Embedded Atom Method (EAM) potential [22] and Finnis-Sinclair (FS) potential [23] are two common many-body potentials. The two potentials are based on different theories. EAM potential is obtained by DFT, and FS potential is obtained by Tight Binding Theory. Present works are all based on EAM potential. Here, fundamental of EAM is introduced. The potential's general form can be seen in equation (1-10).

$$U = \frac{1}{2} \sum_{i=1}^N \sum_{j \neq i}^{N-1} V(r_{ij}) + \sum_{i=1}^N F(\rho_i) \quad (1-10)$$

where,  $V(r)$  is pair potential function,  $F(\rho)$  is the embedding function,  $\rho_i$  is the electron density, and  $r_{ij}$  is the distance between atom  $i$  and  $j$ . The embedding function

corresponds to the energies for placing one atom  $i$  to electron environment. EAM can deal with electrons contribution, which is important for metallic systems. The electron density contribution is shown in equation (1-11).

$$\rho_i = \sum_{j \neq i} \varphi(r_{ij}) \quad (1-11)$$

Thus, the EAM potential can be rewritten as follows and the separation distance  $r_{ij}$  is only part to estimate the energy.

$$U = \frac{1}{2} \sum_{i=1}^N \sum_{j \neq i}^{N-1} V(r_{ij}) + \sum_{i=1}^N F(\sum_{j \neq i} \varphi(r_{ij})) \quad (1-12)$$

#### 1.4.2 Ensembles

There are several ensembles in MD simulation. If total energy of the system  $E$ , total number of atoms  $N$ , and the volume are conserved in the system, then it is microcanonical ensemble (NVE). In the case of sufficiently large system, the part of the system can be assumed as a canonical system. If the system requires precise temperature control, isothermal ensemble, such as canonical ensemble (NVT), should be used in MD simulations. In the canonical ensemble, the number of atoms, the volume of system, and temperature are constant. The system can be matched with its outside temperature with this ensemble. Isothermal-isobaric ensemble (NPT) is also one of generally used ensembles to relax the system. With this ensemble, the number of atoms, pressure, and temperature are constant. It should be chosen right time step and period to equilibrate the system with those ensembles by considering system size and properties.

### 1.4.3 Periodic Boundary Conditions

If the number of atoms in the simulation box is large, then the computational cost is expensive. In order to simulate large systems with small number of atoms, periodic boundary condition can be used. In periodic boundary condition, one atom moves out of the cubic box, it enters again into the simulation box from the opposite side. It can be used in the bulk region of materials, or in the surface effect is not concerned [15]. Even though, the periodic boundary condition is effective to reduce the number of atoms, it should be careful to use the conditions in the MD simulation. Proper number of atoms should be chosen to satisfy the equilibration of system, which can be matched with experimental conditions. It also should be cautious about the cross-atoms in the cascade simulation. During the displacement cascade, if the atom crosses the boundary, it can interact with itself. Thus, it should be used sufficiently large system or damped the boundary atoms [15].

### 1.4.4 Defect analysis

In MD simulations, defects such as interstitials, vacancies, and clusters can be detected by using the Wigner-Seitz cell method [24]. The simulation cell divided by Wigner-Seitz cells are compared each before and after irradiation. The comparison of initial and final position of each atom in the Wigner-Seitz cell provides defects. If the cell has two atoms, this is interstitial defect. If there is no atom in the cell, it indicates a vacancy. Clusters also can be found by using a set of cut-off distances. The cut-off distance of interstitial can be chosen as the distance between the third and fourth nearest

neighbor atoms [15]. In the case of vacancy, the cut-off distance can be chosen between the second and the third nearest neighbor atom distance [15]. The different cut-off distance can provide different size of clusters. However, the difference is small within the statistical uncertainties. Dislocation line and their Burgers vectors can be extracted by using Burgers circuit analysis [24, 25]. Stukowski and Albe developed dislocation detection algorithm for atomistic simulations [24]. Based on the automated Burgers circuit analysis, they presented a computation method to directly extract dislocation lines and provided a way to visualize dislocation processes during sub-picosecond time scales [24].

#### 1.4.5 Large-scale Atomic / Molecular Massively Parallel Simulator (LAMMPS)

Large-scale Atomic / Molecular Massively Parallel Simulator (LAMMPS) is one of MD simulation software packages [26]. Sandia National Laboratory developed and released the LAMMPS. It is open source code, which is written in C++, and has high availability in a wide range of research areas. The capability and usage of the software are expanding continuously by the developer and worldwide users. New functions and packages can be included in the LAMMPS. User can use those developed packages for their researches conveniently. LAMMPS also can be executed in parallel using some type of message passing interface [26].

Input and potential file are main components in LAMMPS. A LAMMPS input script has 4 parts: initialization, atom definition, settings, and running a simulation. Details of each part and their commands can be found in manuals and their website. The

various potential files are included in the LAMMPS source code. The potential files also can be found in several repository sites such as National Institute of Standards and Technology. After running the simulation, output files of LAMMPS such as a log file and dump files, are obtained. In some cases, users are required to do post-processing for more detailed analysis of the results.

#### 1.4.6 OVITO

Atomistic data obtained from molecular dynamics can be visualized by the Open Visualization Tool (OVITO) [24]. OVITO also has unique analysis and animation functions in their graphical interface. The powerful visualization techniques enable users to understand and visualize the physical complex. In many cases, analysis techniques are useful to extract more information from the atomistic data. Thus, the many functions and analysis techniques from OVITO can produce a meaningful scientific depiction from the raw data. It has been designed with flexibility and extensibility, so that data from MD and Monte Carlo simulation can be analyzed and visualized easily [24]. OVITO provides different functions such as coloring atoms based on their type or atom's value, transformation of atoms, calculation of displacement vectors, slicing or cutting of atomic structures, selection of atoms based on user-defined values, calculation of atomic bonds, and others [24]. OVITO also provides sophisticated analysis functions such as common neighbor analysis, cluster analysis, and atomic-level strain tensors. OVITO can display a few millions of atoms smoothly by rendering techniques and Users can extend the

software to their own requirements with easy and convenient plug-in [24]. Additional detailed information can be found in the OVITO website with new version.

## CHAPTER II

### EFFECTS OF STRAIN ON THE DISPLACEMENT CASCADE IN FE

#### 2.1 Introduction

Iron-based stainless steels have been used as structural materials in nuclear fission and fusion reactors. During reactor operation, these materials suffer from high exposure to radiations, high heat flux, and pressure. Neutrons and heavy particles produced from nuclear reactions in the reactor core induce radiation damages in the materials. Besides, reactor's components also experience large thermal stress, and local stress due to extended defects and impurities as well as irradiation creep and external mechanical loads, which are important factors for deformation of materials [5-7, 9]. Therefore, understanding the effects of stress on the radiation damage production in high irradiation environments is important to evaluate the degradation of materials used in nuclear reactors.

Extensive works on radiation displacement cascade in iron for initial damage generation as a function of temperature, energy, and direction of primary knock-on atom (PKA), and extrinsic particles have been done [27-41]. However, few studies have been conducted to investigate the displacement cascade under various stress and strain conditions. The stress and strain can affect defect properties such as displacement threshold, formation and migration energies, and configurations [6-9, 11, 42]. Due to such different properties, the defect production rate, cluster size, and microstructure configurations would be altered with short and long period of time.

For BCC iron, Gao et al. [8] studied the effect on the displacement cascade under uniaxial tensile strains less than 1% along  $\langle 111 \rangle$ . They reported a decrease in the number of defects, and interstitial defects aligned parallel to the strain direction. Beeler et al. also examined the effect of applied strain on damage production under different types and magnitudes of strains [7]. They mentioned that high-magnitude hydrostatic strains and uniaxial strains create significant variances of defect generations, while the monoclinic and tetragonal shear strains show no significant changes in the production of damages. These studies show the importance of strain for radiation damages. However, it is still essential to further investigate the effects of stress and strain under different conditions such as the direction of the applied stress, stress type, and magnitude. A previous work with Cu from Miyashiro et al. revealed that defects increase under both uniaxial tensile and compressive strains [11]. More interestingly, isometric strains, which is volume conserving, generate the largest number of defects [11] However, the largest number of defects under isometric strains has not been reported in bcc-Fe. Wang et al. investigated the effects of strain under different strain directions in bcc-W, which are parallel and perpendicular to the PKA directions [10]. They showed that the number of defects and defect clustering increase or decrease under hydrostatic tensile or compressive strains, respectively, meanwhile no significant change on defect production under uniaxial strains was observed [10].

Previous works have provided limited results the strain effects on displacement cascade. It is also difficult to compare previous results among different materials types. Present work covers displacement cascades in pure iron under uniaxial tensile and

compressive strains, and isometric strains along [111] using molecular dynamics (MD) simulations. We study the defect production and the cluster size under different strain conditions. We also examine anisotropy diffusivity of defect migration. The importance of anisotropy will be discussed with regard to the recombination rate, migration path, diffusion anisotropy and alignment of defects. We also discuss how those results affect the displacement cascades.

## 2.2 Methodology

All calculations are done by molecular dynamics simulations using LAMMPS software [26] and visualized by OVITO [24]. We use the Embedded Atom Method (EAM) interatomic potential developed by Mendeleev et al. [43]. The PKA energy is 10 keV for all simulations with periodic boundary conditions to all directions. Random PKA directions are used to simulate the damage cascades. Three orthogonal axes of the bcc crystal are set as [1-10], [-1-12], and [111] for the x, y, and z-axis, respectively. The uniaxial strains and isometric strains vary from -3 % to +3 %. The (-) and (+) signs mean compressive and tensile, respectively. The strains are applied along the [111] axis. There are several advantages for the direction under strain environment. The direction shows the largest differences of formation energy between  $\langle 110 \rangle$  and  $\langle 111 \rangle$  [8, 44]. Second, the  $\langle 111 \rangle$  is related to the migration of defect both interstitial and vacancy. Lastly, the orientation of defect along the strain direction can be detected, which is related to the SIPN mechanism [10, 11, 44]. The system is relaxed for 100 ps with NPT of a timestep of 1 fs. After strain is applied to the material, the cell is relaxed again with NVT

ensemble. For each strain level, 30 simulations are conducted for statistical analysis with random PKA directions. Thus, the results explain the averaged behavior of defect production and clustering. To dissipate the heat from the system, the border atoms are applied NVT ensemble at given temperature 0 K. The calculations are performed with adaptive time step from 0.01 fs to 1 fs with NVE ensemble. It can provide the force calculation within the very short time step. The Voronoi decomposition is used to detect interstitial and vacancy [24]. We used both author's own code and OVITO software for finding defects. Both methods provide same results. We provide the results calculated by OVITO software. For cluster analysis, we use the cutoff radii the 2<sup>nd</sup> nearest neighbor distance for vacancy and the 3<sup>rd</sup> nearest neighbor distance for interstitial, respectively.

## 2.3 Results

### 2.3.1 Anisotropy of diffusion

The -3 % (compressive) to +3 % (tensile) uniaxial strains are applied to investigate the diffusivity, activation energy for migration and dimensionality of defect motion. Figure 2.1 shows diffusivities of single SIA and vacancy under different uniaxial strains along [111]: (a) Tensile strains for 1-SIA, (b) Compressive strains for 1-SIA, (c) Tensile strains for vacancy, (d) Compressive strains for vacancy.

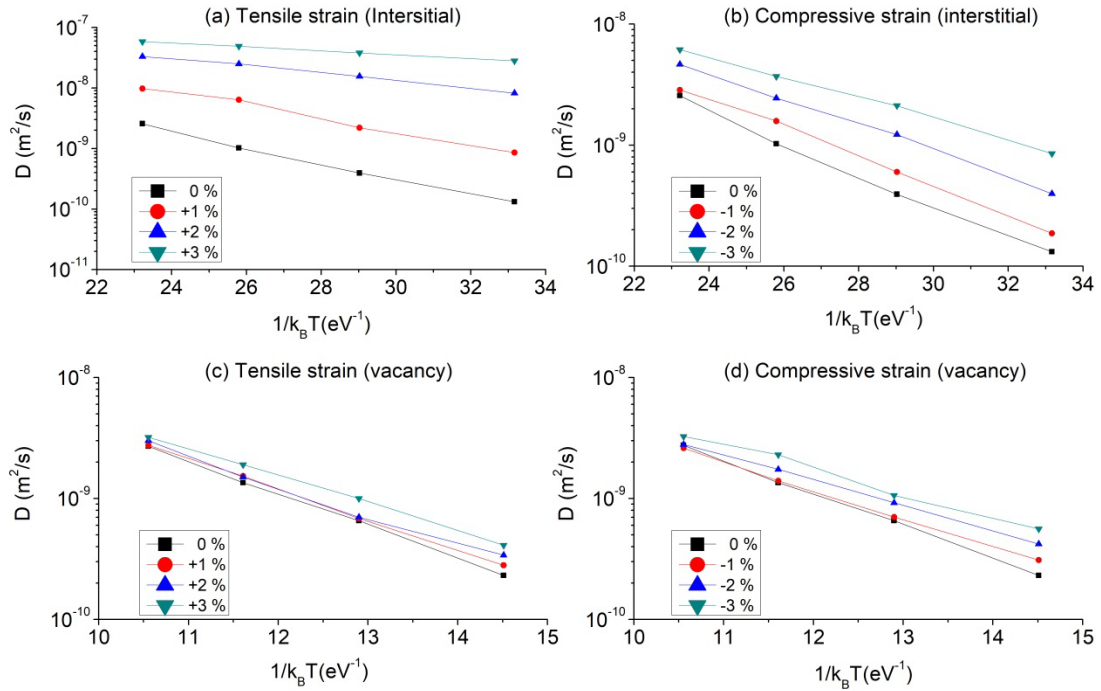


Fig. 2.1 Diffusivities of 1-SIA and vacancy under different uniaxial strains along [111]: (a) Tensile strains for 1-SIA, (b) Compressive strains for 1-SIA, (c) Tensile strains for vacancy, (d) Compressive strains for vacancy.

The diffusivities of single SIA and vacancy increase under both tensile and compressive strains. The SIA has the highest diffusivity under 3 % tensile strain due to fast 1D migration along the applied strain direction. The anisotropic diffusion along one direction is discussed with next figures from 2.2 to 2.4. Migration energies are calculated from the Arrhenius relations of the result as shown in Table 2.1. The migration energies of SIA and vacancy decrease as strains increase for both tensile and compressive strains. The lowest migration energy for SIA, which is about 0.07 eV, is obtained at 3 % tensile strain. The migration energy (0.07 eV) is comparable to those of large interstitial clusters

under zero strain, which has been reported in previous studies [45, 46]. Migration energies of SIA vary more significantly under uniaxial tensile strains, from 0.3 eV to 0.07 eV. Meanwhile, for vacancy, the migration energies are more affected by compressive strains, vary from 0.62 eV to 0.46 eV. Thus, the migration energy for vacancy under 3% compressive strain (0.46 eV) is less than that of 3% tensile strain (0.525 eV).

Table 2.1 Diffusion parameters of SIA and vacancy under uniaxial strains along [111].

Type	Parameter	Compressive strain (%)			0	Tensile strain (%)		
		-3	-2	-1		1	2	3
SIA	$D_0$ ( $\times 10^{-8}$ m <sup>2</sup> /s)	60	100	200	230	383	91	33
	$E_m$ (eV)	0.2	0.245	0.28	0.3	0.23	0.14	0.07
Vacancy	$D_0$ ( $\times 10^{-8}$ m <sup>2</sup> /s)	40	50	70	200	100	90	80
	$E_m$ (eV)	0.46	0.48	0.54	0.62	0.58	0.55	0.525

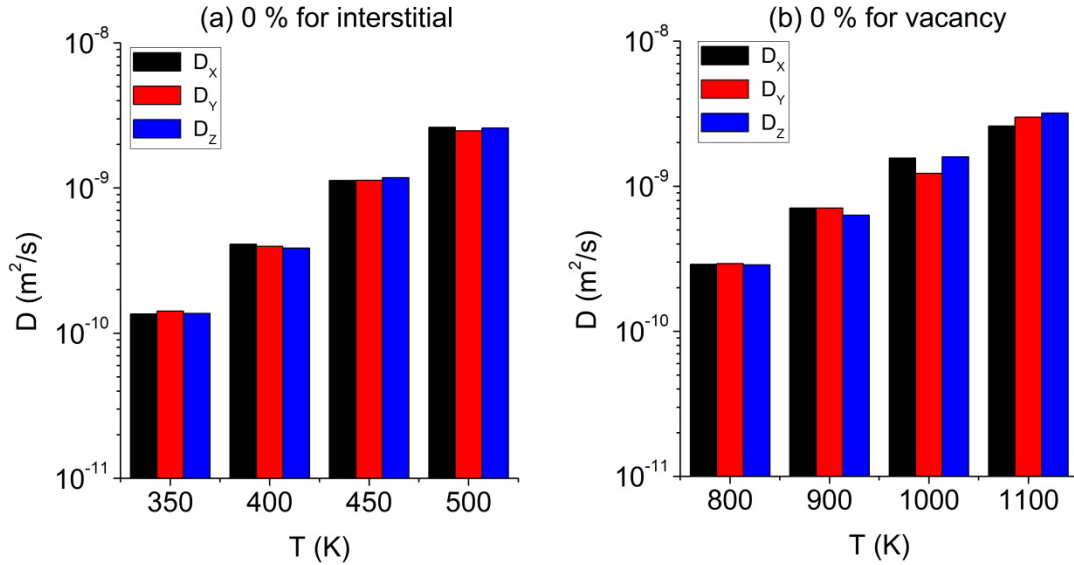


Fig. 2.2 Isotropic Diffusivities of 1-SIA and vacancy under 0% strains: (a) Diffusivities under 0% strain for 1-SIA (b) Diffusivities under 0% strain for vacancy.

Figure 2.2 shows the isotropic diffusivities along x, y, and z-directions for single SIA and vacancy under 0% strains. The three orthogonal axes of the bcc crystal are set as  $[1-10]$ ,  $[-1-12]$ , and  $[111]$  for the x-, y-, and z-axis, respectively. Under zero strain, the diffusivities are similar along the three directions. However, the diffusivity starts showing significant variances along different direction when the applied tensile strain reaches 1%, diffusivity is highest along the z-direction. The z-direction is also the direction of the applied strain. It is shown that SIA diffuses faster along the directions parallel to the strain direction, and slower along the perpendicular to the strain direction. As the tensile strain increases from 1 to 3%, the anisotropy becomes even more

significant. Under 3 % tensile strain, the SIA migrates nearly in 1D along the applied strain direction, which has low migration energy as shown in Figure 1 and Table I.

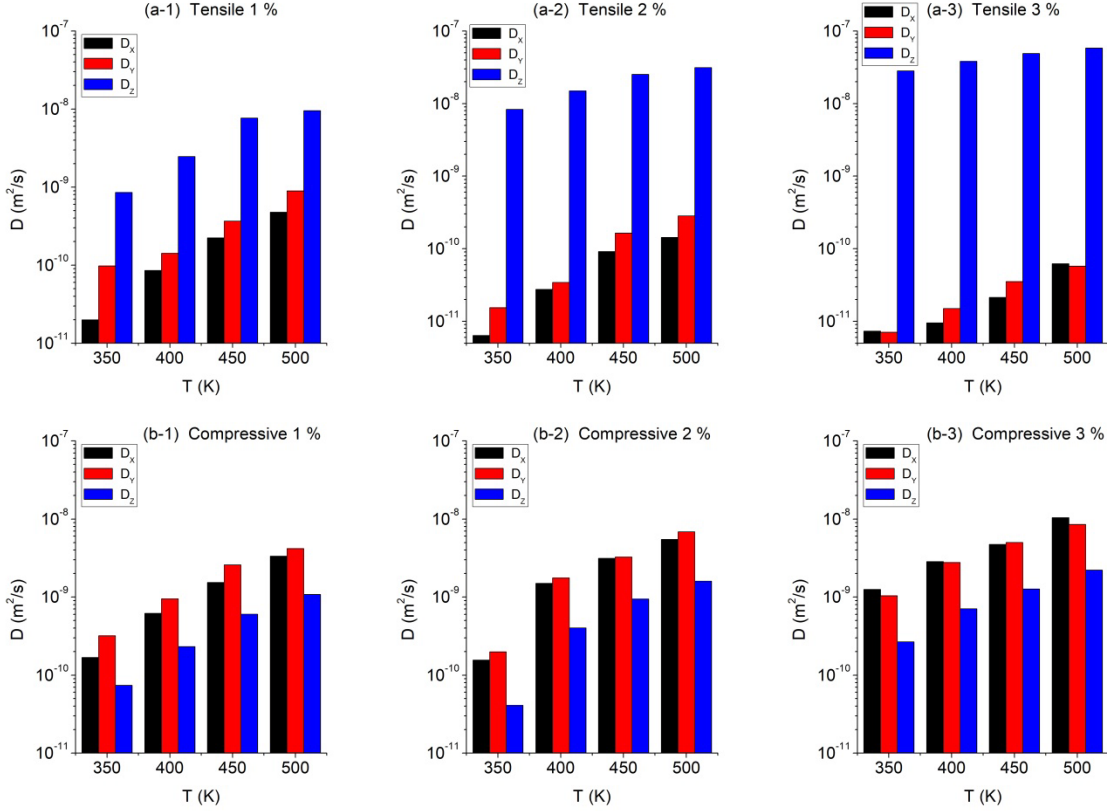


Fig. 2.3 Anisotropic Diffusivities of 1-SIA under different uniaxial tensile and compressive strains along [111]: (a-1) Tensile strain 1%, (a-2) Tensile strain 2%, (a-3) Tensile strain 3%, (b-1) Compressive strain 1%, (b-2) Compressive strain 2%, (b-3) Compressive strain 3%.

Figure 2.3 shows the diffusivities of single SIA along different directions under compressive strains. Unlike the tensile strain cases, the SIA's diffusivity does not differ significantly between different directions. Slightly decreasing diffusivities are obtained under 3% compressive strain. The tendencies are reversed with the case for tensile strains. The defect has lower diffusivity along the applied strain direction, which is z-

direction in these cases. Diffusivities of SIA are similar along the two directions perpendicular to the applied strain direction. The slight differences may come from the stochastic nature of diffusion. Thus, SIA migrates with 3D anisotropic diffusion.

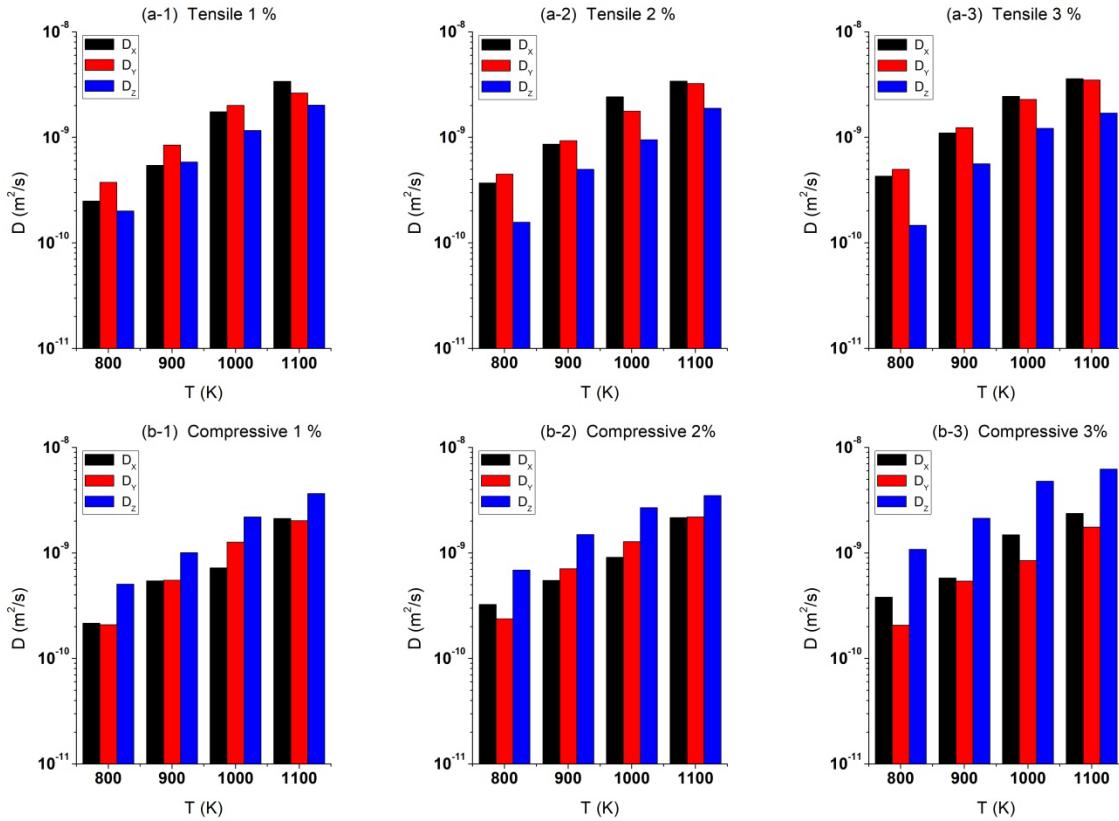


Fig. 2.4 Anisotropic Diffusivities of vacancy under different uniaxial tensile and compressive strains along [111]: (a-1) Tensile strain 1%, (a-2) Tensile strain 2%, (a-3) Tensile strain 3%, (b-1) Compressive strain 1%, (b-2) Compressive strain 2%, (b-3) Compressive strain 3%.

It can be seen that the effect of stress on SIA and vacancy diffusion is opposite. Diffusivities of vacancy along different directions and under different strains are measured and plotted in Figure 2.4. At zero strain, the vacancy diffuses almost

isotropically with similar diffusivities as shown in figure 2.2 (b). As strain increases, the anisotropic diffusivity also increases. Under tensile strains, the diffusivities along x- and y-directions, which are perpendicular to the applied strain z-direction, are higher than that along the z-direction. Meanwhile, the compressive strains produce opposite results. The vacancy migrates faster along the applied compressive strains instead. Unlike the case of SIA, the diffusion of vacancy is anisotropic, but almost 3 dimensionally under both strains. The anisotropy of vacancy diffusions is less than that of SIA under same type and magnitude of strain.

### 2.3.2 Displacement cascade

Displacement cascade under both ion irradiation and different strains are investigated. In this section, we examine how the anisotropic diffusion affects the initial damage production. The applied uniaxial strains are between -2 % (compressive) to +2 % (tensile). Here, we also study isometric strains, which are volume conserving strains. Previous studies have reported that one of the main causes of the different defect production is due to the volume change of material [7]. Therefore, by applying isometric strains, the effect of anisotropic diffusion on damage production can be examined without volume change [11].

Figure 2.5 shows the average number of interstitials and vacancies under different uniaxial strains along [111]. The total number of interstitials, which are represented by the Freely Migrating Defects (FMD), has significant differences at each strain. Both compressive and tensile strains cause the number of interstitial defects to

increase significantly. The number of defects under tensile strain is higher than that under compressive strains, with the same strain magnitude. Vacancy also shows similar behavior. The error bars in Figure 2.5 represent the standard deviation of numbers of defect produced -divided by square root of the number of simulations conducted.

Figure 2.5 also shows the size of different interstitial and vacancy-defects such as mono-interstitial (vacancy), di-interstitials (vacancies), and clusters that are larger than three-interstitials (vacancies). When the uniaxial strain is less than 1 %, mono-interstitials increase in both strain types. The increase of mono-interstitials governs the total increase of defects. On the other hand, under the high strain level (2 %) in present work, the number of mono-interstitials does not affect the increase of the FMD. Even, the number of mono interstitials decreases slightly at 2% uniaxial tensile strain. The increase of the FMD is mainly caused by the increase of interstitial clusters populations. For the vacancy case, the number of mono-vacancy increases with tensile strains, which causes the increase of the FMD. Di-vacancies and vacancy-clusters also increase slightly under both compressive and tensile strain conditions. As compressive and tensile strains increase, the number of clusters and their size increase. These increased number and clustering would aggravate the radiation damage by influencing the evolution of microstructure, which would affect the formation of dislocation loops or voids in long-term [10, 11, 15].

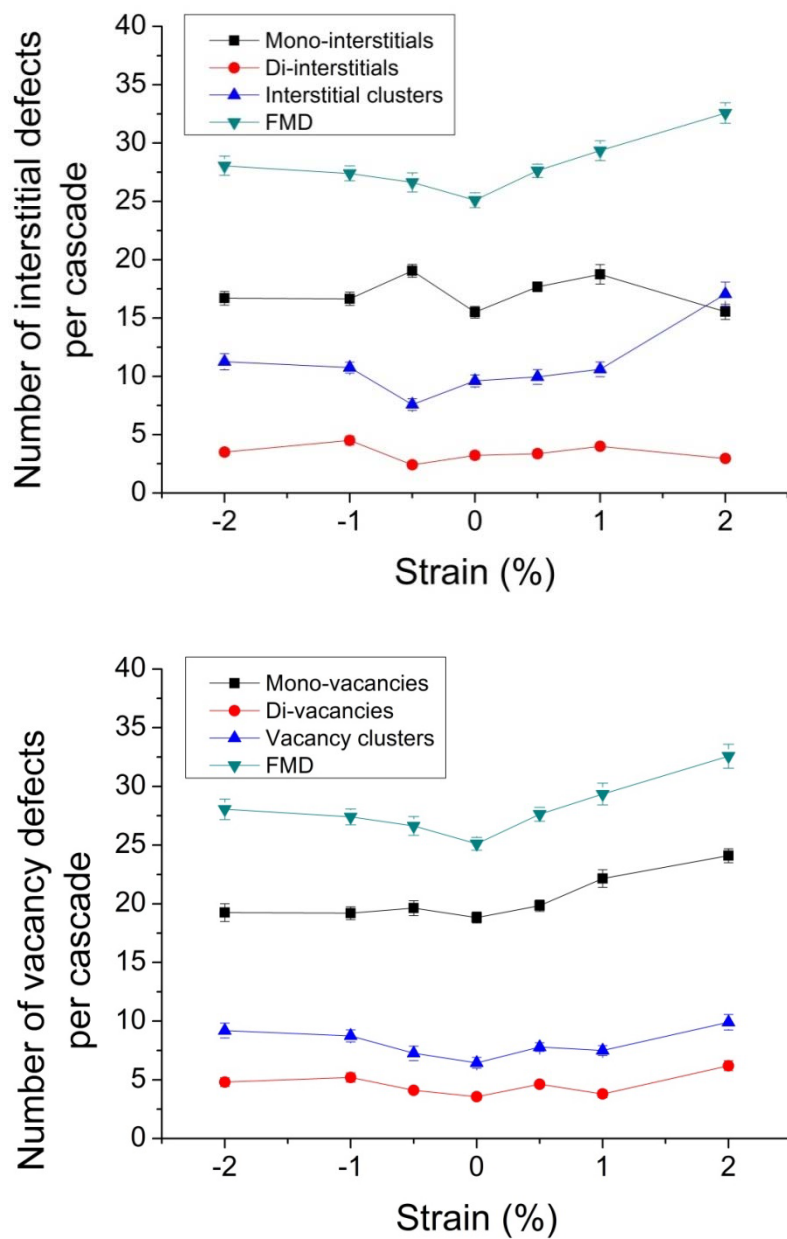


Fig. 2.5 The average number of interstitial defects (above) and vacancy defects (below) under different uniaxial strains along [111].

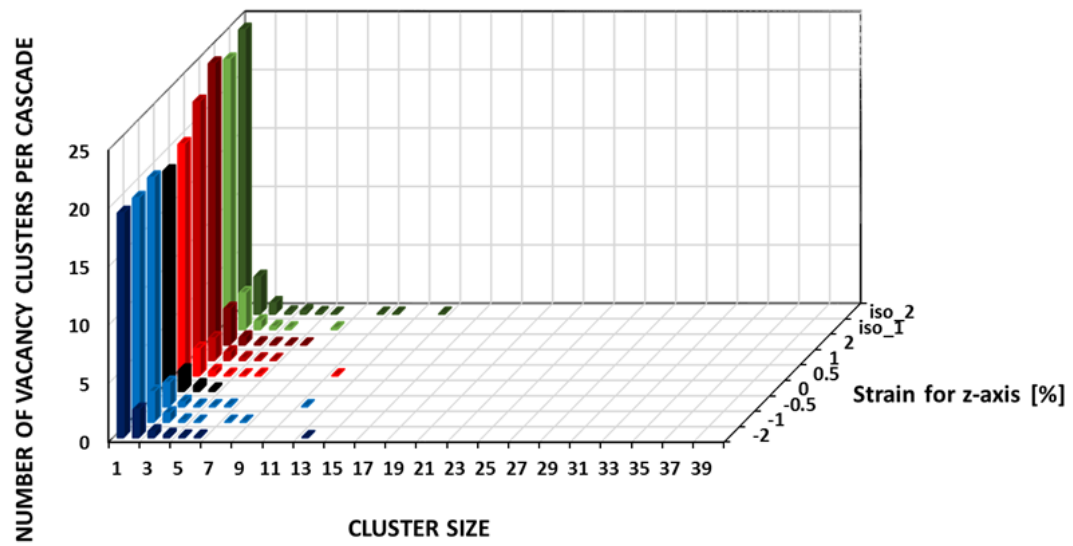
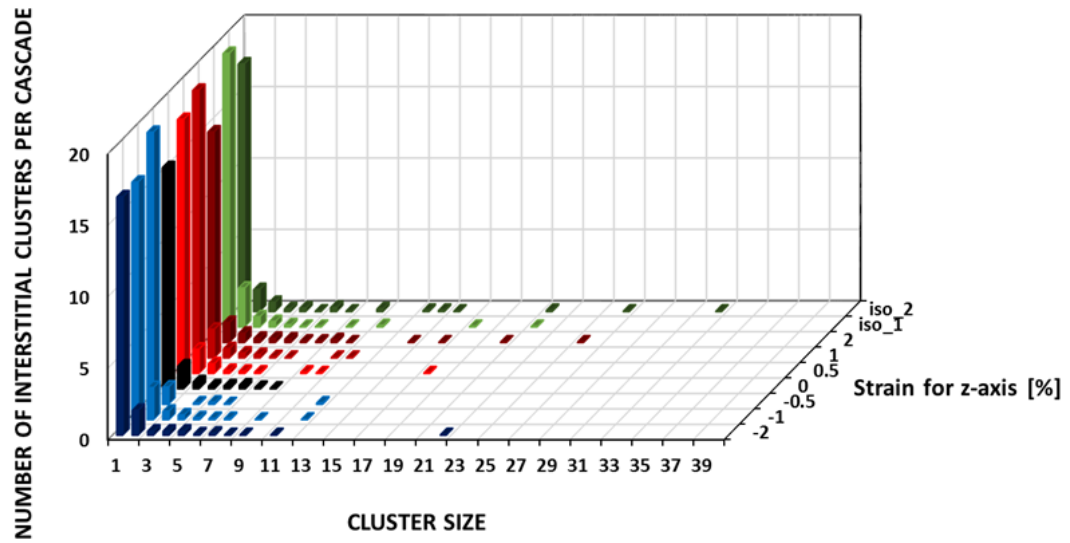


Fig. 2.6 Interstitial and vacancy cluster distribution under different strain types and levels.

Figure 2.6 shows the detailed size distributions of interstitials and vacancies produced under uniaxial strains along [111] by -2% to 2%, and isometric strains by 2%. For 2% isometric conditions, strain for z-axis is set to 2%, and strains for x- and y-axis are set to -1 %. In Figure 2.6, the uniaxial strains along [111] are presented by the strain levels -2 % to 2%, where the iso\_1 and iso\_2 indicate the isometric strains by 1% and 2%, respectively. For isometric strains, the volume is conserved, however, deformation is increased by the strains [11]. Under 0% strain, the mono-interstitials and small sizes of interstitial clusters are produced. As the level of uniaxial strain increases, the larger clusters are easily created. For the isometric strains, even larger sizes of interstitial clusters are generated. The result shows the importance of lattice distortion for the clustering of damage cascades. Cluster sizes for the vacancy have similar tendencies with those of interstitial. Under uniaxial strain and isometric strain along [111], they also create the larger size of vacancy clusters. The vacancy cluster sizes are smaller than those of interstitial clusters under all strain conditions in this work.

As discussed by S. Miyashiro et al. for Cu [11], we also calculate the ratio of FMD to NRT by using the widely used NRT equation (2-1) [19].

$$N_{NRT} = 0.8 \frac{E_{dam}(E_{PKA})}{2E_d} \quad (2-1)$$

Where, the  $E_{dam}$  and  $E_{PKA}$  mean the damage energy and the PKA energy, respectively. We used 10 keV for both, due to the MD simulation does not account for the energy loss by electronic excitation and ionization [15]. The  $E_d$  is the displacement energy, which was used with 40 eV in this calculation. Thus, the  $N_{NRT}$  value is obtained to 100.

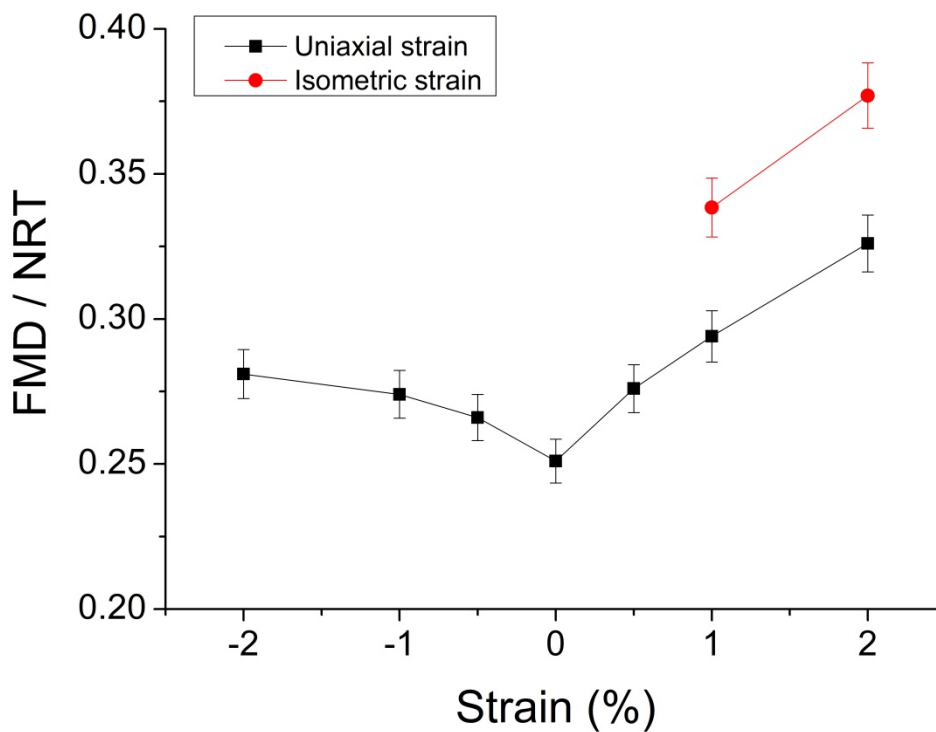


Fig. 2.7 The ratio of FMD to NRT under different strains.

Figure 2.7 shows the FMD divided by the NRT for each strain conditions. Uniaxial compressive and tensile strains show the increase in the ratio. For the uniaxial tensile strains, the values are higher than those of compressive strains. At 2 % uniaxial strains, the ratio is increased by 30 % of those at 0 % strain. For the isometric strain (2%), the ratio of FMD to NRT increases significantly by 50 % compared to those at 0% strain. These tendencies are similar to the results of S. Miyashiro et al. [11]. Present work explains the importance of deformation anisotropy on the strain effect of defect production. It also indicates that the general tendencies for effect of deformation anisotropy caused by strain are similar between BCC-Fe and FCC-Cu.

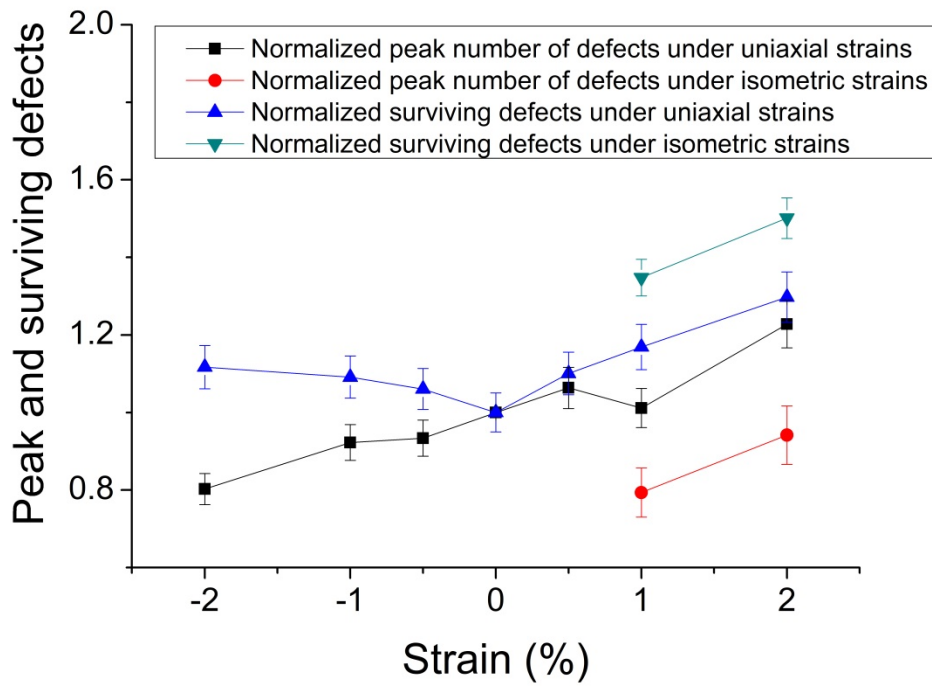
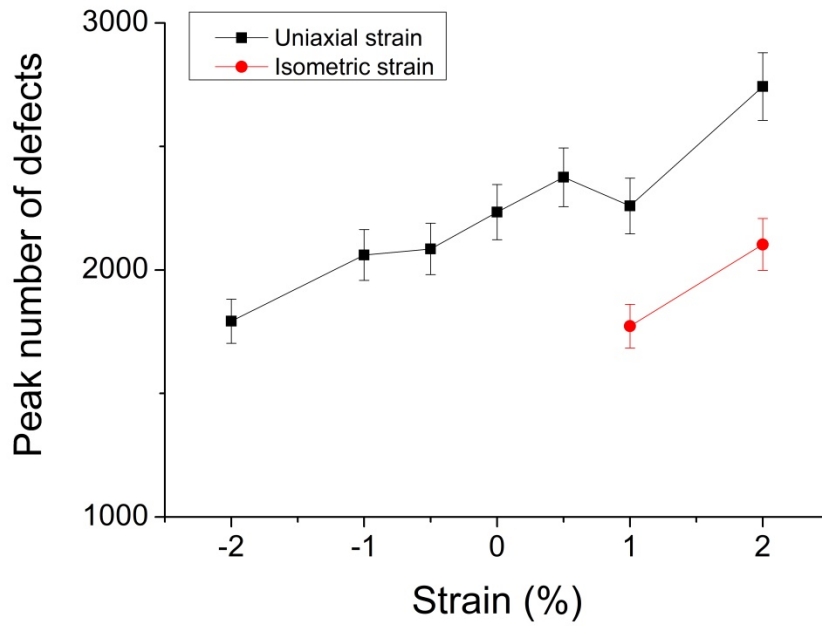


Fig. 2.8 Peak number of defects formed during displacement cascades under different strains (up) and the fraction of surviving defects and peak numbers normalized by those of 0% strain (down).

We also investigate the initial damage evolution under different strains in MD. In order to examine the differences of damage evolutions, the peak number of defects, average peak time, fractions of surviving defects (which are the ratio the peak number to the FMD at initial annealing stage of the cascade), and recombination rates are investigated. Figure 2.8 presents the peak number of defects created during displacement cascades (up) and the peak number and surviving defects normalized by those of 0 % strain (down). From uniaxial compressive to tensile strains, the peak number of defects increases except for 1 % tensile strain due to statistical consequence. However, the trend is generally increased. This result can be inferred from the formation energy or the threshold energy under uniaxial strains. The compressive and tensile strains produce high and low formation or threshold energies compare to that of 0 % strain, respectively [7, 8]. Thus, the peak number of defects increases under uniaxial tensile strains. For the isometric strains, the peak numbers are less than the value of 0 % strains. In the previous section, we discussed that the number of final stable defects under isometric strains is higher than that under uniaxial strains. Under isometric strains, the lowest peak number is obtained, though it produces the highest FMD finally. This result is the opposite knowledge of general investigations under 0% strain. If PKA energy is high, the peak number of defects and the number of stable defects are obtained during the initial evolution of displacement cascade [15].

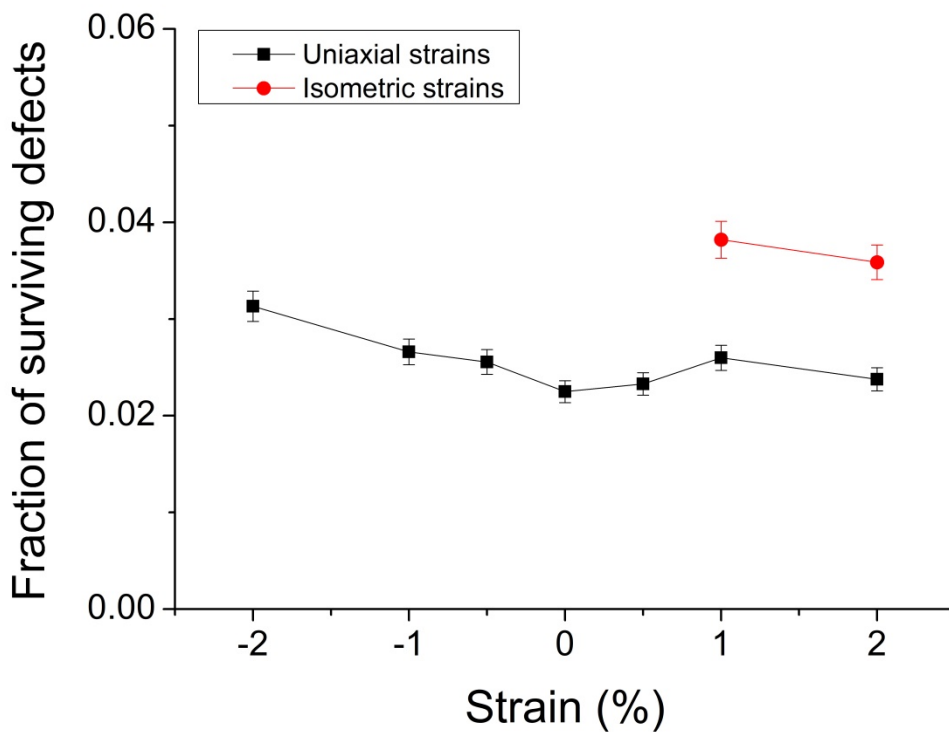


Fig. 2.9 Fraction of surviving defects to peak number formed during displacement cascades under different strains.

Figure 2.9 shows the fraction of peak number to surviving defects under different strains. The ratios under both uniaxial strains are higher than that under 0 % strain. As we discussed above, the fractions for the isometric strains are even higher than those under uniaxial strains and that at 0 % strain. Under isometric strains, the anisotropy affects the recombination rate and surviving ratio. The anisotropy makes defects difficult to recombine. This will be discussed later section.

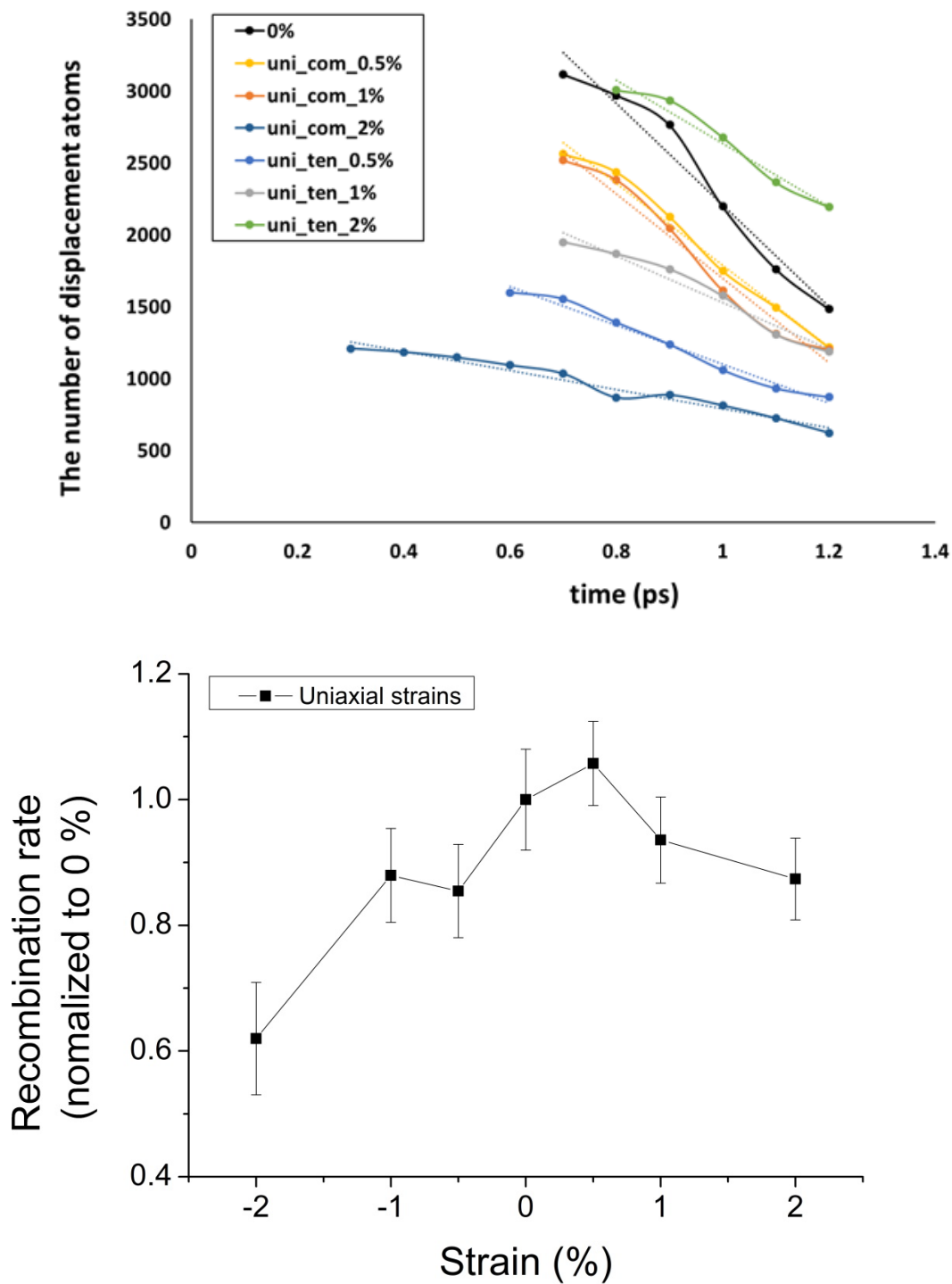


Fig. 2.10 Recombination rates for specific time after creation of peak numbers.

Figure 2.10 shows the recombination rate of defects after achieving the peak number. The reduced number of defects is calculated during the time from a peak to 1.2 ps. The recombination rates are varied significantly under strains. The result shows both strains (tensile and compressive) cause fewer recombination rates during the measured time. As shown in figure 2.10, the recombination rates for the compressive strains are lower than those of tensile strains.

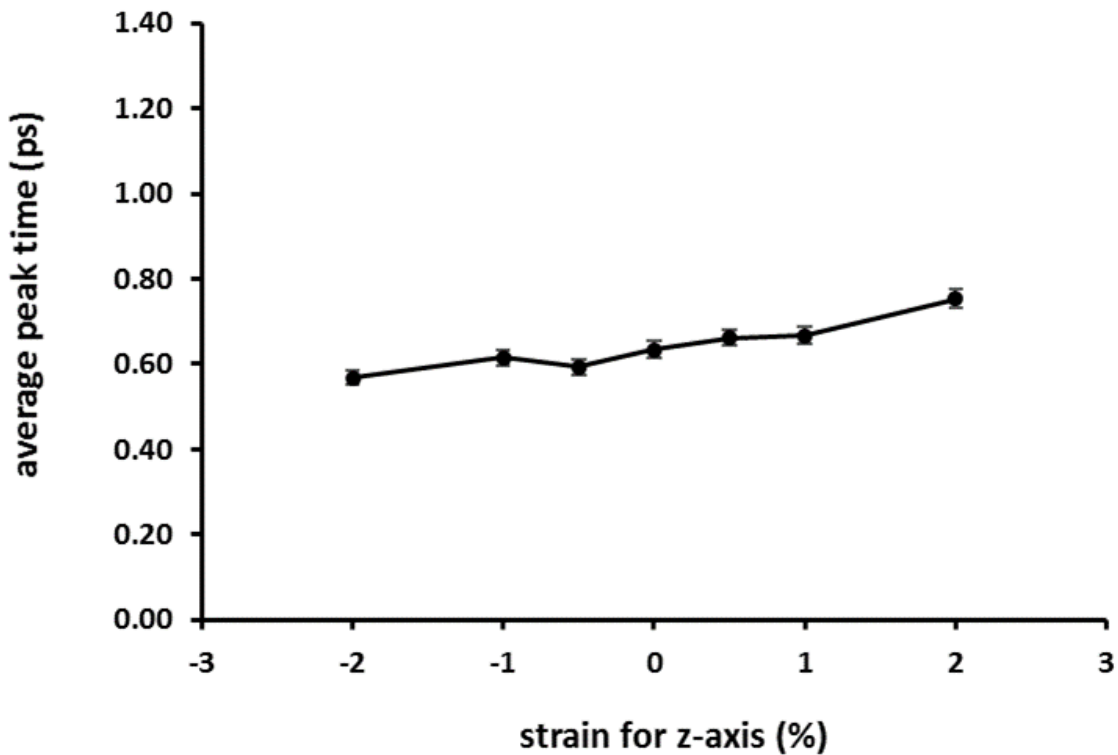


Fig. 2.11 Average peak time under uniaxial strains along [111].

Figure 2.11 shows the average peak time under uniaxial strains from -2 to 2%. The average peak times are increased from compressive to tensile strains generally. It is related to the formation or displacement threshold energy. Less energy for formation or

threshold could have the more generation of defects and keep the time of thermal spike. Thus, the average peak time is increased.

## 2.4 Discussion

Previous works have reported that the formation and displacement threshold energy under hydrostatic and uniaxial strains were the reasons for making differences in the number of produced defects [6-8, 10, 47]. Under uniaxial strains, the variances of both formation and displacement threshold energies are small and other factors may also influence the differences of defect production. Wang et al. [10] suggested the recombination stage would be a possible reason. We discuss the possible reasons for the differences in the number of surviving defect, focusing on recombination rates with regard to anisotropy diffusion, migration energy, and alignment of defects.

Present work indicates that uniaxial strains along [111] affect the defect production and clustering significantly. The results are different from Beeler et al. works, which used the uniaxial strains along [001] and showed no statistically significant effect on the number of defects under low uniaxial strains by 2 % [7]. In addition, they reported no significant changes of defects generation under tetragonal shear strains, which are the same as the isometric strains in this work. The main differences are due to the lattice distortion caused by different strain directions. The applied strains along [111] in present work create more distortion in the bcc structure. The distortion causes the anisotropy of the migration of defects and reduces the migration energy, which may affect the recombination stage. The anisotropic diffusion of defect reduces the

recombination of interstitials and vacancies. The interstitials and vacancies produced by a series of collisions are difficult to recombine with the 1D migration of defects compared to 3D migration. Hence, the distortion of structure and the anisotropy of diffusion under strains provide the increased surviving defects significantly compare to that of 0% strain. Those anisotropy diffusions for the interstitials and vacancies are different with strain types and levels. Present work shows less recombination under compressive strains so that the ratios of the peak defect number to surviving defects are slightly higher under compressive strains than those under tensile strains as shown in figure 2.9. Under tensile strains, the interstitials diffuse 1D, which can decrease recombination between interstitials and vacancies. However, the interstitials have low migration energy, 0.7 eV for 3 % tensile strain and high diffusivities, which can increase the recombination with neighbor vacancies. The 1D diffusion and reduced migration energy are also related to the defect alignment. The larger tensile strains, the higher fraction of SIA aligned to [111] direction [8, 10, 44]. The tensile/compressive strains create more/less aligned SIAs along [111] direction, respectively [10]. The alignment under tensile strain makes the interstitials easy to jump to the closed packed direction, which is same as the applied strain direction in the present work. Thus, the alignment reduces migration energy under the tensile strain as shown in figure 2.8. Finally, the low migration energy leads to high diffusivity, which would cause the increased recombination. However, for the compressive strain, interstitials are aligned along other  $\langle 111 \rangle$ , which are not parallel to the strain direction. Under compressive strain along

[111], the migration energy also decreases, but the energies are higher than those under tensile strains at same levels as shown in figure 2.8 and table 2.1.

The combination effects of anisotropy diffusion, the reduced migration energy, and alignment along applied strains make the ratios under tensile strains are slightly less than those under compressive strains. This result tells the importance of structure distortion beyond the effect of formation and threshold energies under uniaxial strains along [111] during recombination stage. The volume conserving strain (2%) generates about 50 % more defects compare to that of unstrained work (0%). The result of isometric strains, which have huge distortions, also supports the importance of anisotropy deformation on recombination stage. The results might be useful to understand the mechanisms of irradiation creep contributed the stress induced preferred nucleation (SIPN) and stress-enhanced swelling [11, 48-51]. The alignment of the defect along strain direction produces a defect cluster or loop with same Burgers vectors. The SIA clusters have high dissociation energy, so the aligned cluster or loop would affect the irradiation creep strain in the material [11].

## 2.5 Conclusion

We study the effects of strain on the damage production in pure bcc-Fe using MD simulation. We find that the changes in the number of defects produced, and the cluster sizes are significant under strains along [111]. The volume change due to the applied strain has been known to be the driving force for making a difference of defect generation. The volume change leads to the change of displacement threshold energy and formation energy. Those are directly related to the peak number of defect in the evolution of displacement cascade. 2% isometric volume conserving strain along [111] causes a 50% increase in the number of defects produced, which shows the importance of anisotropy in the defect generation. We also investigate the peak number, the ratio of the peak to surviving numbers of defects, and the recombination rate under different strain conditions along [111]. We clarify that the combined effects of diffusion anisotropy and different migration energies under strains are the reasons for different recombination rates in recombination stage of the evolution of defects, which lead to varying number of surviving defects in displacement cascade of bcc-Fe. This result can be useful to understand the effect of strains on displacement cascade stage and the initial stage of annealing in MD scale. The calculated diffusivities and migration energies under strains along [111] also can be used in multi-scaling computational works.

## CHAPTER III

# KINETICS OF INTERSTITIAL DEFECTS IN FE: THE EFFECT FROM UNIAXIAL STRESS\*

### 3.1 Introduction

Numerous theoretical studies have been performed to obtain formation/migration energies of defects in alpha Fe by using molecular dynamics (MD) simulations, density function theory (DFT) and kinetic Monte Carlo simulations [39, 45, 46, 52-59]. The defect kinetics are needed for multiple scale modeling of defect evolution in stainless steels for reactor applications. Majority of previous studies were limited to stress-free conditions. A few simulation studies considered the effect of stress on the defect generation and defect clustering in the early stage of displacement cascade formation and evolution [6-8]. A few limited atomic scale simulations were performed to compare the diffusion behaviors under stress [55, 60, 61]. Ab-initio calculations were employed to investigate the stability and mobility of single SIA in alpha Fe under external deformation [62]. Previous studies also considered the changes of energy barrier for impurity diffusion under stress [55, 61, 63].

For all previous studies on stress effects on defect formation and defect migration in alpha Fe, they were limited to single self-interstitial atom (SIA). The lack of knowledge on SIA clusters (containing more than one SIA) has been an issue for multi-

---

\*Reprinted with permission from “Kinetics of interstitial defects in  $\alpha$ -Fe: The effect from uniaxial stress” by Changwoo Kang, Qingyu Wang, Lin Shao, 2017. Journal of Nuclear Materials, Volume 485, Page 159-168, Copyright [2017] by Elsevier B.V.

scale modeling of defect development under conditions combining neutron damage and stress. One example is creep deformation of fuel cladding when strong fuel and fuel cladding interactions develop under high burnup. Understanding SIA and SIA clusters' behaviors are important to develop multiscale modeling approaches involving the coupling of microstructural changes and mechanical property changes. Small SIA clusters form in damage cascade stage and they are important precursor defects to form large stable defect clusters. In this study, we investigate the formation and migration energies of SIA defects from single SIA to 5-SIAs under uniaxial strain. The present study considers large strain up to 3%, which is not uncommon for strain concentrated region at a cracking tip, which is one important degradation phenomenon for reactor in-core components. Stable defect configurations, defect formation/migration kinetics and diffusion mechanisms are discussed.

### 3.2 Methodology

We use LAMMPS [26] code for both molecular dynamics (MD) and molecular statistics (MS) simulations. MD simulations are used to simulate defect migration to extract diffusivity and diffusion energies as a function of temperatures. MS simulations are used to calculate defect formation energies of different defect configurations. The Fe interatomic potential used in the present study is an embedded atomic potential type and was developed by Mendelev *et al.* [43]. The potential was obtained by fitting to both ab initio total energy calculation results and experimentally measured properties. The supercell contains about 512000 Fe atoms and periodic boundary condition is applied. In

order to obtain migration energies, MD simulations are performed at temperatures from 350K to 600K, which are high enough to obtain sufficient defect mobility but low enough to avoid dissociation of defect clusters. Under a given temperature the cell is first relaxed in NVT ensemble, then following by NPH ensemble. A stress is applied to the cell along [111] direction, to maintain a constant strain. After stress loading, a thermal relaxation is allowed in NVT ensemble. The cell stretching along [111] direction leads to shrinkage in both  $[1\bar{1}0]$  and the  $[11\bar{2}]$  directions through a Poission's ratio of about 0.29. The time step during simulation is fixed to 0.2 fs. After equilibration to a fixed temperature, a NVE microcanonical ensemble is used to simulate defect migration for a time period up to 40 ns. The visual tool, OVITO [24], is used to record diffusion trajectories.

The migration energies of SIAs can be obtained by both MS and MD methods. For MS approach, the migration energies represent difference of total energy between the initial SIAs configuration and the SIAs at saddle points. Nudged Elastic Band (NEB) method is used to study the kinetics of transition from the initial position to the final position [64-66]. The MD approach is more computational costly but it provides atomic-level details of SIAs' dynamics. The MD approach does not pre-select migration paths, and the migration energies are obtained from temperature dependence of diffusivities. Diffusivities are determined by

$$D_N(T) = \frac{\overline{R^2(T)}}{2n_d t}, \quad (3-1)$$

where  $\overline{R^2}(T)$  is the mean-square displacement of the SIAs,  $n_d$  is the dimensionality of the motion (1 to 3), and  $t$  is the simulation time. The migration energies are extrapolated from Arrhenius expression,

$$D_N(T) = D_{0,N} e^{-E_m/k_B T} \quad (3-2)$$

where  $k_B$  is Boltzmann's constant,  $E_m$  is the migration energy, and  $D_{0,N}$  is a pre-factor. The data analysis follows the independent interval method in order to alleviate issue from limited computational time [45, 46, 54, 67, 68]. In this approach, the total simulation time is divided into  $K$  short time segments. For each time interval of  $\tau_K (= \frac{t}{K})$ , the square displacement  $\overline{R_t^2}$  is calculated and the diffusion coefficient is obtained by considering the average of their square,

$$D_N(T) = \frac{1}{K} \sum_{i=1}^K \frac{\overline{R_t^2}}{2n\tau_K}(T) \quad (3-3)$$

Care must be taken to appropriately select  $\tau_K$ , as discussed by Terentyev *et al.* [46]. The time interval  $\tau_K$  must be long enough to include local correlations of defect motion (i.e. allowing diffusion in back and forth directions for 1-D diffusion), but not too long to significantly increase total computation time. Previous study show that obtained diffusivity decrease with increasing  $\tau_K$ , and become saturated for longer  $\tau_K$ . The shortest  $\tau_K$  to reach such saturation should be used in order to minimize statistic error and maximize computational efficiency [46]. In the present study, we use  $\tau_K$  of 3.3 to 400 ps depending on the defect sizes and temperatures.

### 3.3 Result and discussion

Many previous studies have been performed to understand diffusion mechanisms and obtain defect kinetics of SIAs and SIA clusters in  $\alpha$ -Fe and other metals [39, 41, 45, 46, 52, 53, 56, 57, 59, 69-74]. All these studies are limited to zero-strain conditions. Table 3.1, 3.2 and 3.3 compare the structures of small SIAs, formation energies and migration energies from the present study with selected previous works (Table 3.1 and 3.2 for 0% strain), although the major focus of the present work is for non-zero strain conditions.

Table 3.1 shows the structures of small SIAs identified from the MD simulations. The OVITO is used for visualization [24]. The structures of 1-5 SIAs under strain free condition are consistent with previous studies [45, 52, 72]. For 1-SIA and 2-SIA, only  $\langle 110 \rangle$  is observed during migration. For 2-SIA,  $\langle 110 \rangle$  sessile configuration is observed, which is featured with low diffusivity and high migration energy barrier at low temperatures (less than 500 K).  $\langle 110 \rangle$ ,  $\langle 111 \rangle$ , and sessile configurations are observed during the migration for 3-SIA and 4-SIA. The 4-SIA sessile configuration is relatively immobile. For 5-SIA, only  $\langle 111 \rangle$  is observed. Defect configurations may change at different temperatures and under different simulation times [45]. More detailed descriptions of SIA structures under strain free condition can be founded in previous studies [45, 52, 53, 72].

The main differences between strain free and  $[111]$  strained conditions are alinement directions of defects. The 1 to 5 SIAs prefer to be aligned parallel to  $[111]$ . At 0% strain, the 1-SIA can take any  $\langle 110 \rangle$  configuration. However, under  $[111]$  strain,

only specific  $\langle 110 \rangle$  configuration is preferred, which has small angle away from the  $[111]$  strain direction. Unlike strain free condition, 1-SIA under the strain prefer to have  $\langle 111 \rangle$  configuration aligned with  $[111]$  direction. For 2-SIA,  $\langle 110 \rangle$  and  $\langle 111 \rangle$  configurations are observed. However, under high strain, the sessile configurations are not observed. The absence of sessile configurations leads to high diffusivities. For 3-SIA,  $\langle 110 \rangle$ ,  $\langle 111 \rangle$  and sessile configuration are all observed. The sessile configuration is observed under 1% strain at 400 K. The sessile configuration is highly immobile, similar to the 4-SIA sessile configuration at zero strain. For 4 and 5-SIAs, only  $\langle 111 \rangle$  configuration is observed under strain. As strain increases, small SIAs prefer to have  $\langle 111 \rangle$  rather than  $\langle 110 \rangle$  configurations.

Table 3.2 and 3.3 show formation energies and migration energies of 1-SIA to 5-SIA, respectively. Formation energies of 1-SIA to 5-SIA are in good agreements. With increasing defect cluster sizes, formation energies are increasing. In consistent with these previous studies as shown in table 3.2, the present study shows that  $\langle 110 \rangle$  configurations are energetically more favorable than  $\langle 111 \rangle$  configurations. For SIAs of size from 1 to 3, the energy difference between  $\langle 111 \rangle$  and  $\langle 110 \rangle$  is about 0.5 eV. As for the migration energies (as shown in table 3.3), they are generally decreasing with increasing sizes. Migration energies obtained from Soneda *et al.* and Marian *et al.* have relatively large differences from others, due to different potentials used [55, 59]. In generally, our results are in good agreements with previous studies [45, 46, 72].

Table 3.1 Observed configurations of 1-SIA to 5-SIA under strain free and strains along [111].

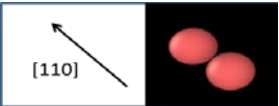
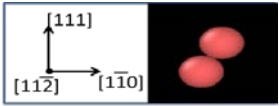
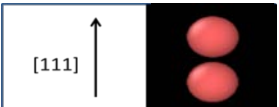
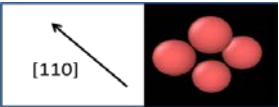
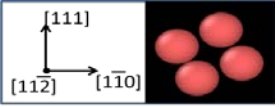
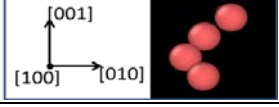
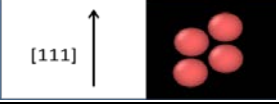
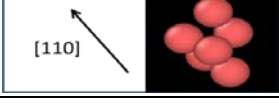
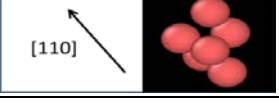
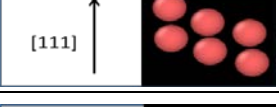
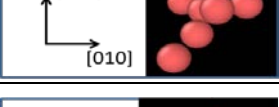
	0% strain		Tensile strains along [111] : 1 to 3 %	
1-SIA	<110>		<110>	
	-	-	<111>	
2-SIA	<110>		<110>	
	Sessile		<111>	
3-SIA	<110>		<110>	
	<111>		<111>	
	Sessile		Sessile	
4-SIA	<110>		-	
	<111>		<111>	
	Sessile		-	
5-SIA	<111>		<111>	

Table 3.2 Formation energies in eV for 1-SIA to 5-SIA under 0% strain.

Defect size	Config.	Present work	Anento <i>et al.</i> [45]	Terentyev <i>et al.</i> [46]	Marinica <i>et al.</i> [72]	Medelev <i>et al.</i> [43]	Willaime <i>et al.</i> [73]
1	<110>	3.52	3.57	3.52	3.52	3.52	3.75
	<111>	4.02	3.97	4.01	3.94	4.02	4.45
2	<110>	6.19	6.28	6.23	6.21	6.21	6.68
	<111>	6.73	6.86	6.76	6.74	6.74	7.43
3	<110>	8.85	9.00	8.87	8.84	8.84	9.49
	<111>	9.37	9.39	9.36	-	9.37	10.01
4	<110>	10.92	11.04	11.05	10.94	11.05	11.66
	<111>	11.07	11.18	11.22	11.14	11.36	11.77
5	<110>	13.24	14.12	13.42	-	13.25	14.18
	<111>	13.20	13.47	13.49	-	13.36	13.88

Table 3.3 Migration energies in eV (diffusion prefactors in  $10^{-8} \text{ m}^2/\text{s}$ ) for 1-SIA to 5-SIA under 0% strain.

Defect size	Present work	Anento et al. [45]	Terentyev et al. [46]	Soneda et al. [59]	Marinica et al. [72]	J. Marian et al. [55]	Fu et al. [57]
1	0.30(230)	0.27(83.1)	0.31(44.2)	0.167(20.9)	0.31	0.127 (19.4)	0.34
2	0.41(1970)	0.36(351.6) 0.44(4267) for (T ≤ 500 K) 0.19(19.7) for (T > 500 K)	0.33(243)	0.083(7.32)	0.33	0.084 (14.8)	0.42 0.43
3	0.13(11)	0.14(12.1)	0.14(3.35)	0.065(5.57)	0.33-0.38	0.074 (14.2)	0.43
4	0.14(17)	0.15(12.3)	0.16(3.11)	0.100(7.93)	0.05-0.14	0.07*	-
5	0.06(9)	0.05(8.6)	0.007(0.43)	0.066(4.82)	-	0.067*	-

\* The migration energy is deduced from their fitting equation.

Figure 3.1(a-d) compare the defect formation energies as a function of uniaxial tensile strain along [111] for 1-SIA to 5-SIAs, respectively. Both  $\langle 111 \rangle$  and  $\langle 110 \rangle$  configurations are considered. All defect formation energies decrease with increasing strain, but the magnitudes of changes are different.  $\langle 111 \rangle$  configurations are more sensitive to strain than  $\langle 110 \rangle$ . Hence, the energy gap between  $\langle 111 \rangle$  and  $\langle 110 \rangle$  configurations is reduced with increasing strain. As shown in Fig. 3.1a, the formation energies of  $\langle 111 \rangle$  and  $\langle 110 \rangle$  1-SIA under zero strain are 4.02 eV and 3.52 eV, respectively. At 3% strain, these two energies reduce to 3.19 eV and 3.14 eV, respectively. For 2-SIA,  $\langle 110 \rangle$  configuration is more favorable at zero strain. With increasing tensile strain, the energy gap between  $\langle 110 \rangle$  and  $\langle 111 \rangle$  configurations are reducing. At the highest strain of 3%, as shown in Fig. 3.1b, the formation energy of  $\langle 111 \rangle$  2-SIA is lower than  $\langle 110 \rangle$  2-SIA. For 3-SIA, switching of favorable configurations from  $\langle 110 \rangle$  to  $\langle 111 \rangle$  occur at 2% strain, as shown in Fig. 3.1c. For 4-SIA, such change occurs at even smaller strain  $< 0.5\%$  (Fig. 3.1d). For the largest defect 5-SIA,  $\langle 110 \rangle$  and  $\langle 111 \rangle$  configurations are comparable in formation energies for 0% strain. But adding even small strain makes  $\langle 111 \rangle$  configuration more favorable (Fig. 3.1e). For small defect clusters (1-SIA to 3-SIA), the formation energies of both configurations show almost linear dependence on strain. For large defect cluster such as 5-SIA, formation energies of  $\langle 110 \rangle$  configuration deviate from Arrhenius temperature dependence and show an accelerated energy drop at higher strain ( $>2\%$ ). It is worthy of the note that the trend of formation energy changes upon stress can be predicted by the elastic interaction between defects and applied stress fields. However, such estimation is

difficult to consider the complexity caused by anisotropic strain relaxation associated with defect clusters. For multiscale modeling, it is necessary to have quantitative kinetics information as shown in Fig. 3.1.

Under zero strain condition, there are two possible diffusion mechanisms for SIAs in  $\alpha$ -Fe. Figure 3.2 shows the migration mechanisms of A and B for 1-SIA. In the first mechanism (denoted as mechanism A),  $\langle 110 \rangle$  SIA(s) reorient to  $\langle 111 \rangle$  and then diffuse along  $\langle 111 \rangle$  direction. The migration energy is mainly contributed by the energy barrier required by reorientation [35, 39, 46, 52, 59, 71, 75]. In the second mechanism (denoted as mechanism B) which was first proposed by Johnson [76],  $\langle 110 \rangle$  SIA(s) rotate rigidly and translate to other  $\langle 110 \rangle$  SIAs on a different plane. Recent DFT and MD studies suggested that mechanism B is more favorable [45, 46, 56, 72]. One of interesting feature of the mechanism A is that 1-SIA can migrate with 1D resulted from the small formation energy difference between  $\langle 111 \rangle$  and  $\langle 110 \rangle$  configurations [46]. After one jump with the mechanism A, 1-SIA may translate consecutively without returning  $\langle 110 \rangle$  configuration due to small energy barrier for 1D migration [39, 52, 69, 75]. The mechanism B, on the other hand, leads to 3D migration [45, 46, 72].

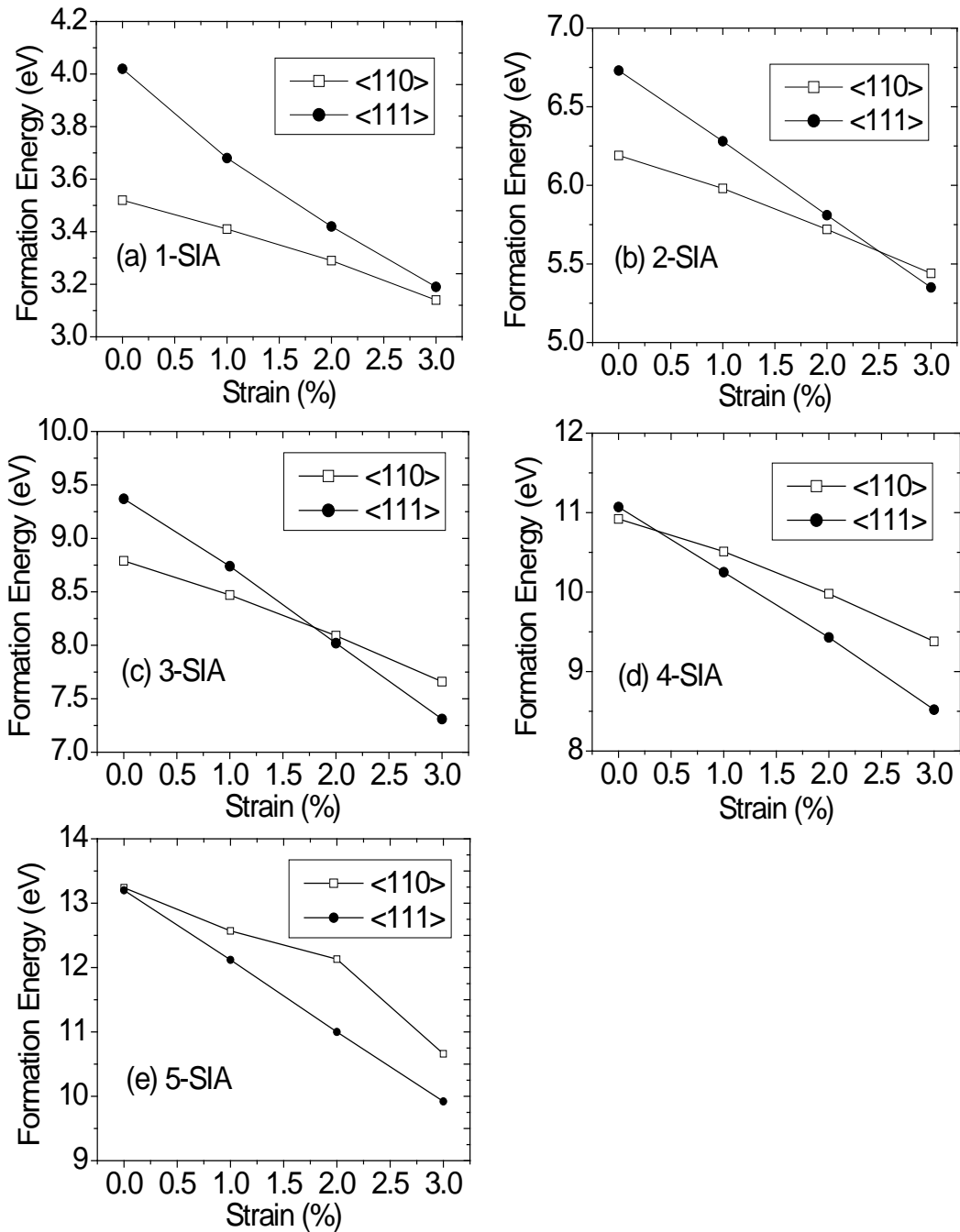


Fig. 3.1 Formation energies of  $\langle 111 \rangle$  and  $\langle 110 \rangle$  SIA defect clusters as a function of strain for cluster containing (a) single SIA, (b) 2 SIAs, (c) 3 SIAs, (d) 4 SIAs, and (e) 5 SIAs.

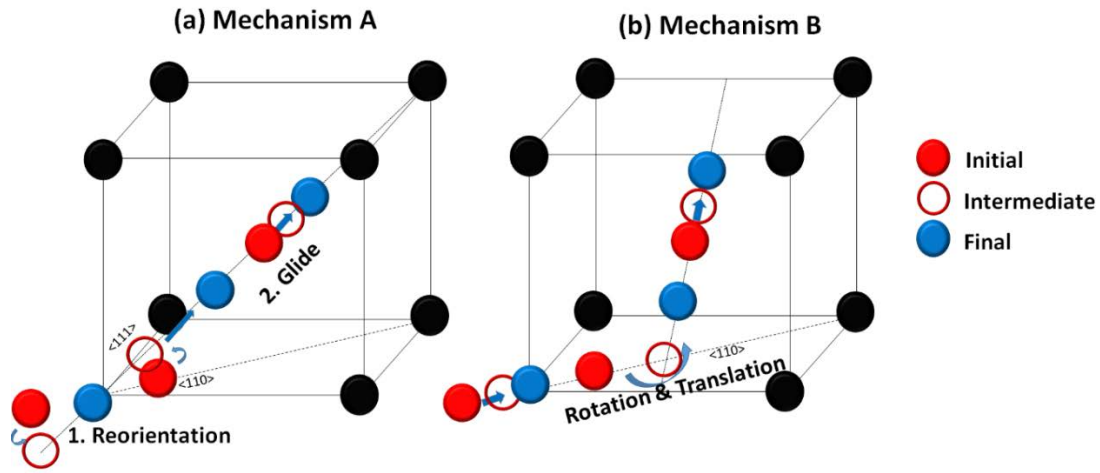


Fig. 3.2. Schematics of migration mechanisms for 1-SIA.

We calculate the energy barriers for the diffusion mechanisms A and B, as shown in Fig. 3.3a and 3.3b, respectively. Energy barriers are calculated by using Molecular Statics (MS) and Nudged Elastic Band (NEB) methods [64-66]. Fig. 3.3a plots the energy barriers for reorientation of  $\langle 110 \rangle$  to  $\langle 111 \rangle$  configuration in the mechanism A. Previous DFT calculation showed such reorientation is unlikely due to relatively high energy barrier ( $\sim 0.7$  eV) [56, 73]. In consistency, the present study obtains an energy barrier of 0.50 eV for  $\langle 110 \rangle$  to  $\langle 111 \rangle$  reorientation involved in the mechanism A, and 0.31 eV for  $\langle 110 \rangle$  to  $\langle 110 \rangle$  migration involved in the mechanism B. In comparison, F. Willaime et al. obtained 0.50 eV and 0.31 eV by using MD simulations, and 0.76 eV and 0.34 eV by using DFT calculations [56, 73]; Terenvey et al. obtained 0.57 eV and 0.34 eV by using MD simulations for mechanisms A (reorientation only) and B, respectively [46]. All these calculations show that mechanism B is energetically favored (0.31 eV). As the strain along [111] increases, the energy barriers decrease for both mechanisms and the barrier difference between two mechanisms is reduced as well. At 3% strain

along [111], the two mechanisms become comparable (0.214 eV vs. 0.184 eV). The energy barrier, 0.184 eV, is higher than the MD result, 0.07 eV (to be shown).

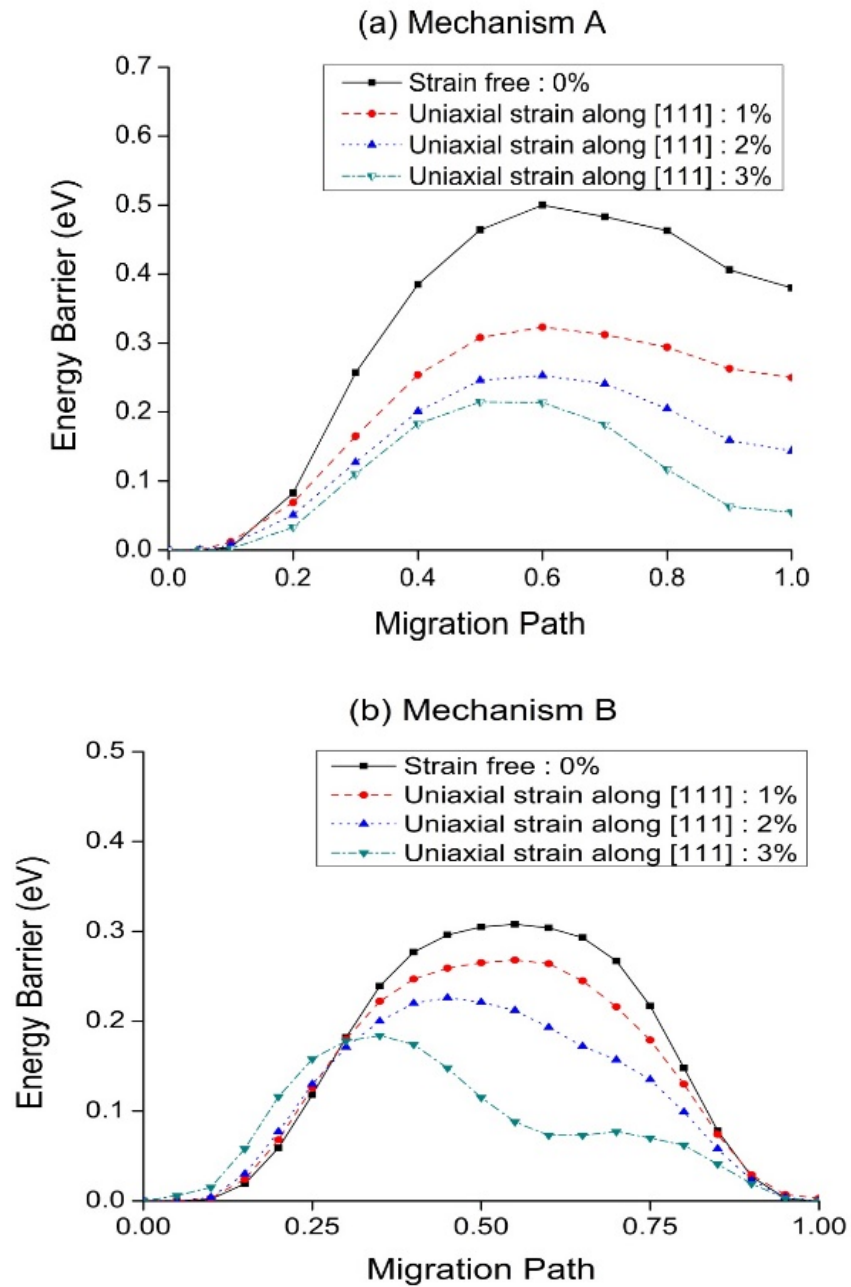


Fig. 3.3 The energy barriers of 1-SIA for (a) the migration mechanism A and (b) the migration mechanism.

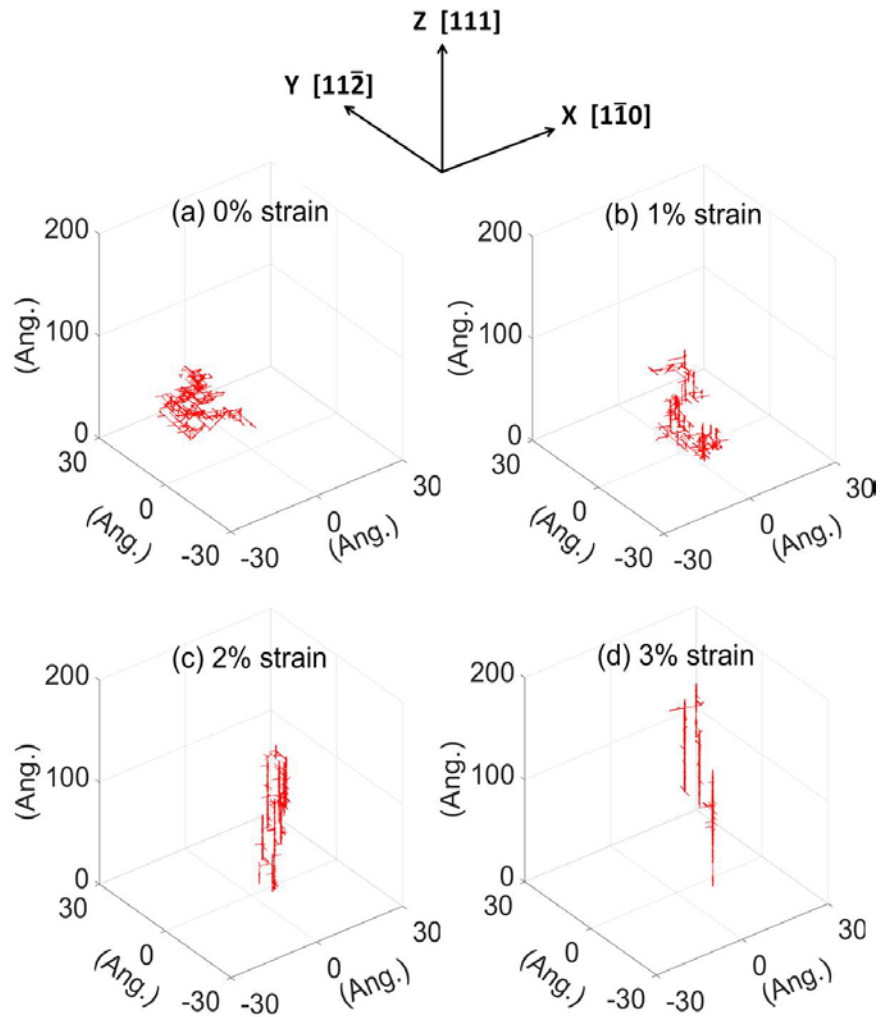


Fig. 3.4 1-SIA migration trajectories under different uniaxial tensile strains along  $[111]$  direction at 500 K.

Figures 3.4(a-d) compare single SIA migration trajectories under different tensile strains of 0%, 1%, 2% and 3%, respectively. The z axis is  $[111]$  direction, x axis is  $[1\bar{1}0]$  direction and y axis is  $[11\bar{2}]$  direction. The trajectories represent the movements of the center of mass of single SIA, used to calculate diffusion coefficient. As strain increases, the migration of 1-SIA gradually changes from 3D (Fig. 3.4a) to 1D (Fig. 3.4d). At 0%

strain, the 1-SIA have only  $\langle 110 \rangle$  configuration during the migration, which leads to 3D migration due to diffusion mechanism B. However, at 3% strain, deformation induced asymmetric structural distortion favors certain alignments of 1-SIA. That is, the 1-SIA has different formation energy for different  $\langle 110 \rangle$  configurations. It causes  $\langle 110 \rangle$  1-SIA to choose specific  $\langle 110 \rangle$  direction, which is aligned parallel to the strain direction [111]. Such alignment has been discussed before in simulation of cascade creation [8]. The 1D migration is due to the preference of parallel alignment of  $\langle 110 \rangle$  and  $\langle 111 \rangle$  1-SIA to [111] strain direction. Although it is difficult to tell from Fig. 4, visual inspection at much smaller length scales show that for strain  $> 2\%$ ,  $\langle 111 \rangle$  1-SIA may occasionally change to  $\langle 110 \rangle$  1-SIA. But  $\langle 110 \rangle$  1-SIA quickly changes back to  $\langle 111 \rangle$  and re-start 1D diffusion. The time duration to stay as  $\langle 110 \rangle$  configuration is much shorter at high strains. At highest strain of 3% the likelihood of  $\langle 111 \rangle$  to  $\langle 110 \rangle$  transition is further reduced. Diffusion is dominated by forward and backward movements along  $\langle 111 \rangle$  axis without returning back to  $\langle 110 \rangle$  configuration.

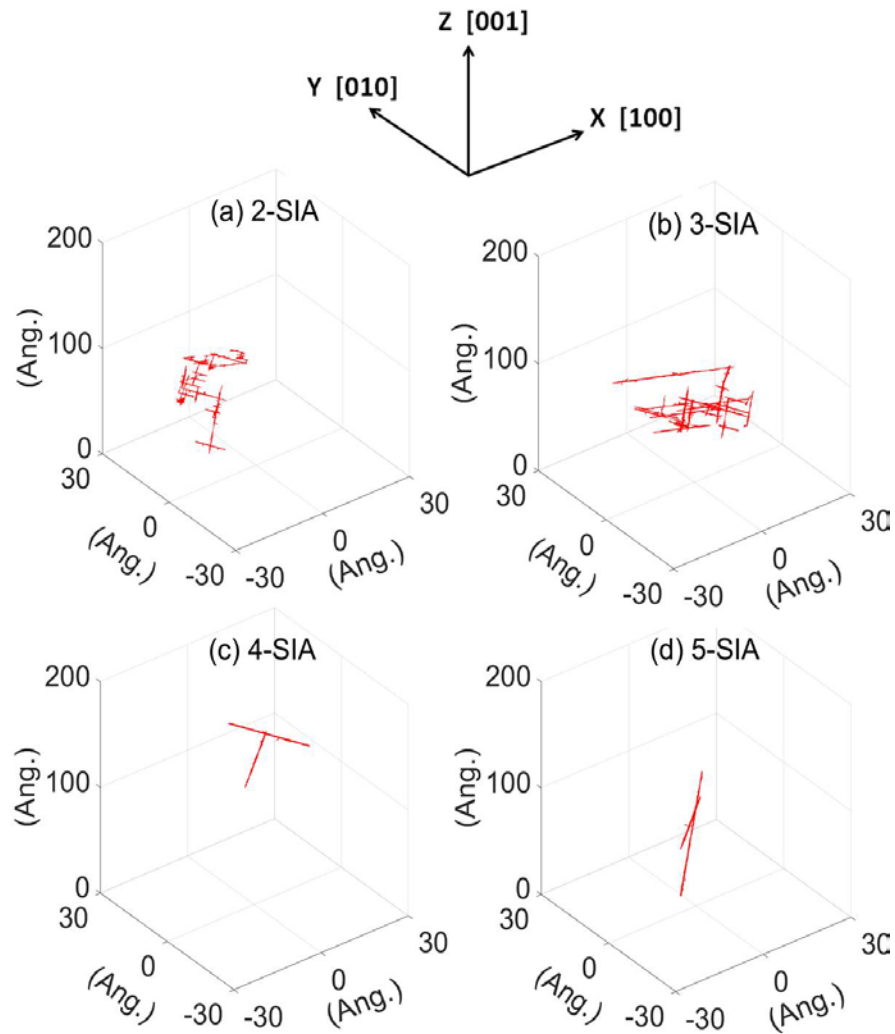


Fig. 3.5 Migration trajectories of (a) 2-SIA, (b) 3-SIA, (c) 4-SIA, and (d) 5-SIA under 0% strain at 500 K.

For defect clusters (from 2-SIA to 5-SIA), their diffusions under zero strain exhibit a transition from 3D (for small clusters) to 1D (for large clusters). Figure 3.5(a-d) plot the diffusion trajectories of 2-SIA to 5-SIA clusters. The x, y, z axes correspond to directions of [100], [010] and [001], respectively. All defect clusters show certain mixture of 3D and 1D diffusion. But their relative contributions to diffusion are sensitive

to cluster sizes. For 2-SIA, as shown in Fig. 3.5a, diffusion favors 3D migration. For 3-SIA, diffusion is still a mixture of 3D and 1D, but the contribution from 3D is decreasing, as evidenced by relatively longer migration distance (or equivalently, longer time duration) for 1-D migration along [111] axis, as shown in Fig. 3.5b. For larger clusters of 4-SIA and 5-SIA, as shown in Figs. 3.5c and 3.5d, 1D diffusion is dominant, featured by line-like diffusion trajectories. Defects may end its 1D migration by changing back to  $\langle 110 \rangle$  configuration. But  $\langle 110 \rangle$  SIAs immediately rotate into another  $\langle 111 \rangle$  configuration and start another [111] 1D diffusion. These motion of small SIAs are consistent with previous works under strain free condition [45, 46].

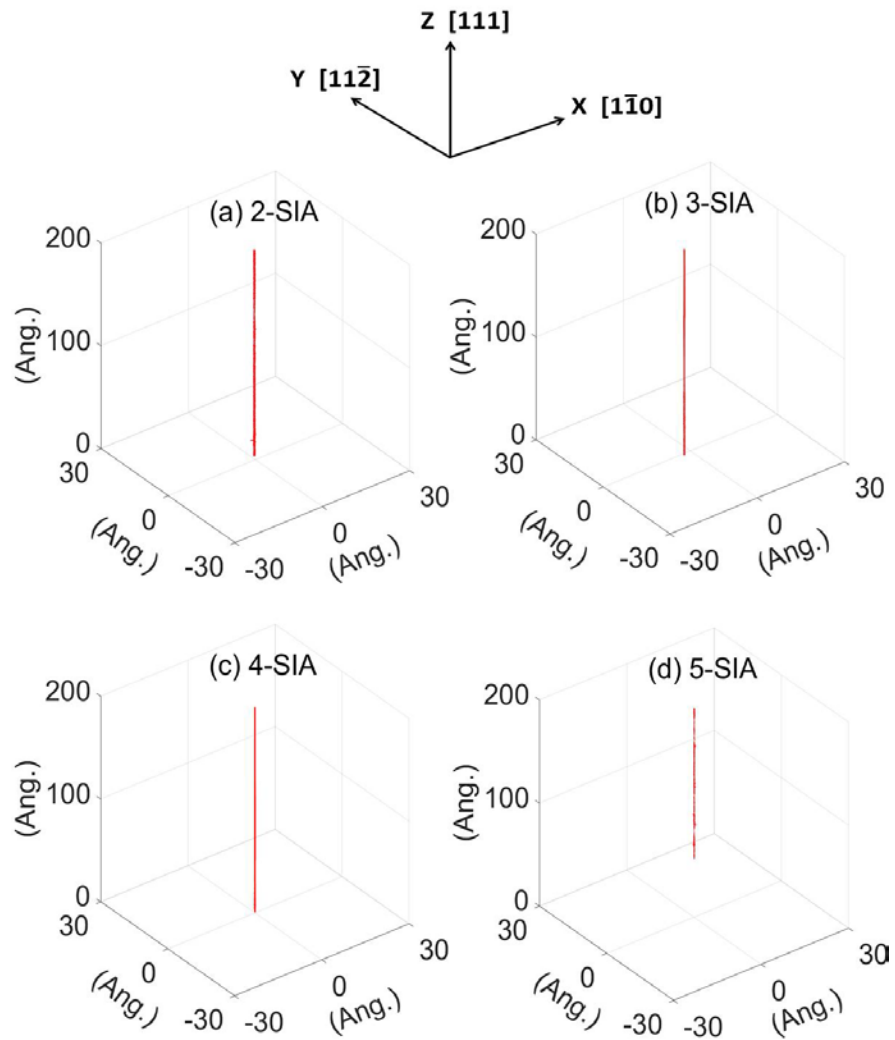


Fig. 3.6 Migration trajectories of (a) 2-SIA, (b) 3-SIA, (c) 4-SIA, and (d) 5-SIA under 3% strain at 500 K.

Adding tensile strain promotes 1D migration, and the likelihood to end 1D migration through transition of  $\langle 111 \rangle$  to  $\langle 110 \rangle$  configurations is significantly reduced. Under high strains (3%), no such configuration changes are observed. Figs. 3.6(a-d) plot the diffusion trajectories of 2-SIA to 5-SIA under 3% strain. The x, y, z axes correspond to directions of  $[1\bar{1}0]$ ,  $[11\bar{2}]$ , and  $[111]$ , respectively. Regardless of cluster sizes, all

diffusion trajectories are featured by single straight-lines along [111] axis. The migration direction is matched to the strain direction and it shows fully 1D under 3% strain along [111]. Again like 1-SIA, the formation energy differences between  $\langle 111 \rangle$  and  $\langle 110 \rangle$  of the small SIAs are reduced compared to that of unstrained crystals (0%). Even, the  $\langle 111 \rangle$  for small SIAs have the lowest formation energy depending on strains as shown in Fig. 3.1b to 3.1e. Plus, under 3% strains, all defects are aligned parallel to the strain direction [111]. Thus, the small SIAs show 1D fast diffusion to the applied strain direction. These migration behaviors under high [111] strain are similar to large SIAs (sizes more than 7) under zero strain. The fast 1D migration and its relative low migration energies for large SIAs have been observed in previous works [45, 46, 52, 55, 59, 70].

Figure 3.7(a-e) summarizes the diffusivities extracted from defect clusters of different sizes, from 1-SIA to 5-SIA, and under different strains, from 0% to 3%. The effects of strain on mobilities are significant, particularly for small clusters. As shown in Fig. 3.7a, for 1 SIA, diffusivities increase with increasing strain. At 350K (corresponding to  $1/kT=33.17 \text{ eV}^{-1}$ ), 3% strain enhances the diffusivity by more than two orders of magnitudes. The enhancements are less at higher temperatures. The temperature dependence shows an Arrhenius relation for a thermally activated process. The “apparent” activation energies are the largest for 0% strain, and are reduced with increasing strain, as reflected by slope changes of lines. We use “apparent” to emphasize that even diffusivities follow an Arrhenius expression governed by seemingly a single activation energy, the diffusion mechanisms behind can be a mixture of many different

mechanisms. At 0% and 1% strain, 1-SIA defect diffuse dominantly through 3D mechanism B. At 2-3% strain, it diffuses through a mixture of mechanism A and B as shown in Figure 3.3. These diffusion differences are supported by strain-induced formation energy changes (as shown in Fig. 3.1) and are the fundamental causes of diffusivity changes in both their magnitudes and activation energies.

For defect clusters larger than 1-SIA, the strain-induced diffusivity enhancements are relatively less. Introducing small amount of strain quickly enhances diffusivity to a level comparable to that under large strain. A higher strain results in a higher diffusivity, but the enhancement is less. Hence, the effect of strain is quickly saturated. Diffusivities at the highest strain of 3% are comparable among different cluster sizes. Fundamentally this is due to the fact that relative diffusion contributions of gliding with less migration energies are already significant for larger clusters under 0% strain (as evidenced by 3D to 1D diffusion transition shown in Fig. 3.3). Under strain, 1D diffusion is further promoted but its additional contribution to diffusivity enhancement is limited for large defect clusters. For the largest 5-SIA defect cluster, diffusivities under strain are very close to that without strain, since adding small amount of strain quickly lets  $\langle 111 \rangle$  configuration become energetically favorable and diffusion is exclusively governed by 1D migration.

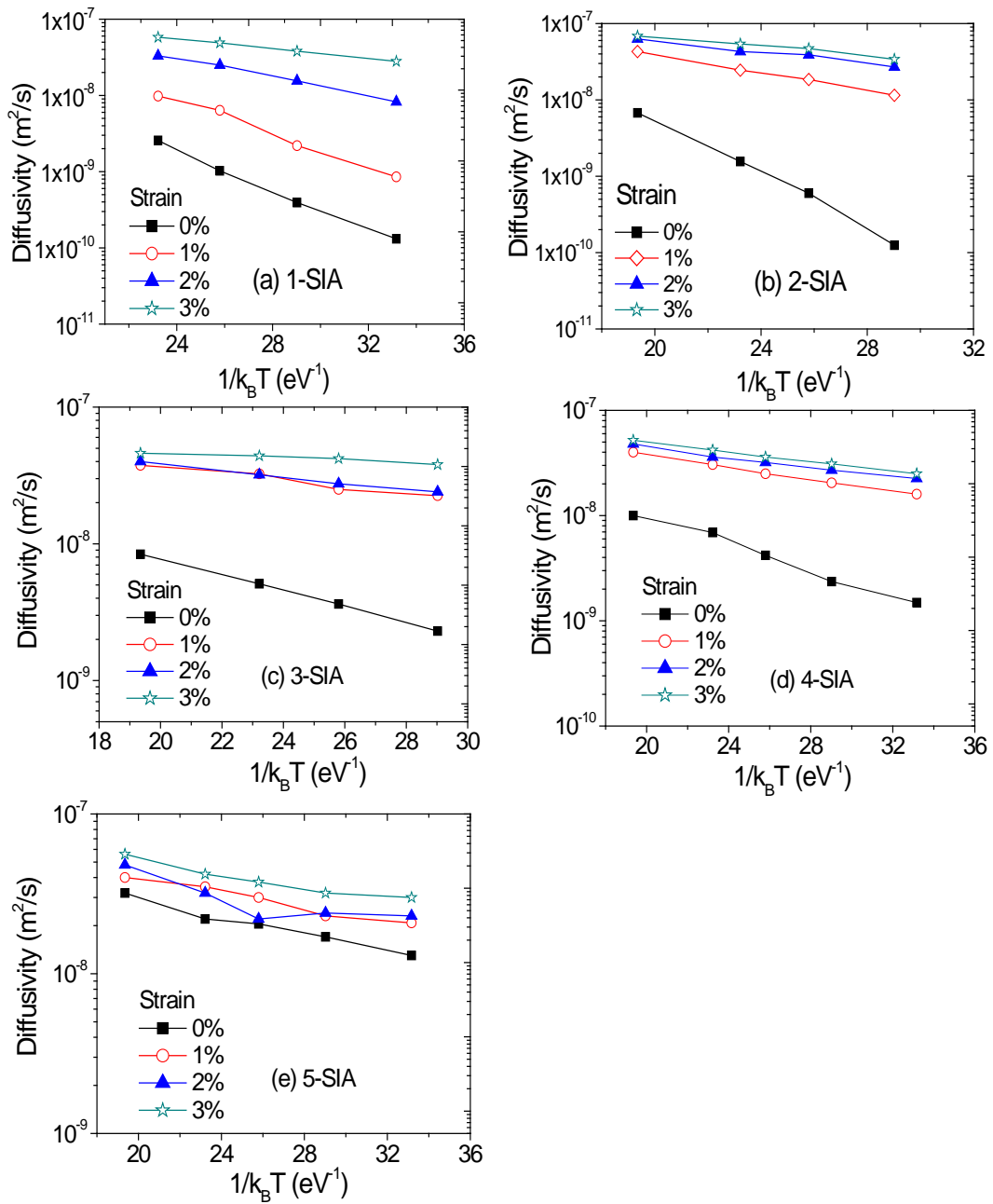


Fig. 3.7 Diffusion coefficients as a function of temperature under different tensile strain along  $\langle 111 \rangle$  direction for defect clusters containing (a) 1-SIA, (b) 2-SIAs, (c) 3-SIAs, (d) 4-SIAs, and (e) 5-SIAs.

Table 3.4 Migration energies and diffusivity prefactors of SIAs defects.

Defect size	$D_0$ ( $\times 10^{-8}$ m <sup>2</sup> /s) and $E_m$ (eV) at different tensile strains							
	0%		1%		2%		3%	
	$D_0$	$E_m$	$D_0$	$E_m$	$D_0$	$E_m$	$D_0$	$E_m$
1	230	0.30 ± 0.003	383	0.23 ± 0.005	91	0.14 ± 0.001	33	0.07 ± 0.001
2	1970	0.41 ± 0.008	58	0.14 ± 0.003	32	0.08 ± 0.002	28	0.07 ± 0.001
3	11	0.13 ± 0.003	11	0.06 ± 0.002	11	0.05 ± 0.001	11	0.05 ± 0.001
4	17	0.14 ± 0.004	14	0.07 ± 0.001	13	0.05 ± 0.002	12	0.05 ± 0.003
5	9	0.06 ± 0.002	9	0.05 ± 0.002	11	0.05 ± 0.002	8	0.04 ± 0.001

Table 3.4 summarized the extracted migration energies and diffusivity prefactors of SIA defect clusters under different strains. Regardless of strain levels, migration energies of defect clusters in general become smaller with increasing cluster sizes. Under zero strain, diffusion energies change from 0.3 eV for 1-SIA defect to 0.06 eV for 5-SIA defect. Under 3% tensile strain, the energies change from 0.07 eV for 1-SIA defect to 0.04 eV for 5-SIA defect. For the defects of the same size, increasing strain reduces migration energies. But the energy reduction is less for large defect clusters. For example, for 1-SIA defect, migration energy changes from 0.3 eV under zero strain to 0.07 eV under 3% strain. In a comparison, the changes are 0.06 eV to 0.04 eV for 5-SIA defect. For the diffusivity prefactor, it abruptly increases for 2-SIA under strain-free (0%) condition. Similar trend has been reported in previous studies [45, 46]. The primary reason is the involvement of sessile configurations which are relatively immobile than other defect types.

It is worthy to point out that the present study has certain limits. Firstly, although the EAM potential used were able to reproduce qualitatively the DFT results, it may underestimate the formation energy difference between  $\langle 110 \rangle$  and  $\langle 111 \rangle$ , which may impact on the diffusion properties predicted. Secondly, the present study is limited to strain effect along  $[111]$  only, since this direction is most effective to influence the stability difference between  $\langle 110 \rangle$  and  $\langle 111 \rangle$  SIA configurations [8]. Studies on diffusion behaviors under an arbitrary strain direction is beyond the scope of the present study. The effect of other strains could be very different.

The studies are important for multiscale modeling. Particularly for object kinetic Monte Carlo simulations which treat defect clusters as point-like defects. Both diffusivity enhancement and migration energy reduction for large defect clusters suggest that SIA clusters play an important role in defect clustering process, including agglomeration of small defects to larger ones, recombination of interstitial-type and vacancy-type defect clusters, and defect migration towards defect sinks such as grain boundaries. The dimensionality of SIAs' migration is important to defect clustering process [46]. This anisotropic diffusion causes big differences in microstructural evolution. Thus, the present study provides necessary fundamental understanding towards multiscale modeling.

### 3.4 Conclusion

We investigate the formation and migration energies of 1-SIA and SIA defect cluster under uniaxial [111] strain. Regardless of cluster sizes, both  $\langle 111 \rangle$  and  $\langle 110 \rangle$  oriented defects have reduced formation energies as a function of strain. Furthermore,  $\langle 111 \rangle$  configuration is more sensitive to strain and its defect formation energies are reduced more significantly. For all defect cluster sizes, there are switching of stable configurations from  $\langle 110 \rangle$  SIA to  $\langle 111 \rangle$  SIA. The strain also reduces the energy barrier for  $\langle 110 \rangle$  SIA(s) to rotate into  $\langle 111 \rangle$  SIA, which makes 1D migration along [111] more feasible. For 1-SIA, the migration dimension is 3D under zero strain, but change from 3D to 1D gradually with increasing strain. For SIA clusters, even under zero strain, their diffusion exhibit gradual transition from 3D to 1D at large sizes. By applying [111] tensile stress such transition starts at smaller defect sizes.

CHAPTER IV  
INDENTATION INDUCED FAST ONE DIMENSIONAL MIGRATION OF  
VACANCY CLUSTERS IN ALPHA IRON

#### 4.1 Introduction

In defective metals such as those used in nuclear reactors, extended defects resulting from irradiation damage in general causes hardening phenomena. Classic theory of plasticity explains the mechanisms due to enhanced friction of dislocation migration. Voids, loops and networking dislocations act as barriers to block dislocation migration, leading to higher yield strengths. Such hardening is accompanied with reduced ductility and reduced critical stress for cracking, and represents one major property degradation detrimental to lifetimes of reactor core components. Atomic scale modeling has been used to reveal mechanisms of metal plasticity under various conditions. Although the interplay of strain rate, stress, temperatures and crystal structures play roles in plasticity behaviors, the most recent study shows the significance of defects seeded prior to compression tests [77]. For defect free metals, twinning propagation and twin growth is the mechanism of plasticity flow and yielding; for dislocation-seeded metals, dislocation multiplication and migration are the mechanism; for void-contained metals, dislocation nucleation at voids, following by twinning, represents the yielding mechanism [77].

For radiation material science essential to nuclear engineering, effect of preexisting voids on plasticity of Fe-based steels is one key question due to void

swelling under high damage levels. In previous multiscale modeling of defect evolution, mono-vacancies and small vacancy clusters of sizes less than 5 were treated as mobile defects. Large voids of spherical shapes were reported to be stable defect configurations with low formation energies [39, 78], and were often assumed to be immobile [39, 57, 71, 79]. Recent study has shown that both migration mode (3D vs. 1D) and migration kinetics of interstitial clusters change under stress, which points to the question whether the assumption of immobile voids is still valid under stress conditions. If voids are immobile, plasticity is governed by dislocation interactions with immobile voids. However, as to be shown in the present study, small voids become mobile and evolve into dislocation loops of high diffusivities under stress, making the phenomena more complex than the current understanding.

## 4.2 Methodology

Experiment for indentation provides accurate assessment for phase transformation, shear instability, indentation energy, the elastic modulus and nucleation of dislocation through the load-displacement data [80]. Otherwise, MD simulations for nano-indentation also have been accepted well to investigate stress-strain responses with different environments. The “Large-scale atomic/molecular massively parallel simulator” (LAMMPS) is used to examine the vacancy cluster movement and the nucleation of dislocation with different size of a void [26]. The substrate interactions are described by the Mendelev potential [43]. The potential is many-body potentials of the embedded-atom-model (EAM) type. The potential has been used and concluded that

Mendelyv-type potentials are best to investigate the defect properties under different environments and nanoindentation [81-85].

Figure 4.1 shows a schematic representation of the MD simulation system. It illustrates the indenter and the substrate crystal. Periodic boundary conditions are used for X and Y directions. The X, Y, Z direction indicate [1-10], [11-2], and [111], respectively. The top surface of Z direction is non-periodic boundary condition. Two atom layers at the bottom are fixed in order to suppress any rigid-body movement of the substrate. The next four layers at the bottom, as well as the outermost four layers of the substrate in lateral directions are kept at a fixed temperature (0K). The central region of atoms are directly interacted with indenter and the system is allowed to follow NVE ensemble, while the thin layered atoms is applied NVT ensemble to dissipate the heat in the finite simulation volume. This method is similar to the previous works [86]. The indenter is assumed as infinitely rigid body. The nano-indenter is executed at speed of 2 m/s. To make uniform stress field, plane shape of indenter is applied to the surface of atoms. Atomic local strains (von Mises strains) are calculated to investigate the applied strain with depth of the indenter.

Our simulation consists of two parts: (1) Nano-indentation tests: The indenter is pushed to the substrate in Z-direction. We investigate the nucleation of dislocation and shape, mobility of vacancy clusters with increased stress. (2) Diffusion of small vacancy cluster under strains: Constant strains from 0 to 3% are applied to Z-direction. The small size vacancy clusters can be generated from irradiation directly as well as emission from large vacancy clusters. We examine the detail diffusivities and shapes of the small size

vacancy clusters. In order to identify the lattice dislocations and to determine their Burgers vector, the Dislocation Extraction Algorithm (DXA) is used. It is based on the Common Neighbor Analysis (CNA) method [87]. For visualization of the atomistic configurations we use the Open Visualization Tool OVITO [24].

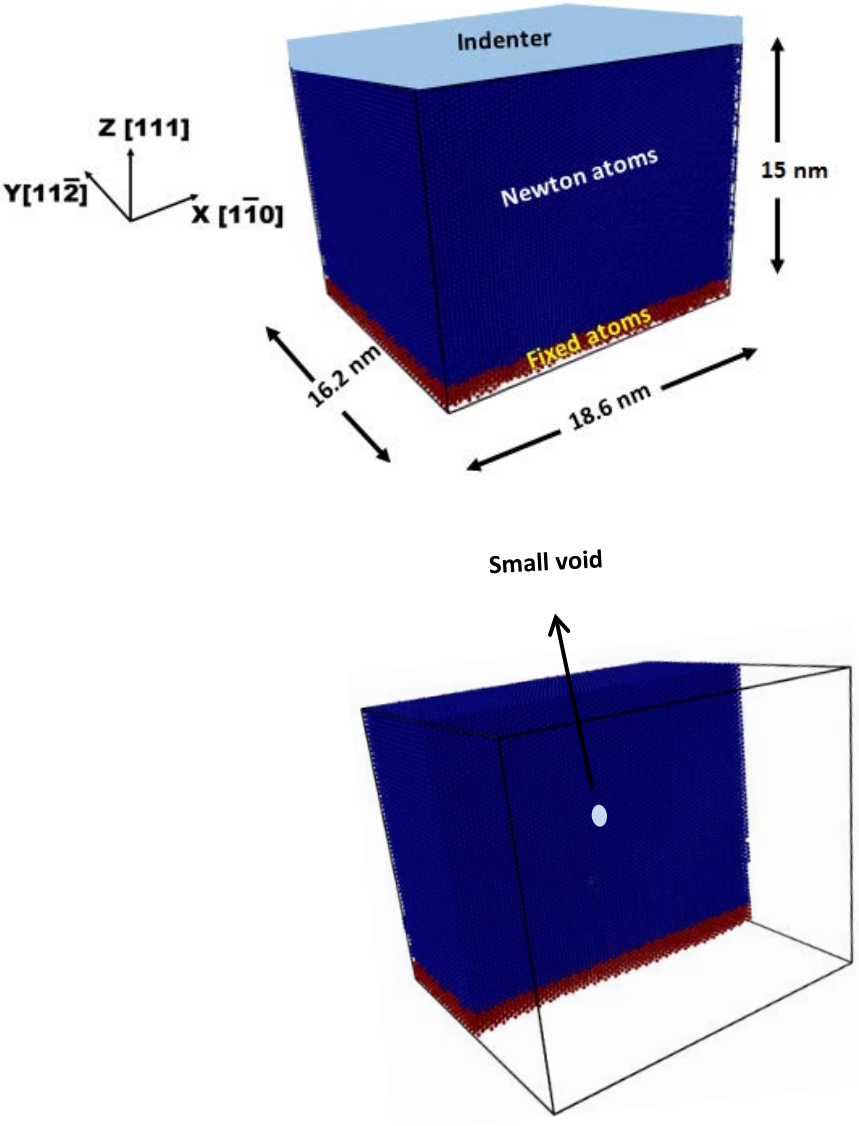


Fig. 4.1 Schematic diagram of the nanoindentation simulation model.

### 4.3 Result and discussion

Nanosized voids under compression cause plastic deformation by emitting prismatic or shear dislocation loops [88, 89]. By emitting dislocation loops, voids are collapsed [90-93]. Present work investigates the effect of stress of vacancy clusters sizes less than nanometer and a nanoscale single void.

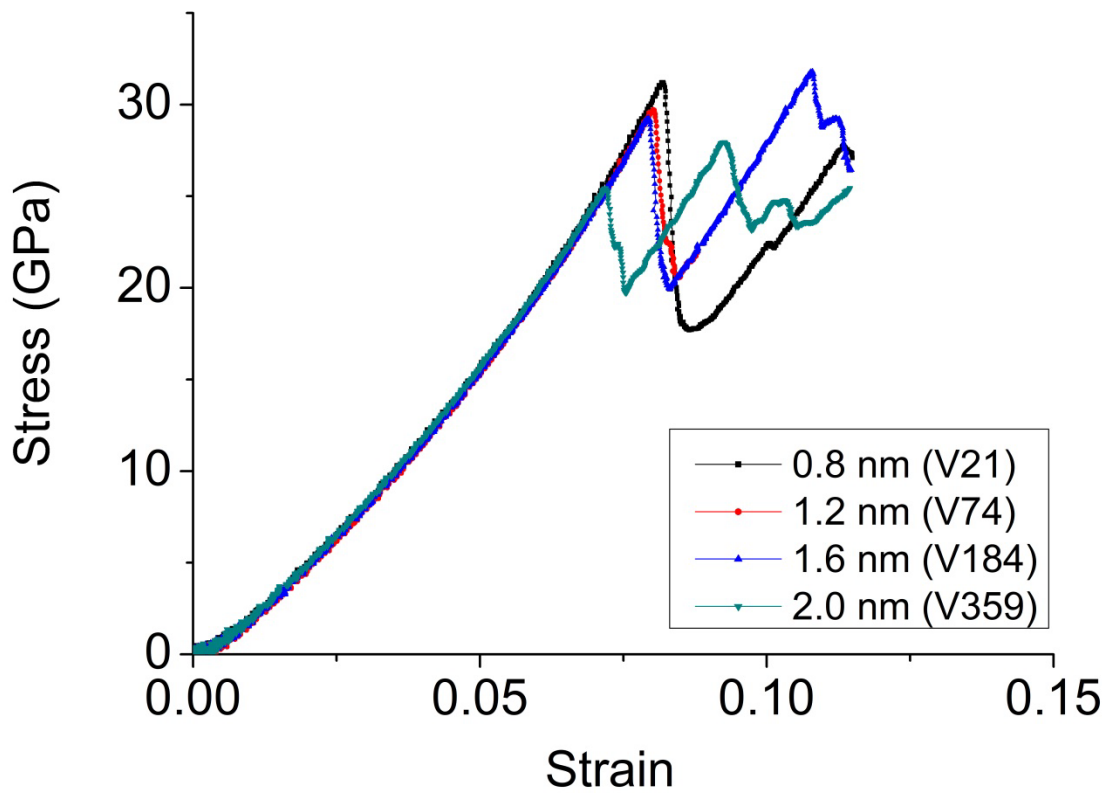


Fig. 4.2 The stress-strain curve for different size of voids.

Figure 4.2 shows stress-strain curves for bcc Fe containing a single void of different sizes, ranging from 0.8 to 2.0 nm. For the smallest void (0.8 nm), the upper

yield stress is the highest and lower yield stress is the lowest. For voids of 1.2 nm and 1.6 nm, upper yield stresses are roughly the same and both are close to 0.8 nm case, while lower yield stresses are slightly higher than the 0.8 nm case. For the largest void size of 2.0 nm, the lower yield stress is close to the cases of 1.2 nm and 1.6 nm, but the high yield stress is noticeably lower. Consistently, the upper yield stresses decrease with increasing void sizes, changing from 31.2 GPa for the smallest void of 0.8 nm to 25 GPa for the largest void of 2.0 nm. The strains at which plastic deformation occurs decrease with increasing void sizes. The changes are slight for large voids (changing from 25.44 GPa to 19.72 GPa for voids of 2.0 nm) and substantial for smallest void (abruptly from 31.2 GPa to 17.88 GPa for a void of 0.8 nm).

The stress decreases sharply after the yield stress, which means a plastic deformation of the material. After the yield stress, many dislocations are created, which increases material strength. Interestingly, the small size voids shows fast 1D migration after the stresses on surface of void increase slightly less than the yield stress as shown in figure 4.3. The movement will be discussed later.

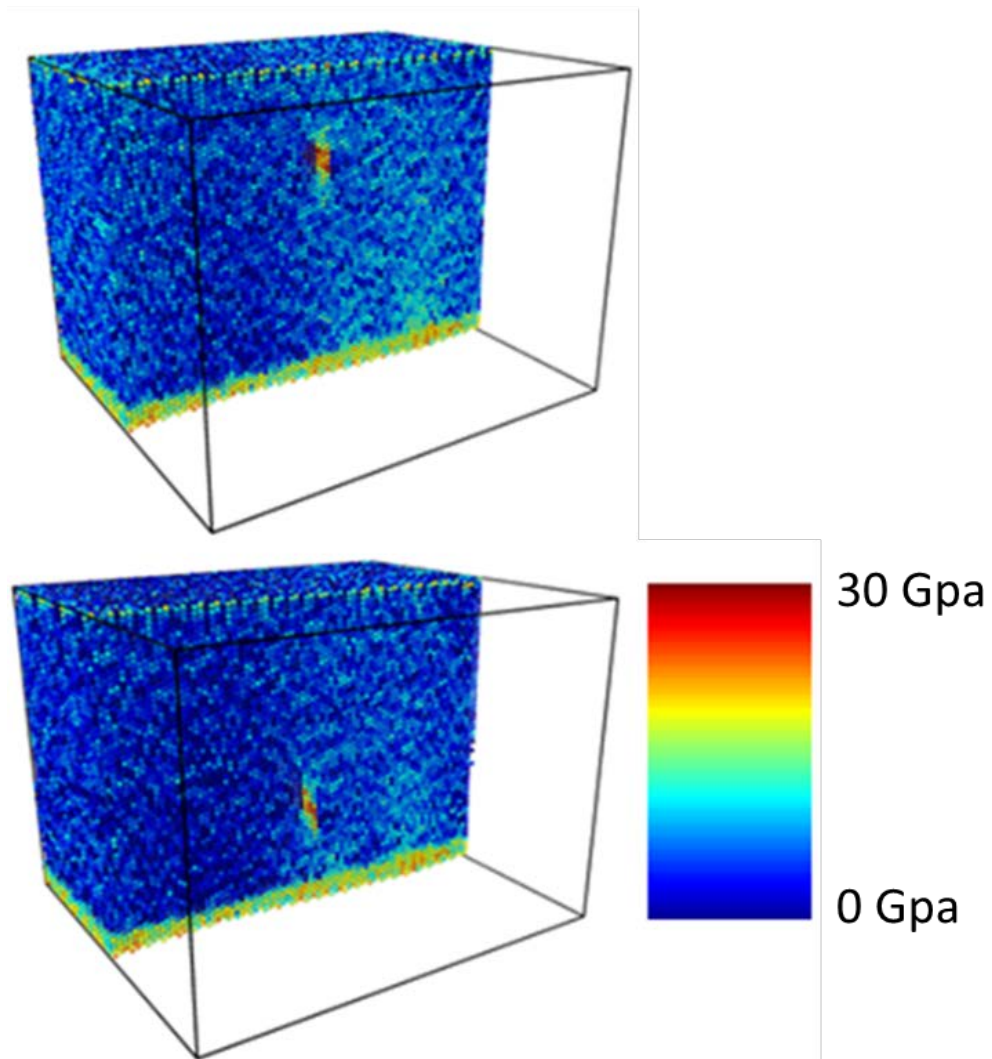


Fig. 4.3 The stress( $zz$ ) for the material with a small void (0.8 nm).

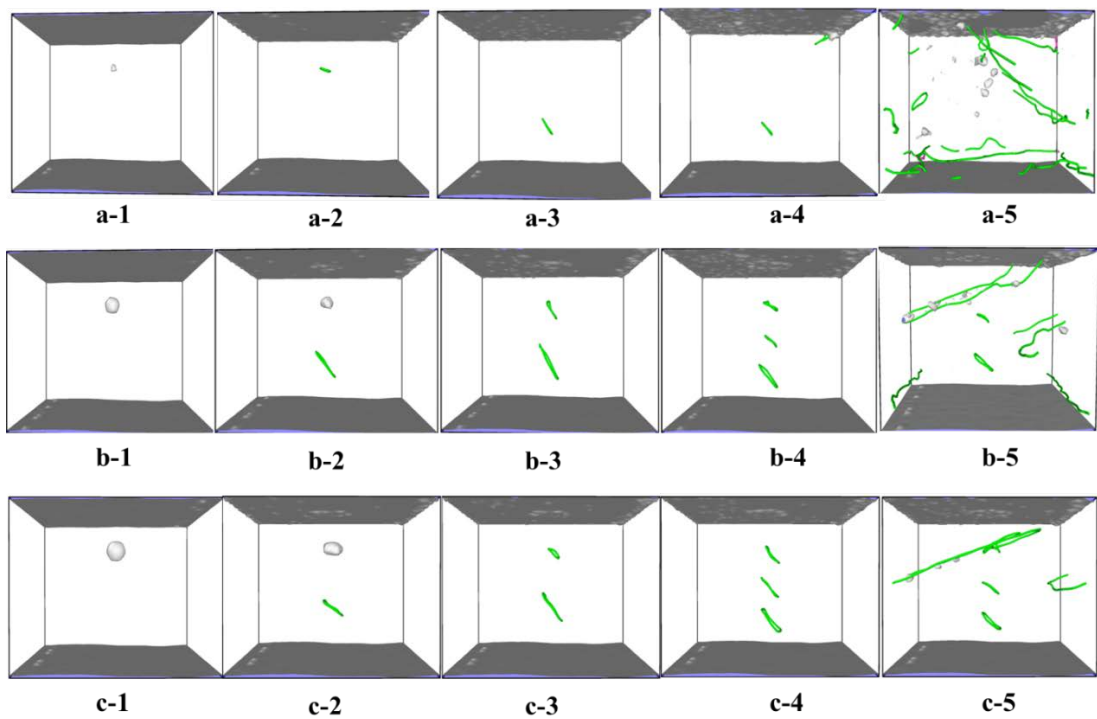


Fig. 4.4 The snapshots of different size voids for 0.8 nm (a 1 to 5), for 1.6 nm (b 1 to 5), and for 2.0 nm (c 1 to 5), showing the collapse of a void and migration under increased compressive stress.

Voids of all sizes are found to evolve into dislocation loops under indentation. Furthermore, their detail structural changes are different for void sizes. Figure 4.4 shows snapshots of the cell containing the voids of 0.8 nm (a-1 to 5), 1.6 nm (b-1 to 5), and 2.0 nm (c-1 to 5), respectively. All voids are located at 4 nm beneath the top surface. In all cases, we observe transition of spherical voids to planar vacancy dislocation loops, following by subsequent one-dimensional loop migration. The stress required for such transition depends on voids sizes: the larger the voids, the lower the stress. The critical stress varies with voids sizes from 20 to 28 GPa, but all are lower than the upper yield stress observed in indentation stress-strain curves of Figure 4.2.

For the smallest void size of 0.8 nm, it is collapsed to a vacancy dislocation loop characterized by a burgers vector of  $\frac{1}{2}$  [111], which is the same as the force loading direction (Fig. 4.4 a-2). The vacancy dislocation loop moves along the [111] with 1D (Fig. 4.4 a-3 and a-4). The migration is not necessary to be the direction which is away from the indenter. The dislocation loop movement is not a mechanism for plasticity flow away from the indented region. With increasing stress, dislocations are created at the cell surface and at the region immediately beneath the indenter. The surface dislocation creation represents the start of yielding (Fig. 4.4 a-5).

For the void size of 1.6 nm, instead of direct transition to a dislocation, the void emits a vacancy dislocation and reduces its size (Fig. 4.4 b-2). The emitted dislocation loop moves along the burgers vector direction of  $\frac{1}{2}$  [111]. At a higher stress, the shrunk void changes to the second dislocation loop of the same burgers vector (Fig. 4.4 b-3). At an even higher stress, the third dislocation loop is created through the dissociation of the

first loop. All three loops have 1D migration along [111] direction. Similar to the case of small void (0.8 nm), yield stress corresponds to the creation of high density dislocations on the surface (Fig. 4.4 b-4). Both void to loop transition and the dissociation of loop do not contribute to yielding.

For the void size of 2.0 nm, void-to-dislocation loop transition is similar. Void first emits a dislocation and later evolves into another dislocation itself. However, different from other two cases, at a high stress dislocations are created from the void, instead of the surface. The upper yield stress point corresponds to the moment that dislocations are created from the dislocation loop (the shallowest loop from the surface as shown in Fig. 4.4 c-5 ). Since such loop-induced plastic deformation occurs at relatively lower stress, the corresponding upper yield stress is the lowest among all three void sizes, as shown in Figure 4.2.

The stress-strain response and the mechanisms for plastic deformation depend on the situations like loading direction, speed, void size and etc [80, 83, 85, 86, 94, 95]]. If the size of void is larger than a few nanometer (in the case of present study set up for indenter and material), the plastic deformation occurs at the surface of void by emitting many dislocation loops from the void surface [96, 97]. The result shows the small spherical clusters change its structure and mode of mobility under stress environment. We confirm that the main differences in migration of vacancy clusters between under strain-free and compressive strain along [111] are diffusivity, direction of movement, its configuration during movement, and migration energy.

In order to investigate the stress effects on void diffusion and structural evolution, different stresses are applied to maintain a constant uniaxial compressive strain (up to 3%) along [111] direction. Furthermore, the cell is kept at 750 K in order to accelerate structural changes. Mean square displacements (MSD) of center of mass (COM) of voids are analyzed to obtain diffusivities and migration energies.

We find that under zero strain, spherical vacancy clusters (up to size  $n=15$ ) rarely migrate within the time period of the present work (up to a few tens ns) and their diffusivities are ignorable. This is understandable due to the fact that void migration requires vacancy dissociation from one end and re-capture of vacancies on the other end. When strain is increased beyond a critical value, the morphologies of voids change from spherical to planar. Subsequently, the planar dislocation loop migrates easily with 1D motion. As typical examples, Figure 4.5 and 4.6 show the displacement of center of mass of  $V_{11}$  and  $V_{14}$  along  $z$  direction under 3 % compressive strain along [111], where  $x, y, z$  directions correspond to [1-10],[11-2],[111] axial directions, respectively. In Figure 4.6, the insets show cluster morphology viewed from the top (along [111] direction) and from the side (along [1-10] direction). From 0 to about 8.2 ns, the  $V_{14}$  remains spherical shape. At about 8.2 ns, the void is collapsed into a planar loop, which represents the moment to start abrupt 1D migration.

Under an uniaxial stress, a planar void has a lower formation energy than its spherical counterpart since strain relaxation along the stress direction is maximized, which gains the largest energy release upon spherical-to-planar transition. As shown in the inset of Figure 4.6 at time about 8.2 ns, the  $V_{14}$  planar void has a total of 14

vacancies as viewed from [111] direction, which means each [111] axis has only one single vacancy. On the other hand, the side view shows that the defects are not exactly like a loop since vacancies do not stay on the same closely-packed atomic plane. The planar void is quite “rough”, and is an assembly of single vacancies on different atomic planes. Four insets on the bottom of Fig. 4.6 show the side views of planar voids at times within the yellow marked time period. Upon migration, each single vacancy jumps along [111] direction. However, the diffusion is correlated due to strong bonding of vacancy to the planar voids.

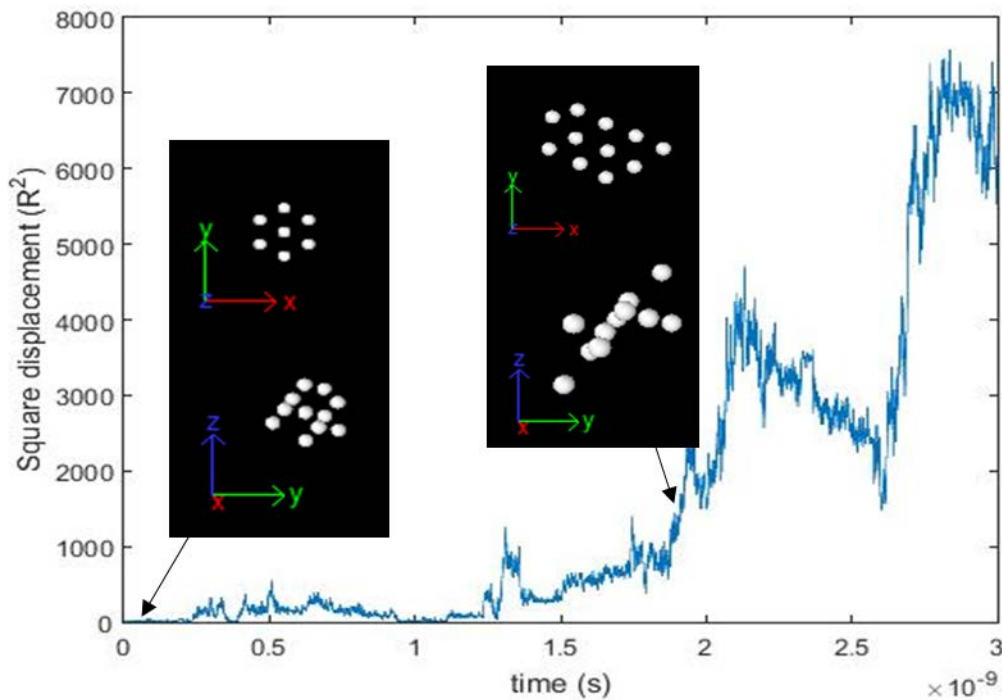


Fig. 4.5 The square displacement ( $\text{\AA}^2$ ) of vacancy clusters size 11 along [111] and the transformation of structure for migration under 3% compressive strain at 750 K.

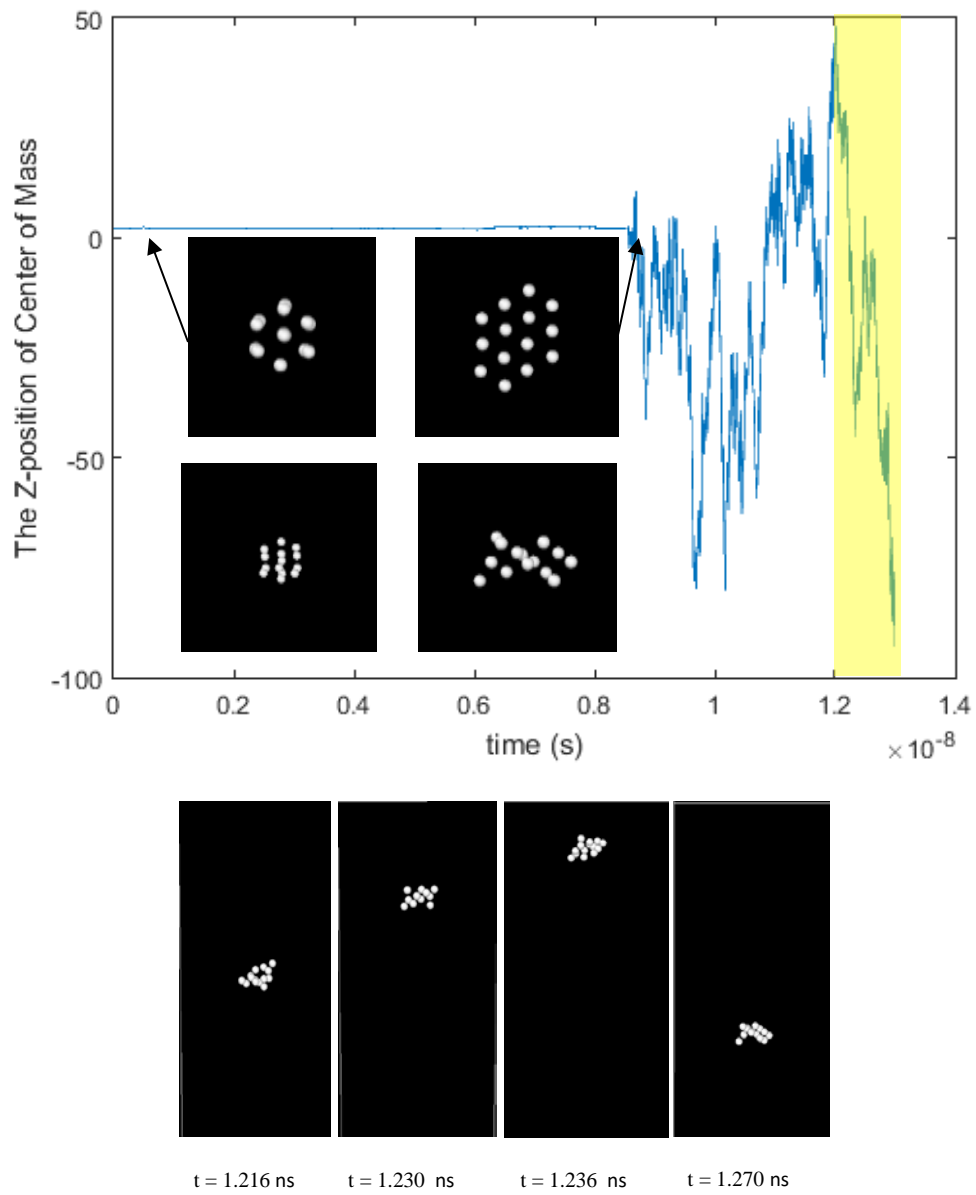


Fig. 4.6 Structures and movements of vacancy cluster with size 14 under 3% compressive strain and 750 K.

Immobility of spherical voids and quick 1D diffusion after spherical-to-planar transition are observed for all clusters up to size of 15 (the largest size modeled). However, complexity arises for size  $n=9$ . Fig. 4.7 shows the [111] displacements of  $V_9$  under 3 % compressive strain.  $V_9$  starts its migration once it evolves into planar loops (at about 5 ns). However, different from other cluster sizes, the  $V_9$  planar loop can evolve back into spherical void, and repeat the change of configuration. It becomes immobilized at about 60 ns.

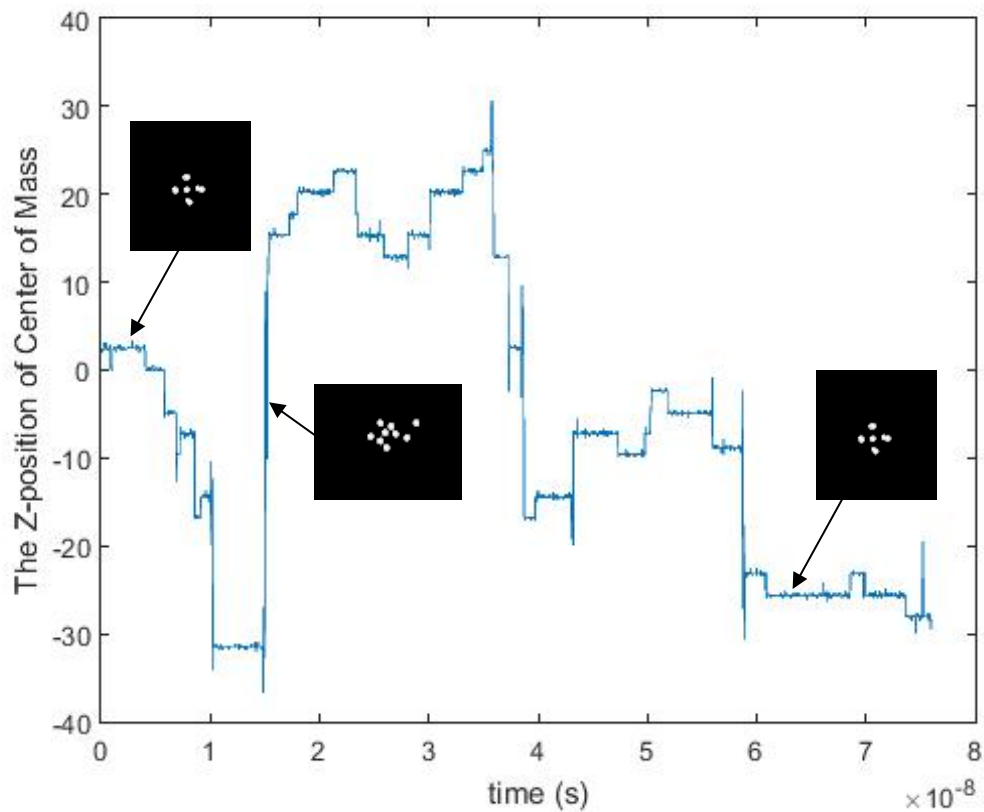


Fig. 4.7 The displacements of center of mass (COM) of vacancy cluster with size 9, and configurations under 3% strain.

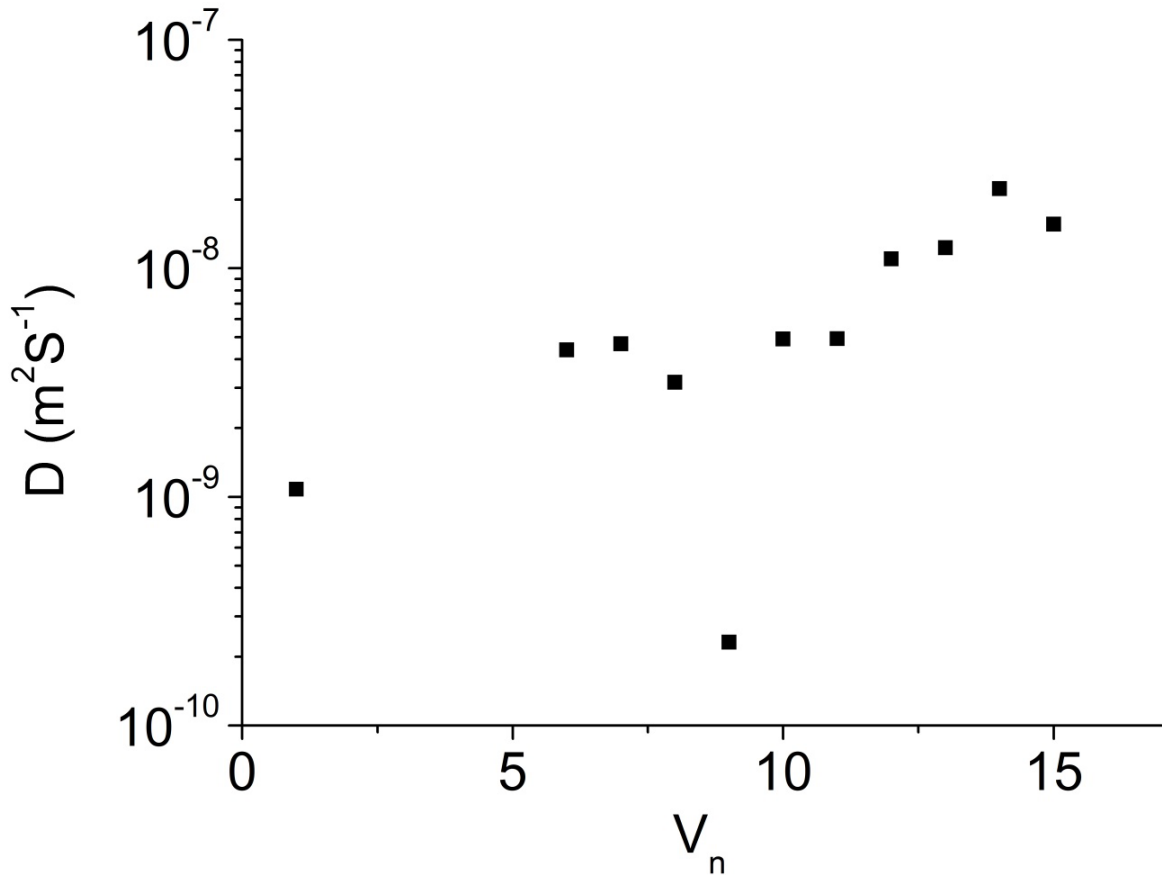


Fig. 4.8 Diffusivities of different sizes of vacancy clusters under 3% compressive strain at 750 K.

Fig. 4.8 shows size dependence of diffusivities of  $V_n$  at 750 K. With increasing sizes, diffusivities generally increase, from about  $10^{-9} \text{ m}^2 \text{ s}^{-1}$  for  $V$  to about  $10^{-8} \text{ m}^2 \text{ s}^{-1}$  for  $V_{15}$ . The size  $n=9$  is deviated from this general trend because of its easy conversion between a spherical void and a planar void. Other cluster sizes do not have such convertible transition. Fig. 5a does not include sizes from 2 to 5 since they easily become dissociated at this temperature. We investigate migration energy of small vacancy

cluster with size 11. Based on the high diffusivity of vacancy clusters under high compressive strain 3%, the migration energy barriers are expected to be small. In present work, the migration energy of 0.14 eV is measured. This low migration energy is related to the probability of the correlation in displacements of vacancy defects inside the cluster [98]. It shows similar values with the fast thermally-activated one-dimensional motion of SIA clusters, which is close to the 0.05 to 0.07 eV in MD calculations [45, 46]. In present work, the 1D glide of small vacancy loops occurs due to the strain and thermal vibration of atoms.

#### 4.4 Conclusion

The effects of compressive stress and strain on diffusivities of vacancy clusters in  $\alpha$ -Fe are investigated by Molecular Dynamics (MD). The nanoindentation is used to monitor the stress-strain response of material with different size voids. A larger size of void has a lower yield stress. The mechanism of collapse of voids with different size is also studied. The void size less than 1 nanometer changes to a vacancy dislocation loop with burgers vector of  $\frac{1}{2}[111]$ , which is the same with loading direction. The vacancy dislocation loop shows fast 1D movement along the  $[111]$ . With this small size of void, the plastic deformation occurs at the surface of material facing with the indenter. However, the void, size of 2.00 nm, emits vacancy dislocation loops and the plastic deformation occurs at the surface of a void or a vacancy dislocation loop. We also investigate diffusivities and migration energy of small vacancy clusters under constant compressive strains along  $[111]$ . At strain-free (0%) and high temperature (750 K), the

spherical vacancy clusters are immobile and displacements of the center of mass (COM) of vacancy clusters can be ignored within the present MD simulation time. However, the migration path shows fully one dimension (1D) under the 3% strain rate along the [111] direction with high diffusivities. A transformation from spherical structure to planar one under the strains is required to have the fast one dimensional migration. The diffusivities of small vacancy clusters are several orders of magnitude higher than that of the single vacancy at the same temperature ( $T=750$  K) and same strain rate (3 %). These results indicate that the damage accumulation will be different significantly between strain-free and strain environment due to the different mobility and migration mode of vacancy clusters, which shows fast one-dimensional movement along the direction of compressive strain.

The present study is important to understand both defect evolution and mechanical property changes of steels in harsh irradiation environments. In fast reactors, neutron damage causes void swelling in fuel cladding and dimensional changes of fuel. Once the gap between fuel and cladding is closed up, the mechanical interaction leads to compressive stress on fuel cladding. Void evolution and migration under stress, dislocation creation, and plasticity flow are all key phenomena to be included in multiscale modeling to predict materials behaviors. The information and properties can be used in the multiscale modeling of damages under strain environment. This work is also important to show and support that vacancy clusters with planar structure can be migrated to one dimensional with high diffusivity. The high diffusivity can be one of

reasons for increased void swelling under stresses since the vacancy clusters would diffuse more and coalesce more to create voids.

## CHAPTER V

### CONCLUSION AND FUTURE WORK

MD simulations are used to investigate the effect of strain. Firstly, we measured the damage production of pure iron ( $\alpha$ -Fe) under different strain environment. We found that the changes in the number of defects, cluster sizes and numbers are significant under strains along [111]. The volume changes due to the applied strains lead to the change of displacement threshold energy and formation energy. Those are directly related to the peak number of defect on the evolution of displacement cascade. On the other hands, present work examined the importance of anisotropic diffusion for initial defect generation. 2% isometric volume conserving strain along [111] causes 50% increase in the number of defects. We also investigated the peak number, the peak time, the ratio of the number of surviving defects to the peak number defects, and recombination rate under different strain conditions along [111]. The combination effects of the anisotropy diffusions and different migration energies under strains might be possible reasons for different recombination rates on the recombination stage of defect evolution. This result can be useful to understand the effect of strains on displacement cascade stage and the initial stage of annealing in MD scale.

Secondly, we investigated the formation and migration energies of 1-SIA and SIA defect cluster in  $\alpha$ -Fe under uniaxial [111] strain. Regardless of cluster sizes, both  $\langle 111 \rangle$  and  $\langle 110 \rangle$  oriented defects have reduced formation energies as strain increases. Furthermore,  $\langle 111 \rangle$  configuration is more sensitive to strain. The formation energies of

$\langle 111 \rangle$  defects are reduced more significantly. For all defect cluster sizes, there are switching of stable configurations from  $\langle 110 \rangle$  SIA to  $\langle 111 \rangle$  SIA. The strain also reduces the energy barrier for  $\langle 110 \rangle$  SIA(s) to rotate into  $\langle 111 \rangle$  SIA, which makes 1D migration along [111] more feasible. For 1-SIA, the migration dimension changes from 3D to 1D gradually with increasing strain. For SIA clusters, even under zero strain, their diffusion exhibit gradual transition from 3D to 1D at large sizes. Under [111] tensile stress, such transitions are shown at smaller defect sizes.

Thirdly, the effects of compressive stress and strain on diffusivities of vacancy clusters in  $\alpha$ -Fe are investigated. The nanoindentation is used to examine the stress-strain response of material with different size voids. We also observed that a larger size of void has a lower yield stress. The mechanism of collapse of voids with different size is also discussed. The void size less than 1 nanometer changes to a vacancy dislocation loop with burgers vector of  $\frac{1}{2}[111]$ , which is the same with applied strain direction. The vacancy dislocation loop showed fast 1D movement along the [111]. We also investigated diffusivities and migration energy of small vacancy clusters under constant compressive strains along [111]. At strain-free (0%) and high temperature (750 K), the spherical vacancy clusters are immobile and displacements of the center of mass (COM) of vacancy clusters can be ignored within the present MD simulation time. However, the migration path showed fully one dimension (1D) under the 3% strain rate along the [111] direction with high diffusivities through thermally activated process. The diffusivities of small vacancy clusters are several orders of magnitude higher than that of the single vacancy at the same temperature ( $T=750$  K) and same strain rate (3 %). The

clusters under strain free and strains showed different mobility and migration modes. These results showed that the damage accumulation would be different significantly between strain-free and strain environment. The present work can be used to develop the multiscale calculation of damages under strain environment. This work is also important to show and support that vacancy clusters with planar structure can be migrated to one dimensional with high diffusivity. The high diffusivity can be one of reasons for increased void swelling under stresses since the vacancy clusters would diffuse more and coalesce more to create voids.

Present work investigated the defect production, formation and migration energies of defects, and the response of small vacancy clusters under different strains by using molecular dynamics. Thus, the results are only valid in limited time and length scales, covered by MD works. In order to investigate long time and length scales, we suggest one of the possible experiment methods. For the research of microevolution of damage under stress condition, heavy ion accelerator systems in Dr. Shao's LAB can be used. By injecting 3.5 MeV  $\text{Fe}^{2+}$  ions on the pure Iron in 1.7 MV accelerator system, the neutron damage of reactor system can be simulated. A miniature-sized stress test machine of 3 point bending can be one of the options to apply strains to the sample as shown in figure 5.1. The sample would have compressive and tensile strains regions. After bending the sample, the deflection of the sample can be measured by using Scanning Electron Microscope (SEM). The stress field on the side of the sample also can be calculated by computational methods. After irradiation, hardness and void swelling can be investigated to see the effects of stress. For hardness test, a nanomechanical test

instrument can be used. For void swelling study, Focused Ion Beam (FIB) and Transmission Electron Microscopy (TEM) can be useful instruments. The experiments will be studied continuously to see the strain effects on hardness and void swelling.



Fig. 5.1 A possible miniature-sized stress test machine for 3-point bending.

## REFERENCES

- [1] G.S. Was, *Fundamentals of Radiation Materials Science: Metals and Alloys*, Springer 2007.
- [2] B.D. Wirth, *Development of Multiscale Materials Modeling Techniques and Coarse-Graining Strategies for Predicting Materials Degradation in Extreme Irradiation Environments*, ; Battelle Energy Alliance, LLC, Idaho Falls, ID (United States), 2016, p. Medium: ED; Size: 43 p.
- [3] L.K. Mansur, Theory and experimental background on dimensional changes in irradiated alloys, *Journal of Nuclear Materials* 216 (1994) 97-123.
- [4] a.E.J.F. C. Cawthorne, Voids in Irradiated Stainless Steel, *Nature* 216 (1965) 575.
- [5] M. Tikhonchev, V. Svetukhin, Primary Radiation Damage of BCC Iron under Uniaxial and Hydrostatic Stress: MD Simulation, *Applied Mechanics and Materials* 835 (2016) 197-202.
- [6] S. Di, Z. Yao, M.R. Daymond, F. Gao, Molecular dynamics simulations of irradiation cascades in alpha-zirconium under macroscopic strain, *Nuclear Instruments and Methods in Physics Research Section B: Beam Interactions with Materials and Atoms* 303 (2013) 95-99.
- [7] B. Beeler, M. Asta, P. Hosemann, N. Grønbech-Jensen, Effects of applied strain on radiation damage generation in body-centered cubic iron, *Journal of Nuclear Materials* 459 (2015) 159-165.

- [8] D.J.B. F. Gao, P.E..J. Flewitt, T.A. Lewis, The influence of strain on defect generation by displacement cascades in  $\alpha$  iron, *Nuclear Instruments and Methods in Physics Research B* 180 (2001) 187-193.
- [9] B. Beeler, M. Asta, P. Hosemann, N. Grønbech-Jensen, Effect of strain and temperature on the threshold displacement energy in body-centered cubic iron, *Journal of Nuclear Materials* 474 (2016) 113-119.
- [10] D. Wang, N. Gao, Z.G. Wang, X. Gao, W.H. He, M.H. Cui, L.L. Pang, Y.B. Zhu, Effect of strain field on displacement cascade in tungsten studied by molecular dynamics simulation, *Nuclear Instruments and Methods in Physics Research Section B: Beam Interactions with Materials and Atoms* 384 (2016) 68-75.
- [11] S. Miyashiro, S. Fujita, T. Okita, MD simulations to evaluate the influence of applied normal stress or deformation on defect production rate and size distribution of clusters in cascade process for pure Cu, *Journal of Nuclear Materials* 415(1) (2011) 1-4.
- [12] J.W.M. M. Nastasi, and J. K. Hirvonen, *Ion-solid Interactions Fundamentals and Applications* Cambridge University Press, New York, 1996.
- [13] B. JA, *Amer J Phys* 24 (1956) 251.
- [14] S. A, On the theory of radiation damage and radiation hardening, In: *Proceedings of the Second United Nations International Conference on the Peaceful Uses of Atomic Energy*, United Nations, New York, 1958, p. 250.
- [15] R.E. Stoller, *Primary Radiation Damage Formation* Elsevier Ltd, Amsterdam, 2012.
- [16] R.S. Averback, Atomic displacement processes in irradiated metals, *Journal of Nuclear Materials* 216 (1994) 49-62.

- [17] B.E. Watt, Energy Spectrum of Neutrons from Thermal Fission of U235, *Physical Review* 87(6) (1952) 1037-1041.
- [18] G.H.K.a.R.S. Pease, The Displacement of Atoms in Solids by Radiation, *Rep. Prog. Phys.* 18 (1955).
- [19] M.T.R. M.J. Norgett, I.M. Torrens, A Proposed method of calculating displacement dose rates, *Nuclear Engineering and Design* 33 (1975) 50-54.
- [20] M.T. Robinson, Basic physics of radiation damage production, *Journal of Nuclear Materials* 216 (1994) 1-28.
- [21] C.H. Woo, X. Liu, Atomistic calculation of point-defect diffusion anisotropy and irradiation growth in  $\alpha$ -zirconium, *Philosophical Magazine* 87(16) (2007) 2355-2369.
- [22] M.S. Daw, M.I. Baskes, Embedded-atom method: Derivation and application to impurities, surfaces, and other defects in metals, *Physical Review B* 29(12) (1984) 6443-6453.
- [23] M.W. Finnis, J.E. Sinclair, A simple empirical N-body potential for transition metals, *Philosophical Magazine A* 50(1) (1984) 45-55.
- [24] A. Stukowski, Visualization and analysis of atomistic simulation data with OVITO—the Open Visualization Tool, *Modelling and Simulation in Materials Science and Engineering* 18(1) (2010) 015012.
- [25] J. Stadler, R. Mikulla, H.R. Trebin, IMD: A Software Package for Molecular Dynamics Studies on Parallel Computers, *International Journal of Modern Physics C* 08(05) (1997) 1131-1140.

- [26] S. Plimpton, Fast Parallel Algorithms for Short-Range Molecular Dynamics, *Journal of Computational Physics* 117 (1995) 1-19.
- [27] A.F.C. D.J. Bacon, J.M. Harder, S.J. Wooding, Computer simulation of low-energy displacement events in pure bcc and hcp metals, *Journal of Nuclear Materials* 205 (1993) 52-58.
- [28] R.E. Stoller, Point defect survival and clustering fractions obtained from molecular dynamics simulations of high energy cascades, *Journal of Nuclear Materials* 233-237 (1996) 999-1003.
- [29] G.R.O. R.E. Stoller, B.D. Wirth, Primary damage formation in bcc iron, *Journal of Nuclear Materials* 251 (1997) 49-60.
- [30] R.E. Stoller, Subcascade formation in displacement cascade simulations: Implication for fusion reactor materials, *Journal of Nuclear Materials* 271&272 (1999) 57-62.
- [31] D.J.B. F. Gao, A.F. Calder, P.E.J. Flewitt, T.A. Lewis, Computer simulation study of cascade overlap effects in  $\alpha$ -iron, *Journal of Nuclear Materials* 230 (1996) 47-56.
- [32] D.J.B. F. Gao, P.E..J. Flewitt, T.A. Lewis, A molecular dynamics study of temperature effects on defect production by displacement cascades in  $\alpha$ -iron, *Journal of Nuclear Materials* 249 (1997) 77-86.
- [33] T.D.d.l.R. David J. Bacon, Molecular dynamics computer simulations of displacement cascades in metals, *Journal of Nuclear Materials* 216 (1994) 275-290.

- [34] D.J. Bacon, Y.N. Osetsky, Multiscale modelling of radiation damage in metals: from defect generation to material properties, *Materials Science and Engineering: A* 365(1-2) (2004) 46-56.
- [35] L. Malerba, Molecular dynamics simulation of displacement cascades in  $\alpha$ -Fe: A critical review, *Journal of Nuclear Materials* 351(1-3) (2006) 28-38.
- [36] D.A. Terentyev, L. Malerba, R. Chakarova, K. Nordlund, P. Olsson, M. Rieth, J. Wallenius, Displacement cascades in Fe–Cr: A molecular dynamics study, *Journal of Nuclear Materials* 349(1-2) (2006) 119-132.
- [37] R.E.S. W.J. Phythian, A.J.E. Foreman, A.F. Calder, D.J. Bacon, A comparison of displacement cascades in copper and iron by molecular dynamics and its application to microstructural evolution, *Journal of Nuclear Materials* 223 (1995) 245-261.
- [38] N.S. M.J. Caturla, E. Alonso, B.D. Wirth, T. Diaz de la Rubia, Comparative study of radiation damage accumulation in Cu and Fe, *Journal of Nuclear Materials* 276 (2000) 13-21.
- [39] N. Soneda, T.D. de la Rubia, Defect production, annealing kinetics and damage evolution in  $\alpha$ -Fe: An atomic-scale computer simulation, *Philosophical Magazine A* 78(5) (1998) 995-1019.
- [40] S.J.Z.a.B.N. Singh, Analysis of displacement damage and defect production under cascade damage conditions, *Journal of Nuclear Materials* 199 (1993) 173-191.
- [41] G.J. Ackland, M.I. Mendeleev, D.J. Srolovitz, S. Han, A.V. Barashev, Development of an interatomic potential for phosphorus impurities in iron, *Journal of Physics: Condensed Matter* 16(27) (2004) S2629-S2642.

- [42] S. Miyashiro, S. Fujita, T. Okita, H. Okuda, MD simulations to evaluate effects of applied tensile strain on irradiation-induced defect production at various PKA energies, *Fusion Engineering and Design* 87(7-8) (2012) 1352-1355.
- [43] M.I. Mendeleev, S. Han, D.J. Srolovitz, G.J. Ackland, D.Y. Sun, M. Asta, Development of new interatomic potentials appropriate for crystalline and liquid iron, *Philosophical Magazine* 83(35) (2003) 3977-3994.
- [44] C. Kang, Q. Wang, L. Shao, Kinetics of interstitial defects in  $\alpha$ -Fe: The effect from uniaxial stress, *Journal of Nuclear Materials* 485 (2017) 159-168.
- [45] N. Anento, A. Serra, Y.N. Osetsky, Atomistic study of multimechanism diffusion by self-interstitial defects in  $\alpha$ -Fe, *Modelling and Simulation in Materials Science and Engineering* 18(2) (2010) 025008.
- [46] D.A. Terentyev, L. Malerba, M. Hou, Dimensionality of interstitial cluster motion in bcc-Fe, *Physical Review B* 75(10) (2007).
- [47] D. Wang, N. Gao, W. Setyawan, R.J. Kurtz, Z.-G. Wang, X. Gao, W.-H. He, L.-L. Pang, Effect of Strain Field on Threshold Displacement Energy of Tungsten Studied by Molecular Dynamics Simulation, *Chinese Physics Letters* 33(9) (2016) 096102.
- [48] G.W. Lewthwaite, Irradiation creep during void production, *Journal of Nuclear Materials* 46 (1973) 324-328.
- [49] G.W. Lewthwaite, Interconnection between irradiation creep and interstitial loop formation in fcc metals, *Journal of Nuclear Materials* 54 (1974) 141-142.
- [50] W.S. K. Herschbach, Interconnection between irradiation creep and interstitial loop formation in fcc metals, *Journal of Nuclear Materials* 51 (1974) 215-220.

- [51] E.R.G. J.F. Bates, Experimental evidence for stress enhanced swelling, *Journal of Nuclear Materials* 59 (1976) 95-102.
- [52] G.R.O. B.D. Wirth, D. Maroudas, G.E. Lucas, Energetics of formation and migration of self interstitials and self interstitial clusters in alpha iron, *Journal of Nuclear Materials* 244 (1997) 185-194.
- [53] Y.N. Osetsky, A. Serra, B.N. Singh, S.I. Golubov, Structure and properties of clusters of self-interstitial atoms in fcc copper and bcc iron, *Philosophical Magazine A* 80(9) (2000) 2131-2157.
- [54] Y.N. Osetsky, Atomistic Study of Diffusional Mass Transport in Metals, *Defect and Diffusion Forum* 188-190 (2001) 71-92.
- [55] J. Marian, B.D. Wirth, A. Caro, B. Sadigh, G.R. Odette, J.M. Perlado, T. Diaz de la Rubia, Dynamics of self-interstitial cluster migration in pure  $\alpha$ -Fe and Fe-Cu alloys, *Physical Review B* 65(14) (2002).
- [56] C.C. Fu, F. Willaime, P. Ordejon, Stability and mobility of mono- and di-interstitials in alpha-Fe, *Physical review letters* 92(17) (2004) 175503.
- [57] C.-C. Fu, J.D. Torre, F. Willaime, J.-L. Bocquet, A. Barbu, Multiscale modelling of defect kinetics in irradiated iron, *Nature Materials* 4(1) (2004) 68-74.
- [58] K. Kusunoki, Molecular-Dynamics Study of Self-Interstitial Diffusion in bcc-Iron, *Materials Transactions* 47(8) (2006) 1906-1909.
- [59] N. Soneda, T. Diaz de La Rubia, Migration kinetics of the self-interstitial atom and its clusters in bcc Fe, *Philosophical Magazine A* 81(2) (2001) 331-343.

- [60] W.-L. Chan, R.S. Averback, Y. Ashkenazy, Anisotropic diffusion of point defects in metals under a biaxial stress field simulation and theory, *Journal of Applied Physics* 104(2) (2008) 023502.
- [61] D.S. Tchitchekova, J. Morthomas, F. Ribeiro, R. Ducher, M. Perez, A novel method for calculating the energy barriers for carbon diffusion in ferrite under heterogeneous stress, *The Journal of chemical physics* 141(3) (2014) 034118.
- [62] Z. Chen, N. Kioussis, N. Ghoniem, D. Seif, Strain-field effects on the formation and migration energies of self interstitials in  $\alpha$ -Fe from first principles, *Physical Review B* 81(9) (2010).
- [63] X. Li, C. Gao, X.L. Xiong, Y. Bai, Y.J. Su, Hydrogen diffusion in  $\alpha$ -Fe under an applied 3-axis strain: A quantum manifestation, *International Journal of Hydrogen Energy* 40(32) (2015) 10340-10345.
- [64] B.P.U. Graeme Henkelman, Hannes Jonsson, A climbing image nudged elastic band method for finding saddle points and minimum energy paths, *Journal of chemical physics* 113 (2000) 9901-9904.
- [65] H.J. Graeme Henkelman, Improved tangent estimate in the nudged elastic band method for finding minimum energy paths and saddle points, *Journal of chemical physics* 113 (2000) 9978-9985.
- [66] A. Nakano, A space-time-ensemble parallel nudged elastic band algorithm for molecular kinetics simulation, *Computer Physics Communications* 178(4) (2008) 280-289.

- [67] M.W. Guinan, R.N. Stuart, R.J. Borg, Fully dynamic computer simulation of self-interstitial diffusion in tungsten, *Physical Review B* 15(2) (1977) 699-710.
- [68] G.R.O. B.D. Wirth, D. Maroudas, G.E. Lucas, Dislocation loop structure, energy and mobility of self-interstitial atom clusters in bcc iron, *Journal of Nuclear Materials* 276 (2000) 33-40.
- [69] M.V. Yu.N. Osetsky, A. Serra, S.I. Golubov, V. Priego, Computer simulation of vacancy and interstitial clusters in bcc and fcc metals, *Journal of Nuclear Materials* 251 (1997) 34-48.
- [70] Y.N. Osetsky, D.J. Bacon, A. Serra, B.N. Singh, S.I. Golubov, One-dimensional atomic transport by clusters of self-interstitial atoms in iron and copper, *Philosophical Magazine* 83(1) (2003) 61-91.
- [71] N. Soneda, S. Ishino, A. Takahashi, K. Dohi, Modeling the microstructural evolution in bcc-Fe during irradiation using kinetic Monte Carlo computer simulation, *Journal of Nuclear Materials* 323(2-3) (2003) 169-180.
- [72] Marinica, Energy landscape of small clusters of self-interstitial dumbbells in iron, *Physical Review B* 83(094119) (2011).
- [73] F. Willaime, C.C. Fu, M.C. Marinica, J. Dalla Torre, Stability and mobility of self-interstitials and small interstitial clusters in  $\alpha$ -iron: ab initio and empirical potential calculations, *Nuclear Instruments and Methods in Physics Research Section B: Beam Interactions with Materials and Atoms* 228(1-4) (2005) 92-99.
- [74] R.C. Pasianot, V.P. Ramunni, Small interstitials clusters migration in bcc metals: A Molybdenum model, *Computational Materials Science* 48(4) (2010) 783-789.

- [75] R.E.Stoller, G.R.Odette, B.D. Wirth, Primary damage formation in bcc iron, *Journal of Nuclear Materials* 251 (1997) 49-60.
- [76] R.A. Johnson, Interstitials and Vacancies in  $\alpha$ -Iron, *Physical Review* 134(5A) (1964) A1329-A1336.
- [77] L.A. Zepeda-Ruiz, A. Stukowski, T. Opperstrup, V.V. Bulatov, Probing the limits of metal plasticity with molecular dynamics simulations, *Nature* 550(7677) (2017) 492-495.
- [78] D. Kandaskalov, C. Mijoule, D. Connétable, Study of multivacancies in alpha Fe, *Journal of Nuclear Materials* 441(1-3) (2013) 168-177.
- [79] C.-C. Fu, F. Willaime, Ab initio study of helium in  $\alpha$ -Fe: Dissolution, migration, and clustering with vacancies, *Physical Review B* 72(6) (2005).
- [80] C.A. Schuh, Nanoindentation studies of materials, *Materials Today* 9(5) (2006) 32-40.
- [81] N. Gunkelmann, E.M. Bringa, K. Kang, G.J. Ackland, C.J. Ruestes, H.M. Urbassek, Polycrystalline iron under compression: Plasticity and phase transitions, *Physical Review B* 86(14) (2012).
- [82] L. Malerba, M.C. Marinica, N. Anento, C. Björkas, H. Nguyen, C. Domain, F. Djurabekova, P. Olsson, K. Nordlund, A. Serra, D. Terentyev, F. Willaime, C.S. Becquart, Comparison of empirical interatomic potentials for iron applied to radiation damage studies, *Journal of Nuclear Materials* 406(1) (2010) 19-38.

- [83] Y. Gao, C.J. Ruestes, H.M. Urbassek, Nanoindentation and nanoscratching of iron: Atomistic simulation of dislocation generation and reactions, *Computational Materials Science* 90 (2014) 232-240.
- [84] Y. Gao, C.J. Ruestes, D.R. Tramontina, H.M. Urbassek, Comparative simulation study of the structure of the plastic zone produced by nanoindentation, *Journal of the Mechanics and Physics of Solids* 75 (2015) 58-75.
- [85] G. Ziegenhain, H.M. Urbassek, A. Hartmaier, Influence of crystal anisotropy on elastic deformation and onset of plasticity in nanoindentation: A simulational study, *Journal of Applied Physics* 107(6) (2010) 061807.
- [86] S. Goel, S.S. Joshi, G. Abdelal, A. Agrawal, Molecular dynamics simulation of nanoindentation of Fe<sub>3</sub>C and Fe<sub>4</sub>C, *Materials Science and Engineering: A* 597 (2014) 331-341.
- [87] H.J. D. Faken, Systematic analysis of local atomic structure combined with 3D computer graphics, *Comp. Mat. Sci.* 2 (1994) 279–286.
- [88] E.M. Bringa, V.A. Lubarda, M.A. Meyers, Response to “Shear Impossibility—Comments on ‘Void Growth by Dislocation Emission’ and ‘Void Growth in Metals’”, *Scripta Materialia* 63(1) (2010) 148-150.
- [89] E.M. Bringa, J.D. Monk, A. Caro, A. Misra, L. Zepeda-Ruiz, M. Duchaineau, F. Abraham, M. Nastasi, S.T. Picraux, Y.Q. Wang, D. Farkas, Are nanoporous materials radiation resistant?, *Nano Lett* 12(7) (2012) 3351-5.
- [90] Y. Tang, E.M. Bringa, M.A. Meyers, Ductile tensile failure in metals through initiation and growth of nanosized voids, *Acta Materialia* 60(12) (2012) 4856-4865.

- [91] Y. Tang, E.M. Bringa, B.A. Remington, M.A. Meyers, Growth and collapse of nanovoids in tantalum monocrystals, *Acta Materialia* 59(4) (2011) 1354-1372.
- [92] L.P. Dávila, P. Erhart, E.M. Bringa, M.A. Meyers, V.A. Lubarda, M.S. Schneider, R. Becker, M. Kumar, Atomistic modeling of shock-induced void collapse in copper, *Applied Physics Letters* 86(16) (2005) 161902.
- [93] J. Marian, J. Knap, G.H. Campbell, A Quasicontinuum study of nanovoid collapse under uniaxial loading in Ta, *Acta Materialia* 56(10) (2008) 2389-2399.
- [94] A.K. Tieu, H.T. Zhu, N.N. Huynh, G. Michal, Y. Gao, C. Lu, Atomistic simulation of nanoindentation of iron with different indenter shapes, *Proceedings of the Institution of Mechanical Engineers, Part J: Journal of Engineering Tribology* 223(7) (2009) 977-984.
- [95] R.S. David Christopher, Asta Richter, Atomistic modelling of nanoindentation in iron and silver, *Nanotechnology* 12 (2001) 372-383.
- [96] C.J. Ruestes, E.M. Bringa, A. Stukowski, J.F. Rodríguez Nieva, Y. Tang, M.A. Meyers, Plastic deformation of a porous bcc metal containing nanometer sized voids, *Computational Materials Science* 88 (2014) 92-102.
- [97] C.J. Ruestes, E.M. Bringa, A. Stukowski, J.F. Rodríguez Nieva, G. Bertolino, Y. Tang, M.A. Meyers, Atomistic simulation of the mechanical response of a nanoporous body-centered cubic metal, *Scripta Materialia* 68(10) (2013) 817-820.
- [98] D.J.B. Yu.N. Osetsky, A. Serra, Thermally activated glide of small dislocation loops in metals, *Philosophical magazine letters* 79(5) (1999) 273-282.